

NOVEL TRANSPORT LAYER
CHARACTERIZATION AND SYNTHESIS FOR
PROTON EXCHANGE MEMBRANE FUEL CELLS

by

DEVIN GARRET ZECH TODD

A THESIS SUBMITTED IN PARTIAL FULFILLMENT OF
THE REQUIREMENTS FOR THE DEGREE OF

DOCTOR OF PHILOSOPHY

in

THE FACULTY OF GRADUATE AND POSTDOCTORAL STUDIES

(Mechanical Engineering)

THE UNIVERSITY OF BRITISH COLUMBIA

(Vancouver)

December 2015

© Devin Garret Zech Todd, 2015

Abstract

Fuel cells are a promising energy conversion technology compatible with developing renewably sourced primary energy distribution. Proton exchange membrane (PEM) fuel cells are particularly suitable for automotive and portable applications. The present thesis advances novel PEM fuel cell porous transport layer (PTL) characterization and materials research. These layers link macro and nano scales by mediating energy and mass transport between reactant distribution channels and catalyst layers. Contemporary commercial PTLs are limited in selection. Moreover, typical characterization methods ignore essential material anisotropy. Herein, a novel transport layer synthesis concept is introduced. By adapting electrospinning technology, structures with engineered morphology are created. PTLs are produced with fibre diameters from 0.2 to 1.6 μm , and are characterized experimentally ex-situ and in-situ. Electrospun PTLs are shown to deliver 85% of equivalent commercial PTL current densities. Furthermore, the state-of-the-art for electronic resistance measurement of PTLs is improved, with rigorous attention given to the anisotropy of the fibre-based media. Novel method and apparatus provide this information as a function of mechanical strain. PTL in-plane resistivities are a unique contribution, where for commercial materials 4.5×10^{-4} to 1.5×10^{-4} $\Omega \cdot \text{m}$ are observed for strains from 0.0 to $-0.5 \text{ m} \cdot \text{m}^{-1}$. Finally, electrospun PTLs are developed to investigate the effect of within-plane anisotropy upon fuel cell performance. Electrospun layers are produced with progressively greater fibre alignment to effect anisotropy. This anisotropy is visualized via microscopy, and quantified using the aforementioned electronic resistivity methods. In-situ results with electrospun PTLs, of anisotropy ratios from 1 to 6, suggest greater performance with average fibre alignment perpendicular to gas distribution channels. The present thesis' contributions strengthen development of a PTL structure-property-performance relationship. With integration into a cell-level relationship, this can empower rational PEM fuel cell design.

Preface

The original idea of applying electrospinning techniques to improve water management in fuel cell transport layers was proposed by Dr. Mérida after learning about related work on catalyst deposition on carbon nanofibres. The work predates, and is separate from, Drs. Mérida and Ko's collaboration with Automotive Fuel Cell Cooperation in developing proton exchange membrane fuel cell catalyst layers via electrospinning.

Devin Todd is responsible for taking the general idea of electrospinning in fuel cell transport layers and identifying the specific topics of investigation documented herein. He is responsible for: the design research programme, execution of research tasks (with support of undergraduate research assistants under direct supervision), analysis of data, and dissemination of results in the form of conferences and publications.

Devin is responsible for most of the substantive and editorial preparation of this thesis:

- Chapters 1 and 2 are composed from final and draft versions of Devin's Ph.D. proposal defence document.
- A version of Chapter 4 has been published as a peer-reviewed full article in The Electrochemistry Society's *Journal of The Electrochemical Society* [1]. Devin was responsible for: scientific question formulation; apparatus and method design; data analysis and discussion; and article preparation. A colleague, Maximilian Schwager, offered critique in apparatus design and article preparation. Walter Mérida served as supervisor.
- A version of Chapter 5 is *under review* for publication as a peer-reviewed full article. Devin was responsible for: scientific question formulation; apparatus and method design; most data analysis and discussion; and most article preparation. Scott Bennett was responsible for: refining the apparatus to facilitate cyclic load application; data acquisition; and a portion of discussion and article formulation. Devin provided this opportunity to facilitate Scott Bennett's professional development. Walter Mérida served as supervisor.

- A version of Chapter 6 has been published as a peer-reviewed full article in *Journal of Power Sources* [2]. Devin was responsible for: scientific question formulation; apparatus and method design; data acquisition; data analysis and discussion; and article preparation. Walter Mérida served as supervisor.
- A version of Chapter 7 is *under review* for publication as a peer-reviewed full article. Devin was responsible for: scientific question formulation; apparatus and method design; data acquisition; data analysis and discussion; and article preparation. Walter Mérida served as supervisor.

A list of publications arising from this thesis is available in Appendix A.

Permission for reproduction of materials published in *Journal of Power Sources* is covered under Elsevier B.V.'s author's rights for personal (scholarly) purposes. Material published in *Journal of the Electrochemistry Society* was done so under their Open Access programme (CC BY-NC-ND).

Table of contents

Abstract	ii
Preface	iii
Table of contents	v
List of tables	vii
List of figures.....	viii
List of abbreviations.....	xi
List of symbols	xii
Acknowledgements	xv
Dedication.....	xvi
1 Introduction.....	1
1.1 Brief history and current status of the fuel cell.....	1
1.2 Motivation	1
1.3 Electrochemistry and fuel cells.....	2
1.4 Electrochemistry and reversible thermodynamics.....	2
1.5 PEM fuel cells	4
1.6 PEM fuel cells and irreversibilities.....	7
1.7 Nanofibres and electrospinning	10
1.8 Objectives	13
2 Background.....	16
2.1 PEM fuel cell transport layers in detail	16
2.2 Transport layer transport.....	17
2.3 Transport layer characterization techniques.....	20
2.4 Transport layer strategies.....	23
2.5 Electrospinning applications in PEM fuel cells	25
3 Experimental.....	26
3.1 Materials.....	26
3.2 Apparatus.....	26
4 Three-dimensional electronic resistance of PEM fuel cell transport layers	31
4.1 Introduction	31
4.2 Background.....	32
4.3 Method.....	38
4.4 Results and discussion	43
4.5 Summary	53
5 Electronic resistance of PEM fuel cell transport layers versus cyclic compression....	54
5.1 Introduction	54
5.2 Background.....	55
5.3 Method.....	57

5.4	Results and discussion	59
5.5	Summary	70
6	PEM fuel cell transport layers enabled via electrospun carbon nonwovens.....	71
6.1	Introduction	71
6.2	Method.....	73
6.3	Results and discussion	74
6.4	Summary	81
7	Implication of PEM fuel cell transport layer in-plane anisotropy	83
7.1	Introduction	83
7.2	Background.....	84
7.3	Method.....	87
7.4	Results and discussion	89
7.5	Summary	95
8	Conclusion	97
	References.....	101
	Appendix A	120
	A.1 Publications	120
	A.2 Publications in preparation	120
	A.3 Conferences.....	121
	Appendix B.....	123
	B.1 Introduction	123
	B.2 Literature.....	124

List of tables

Table 1: Selected electrospinning parameters and associated effects.....	13
Table 2: Materials used in the present thesis.	26
Table 3: Summary of experimental studies investigating PTL electronic resistance.	37
Table 4: PEM fuel cell transport layer materials evaluated in this chapter.	38
Table 5: Summary of relevant experimental studies into PTL transport resistance.	57
Table 6: Details of the electrospun transport layers produced in this study.....	87

List of figures

Figure 1: General half-cell reaction and encompassing control volume.	3
Figure 2: Cross-section of a contemporary PEM fuel cell.....	5
Figure 3: Schematic polarization curve demonstrating losses in a PEM fuel cell.	9
Figure 4: Schematic of electrospinning apparatus.	12
Figure 5: Schematic describing the thesis layout.....	14
Figure 6: SEM images of different PTL types: paper (a), felt (b) and cloth (c).....	16
Figure 7: SEM image of MPL.....	17
Figure 8: Photograph of NEU electrospinning apparatus.....	27
Figure 9: Photograph of NANON electrospinning apparatus.....	27
Figure 10: Photograph of research cell compression hardware. The graphite pieces are not the final BPPs.	28
Figure 11: Photograph of MEA and BPP in small cell hardware.....	29
Figure 12: Photograph of fuel cell test station.	30
Figure 13: Coordinate system and important directions used in this study.	33
Figure 14: Illustration of through-plane 4PP electrode arrangements in conventional (a) and micro-electrode (b) configurations.	34
Figure 15: Illustration of in-plane 4PP electrode arrangements in square (a) and linear (b) configurations.	35
Figure 16: Photograph of through-plane resistivity apparatus (a). Schematic of through-plane resistivity apparatus (b).	39
Figure 17: Photograph of in-plane resistivity apparatus (a). Schematic of in-plane resistivity apparatus (b).....	42
Figure 18: Compressive strain as a function of applied stress. Data are compiled from all through-plane measurements of a given material and fit to a power-law function; the error bars correspond to the 95% confidence bounds of the mean.	44
Figure 19: Principal resistivity through-plane as a function of PTL strain calculated via TP_METHOD_1.....	45
Figure 20: PTL-anvil contact resistance as a function of PTL strain calculated via TP_METHOD_1.....	46
Figure 21: Relative difference between two PTL-anvil contact resistances and one PTL-PTL contact resistance as a function of PTL strain.	47

Figure 22: Principal resistivity through-plane as a function of PTL strain calculated via TP_METHOD_2. Also plotted are the PTL-PTL and PTL-anvil contact resistances. 25/35 refers to the assumption that BA model material properties are consistent across manufactured thicknesses.....	48
Figure 23: Total area resistance in the through-plane direction as a function of PTL strain calculated via TP_METHOD_3. Values capture contributions of the bulk sample and of two PTL-anvil contacts; without separating the contact contributions, calculating a resistivity ($\Omega\cdot\text{m}$) is misleading.	49
Figure 24: Principal resistivities in-plane as a function of PTL strain. For a given material, the upper curve corresponds to FXD and the lower curve to FAD.....	51
Figure 25: Diagram representing in-plane resistivity as a function of direction. The principal components define the interval of possible values. If two orthogonal measurements are incorrectly assumed to coincide with principal directions, the interval width is under-estimated. However if the alignment of said orthogonal measurements to the principal direction is known, the true interval may be reconstructed.....	52
Figure 26: Compressive strain ϵ as function of applied stress.	60
Figure 27: Total area resistance in the through-plane direction as a function of strain.	62
Figure 28: Principal in-plane resistivities as functions of strain. The upper curve corresponds to FXD and the lower curve to FAD.	64
Figure 29: Principal in-plane resistivities, normalized by initial values, as functions of strains.	66
Figure 30: SEM images of PTLs before (a) and after three strain cycles (b) (using the in-plane apparatus).	67
Figure 31: Sheet resistances as functions of strain. Illustrated by the inset, the material is cycled in strain with progressively greater peak (in magnitude) strains each cycle.	68
Figure 32: Process diagram depicting where a sheet resistance measurement may integrate.....	69
Figure 33: Typical SEM micrographs of electrospun layers (a) pre-heat-treatment and (b) post-heat-treatment.	74
Figure 34: Plot of fibre diameter as a function of polymer concentration in the electrospinning dope.	75
Figure 35: Area resistance as a function of applied stress for experimental materials (post-heat-treatment) and commercial PTL.	76
Figure 36: Polarization curves of MEAs featuring cathode PTLs manufactured via electrospinning; also included are results of an MEA featuring a commercial cathode PTL.....	77
Figure 37: Mass-transport overpotentials of the different MEAs calculated from a voltage breakdown analysis.....	79

Figure 38: Images of sessile drop contact angle measurement (a) 10% PAN electrospun and (b) commercial PTL. The observed contact angles of the electrospun (10 wt% and 12.5 wt% PAN) and commercial PTLs were indistinguishable at $140 \pm 5^\circ$	79
Figure 39: Polarization data of 12.5 wt% PAN electrospun and commercial PTLs presented as 5, 25, 50, 75 and 95% quantiles of observed current at fixed potential. The inset plot comprises histograms and Weibull distributions of the currents densities at minimum potential. 10 wt% PAN and reverse polarization sweep data are not presented for sake of clarity.....	81
Figure 40: Illustration of transport layer anisotropy orientation versus flow-field channel geometry: aligned (a) and cross-aligned (b).	85
Figure 41: Illustration of transport layer interaction with adjacent functional layers: FAD aligned to major length (a), and FXD aligned (b).....	85
Figure 42: Schematic of electrospinning procedure (a) and SEM micrographs of electrospun transport layers of progressive anisotropy: 100 rpm (b), 500 rpm (c) and 1000 rpm (d).....	90
Figure 43: Ratio of resistivities (anisotropy ratio) in the FXD versus FAD directions. A higher value implies greater fibre alignment.	91
Figure 44: In-situ polarization results for baseline (commercial material) cells assembled with transport layer anisotropy either aligned or cross-aligned to flow-field geometry. Curves are fit following Equation 30, with superimposed distributions for different alignments at the potentiostatic measurement steps.....	92
Figure 45: In-situ polarization results for baseline (commercial material) cells assembled with transport layer anisotropy either aligned or cross-aligned to flow-field geometry. The contiguous curve is the fit of Equation 30 to all steady-state data, whereas the superimposed distributions reflect the underlying time-series data acquired at 1 Hz for different alignments.....	93
Figure 46: Normalized in-situ polarization results for cells featuring electrospun cathode transport layers of progressively greater in-plane anisotropy in different orientations versus flow-field geometry.....	94

List of abbreviations

PEM	proton exchange membrane, or polymer electrolyte membrane
MEA	membrane electrode assembly
CCM	catalyst-coated membrane
PTL	porous transport layer
GDL	gas diffusion layer
MPL	microporous layer
CL	catalyst layer
BPP	bipolar plate
MD	machine direction
CD	cross-machine direction
FAD	fibre-aligned direction
FXD	fibre-cross direction
ORR	oxygen reduction reaction
OCV	open-circuit voltage
SEM	scanning electron microscopy
4PP	four point probe
EIS	electrical impedance spectroscopy
HFR	high-frequency resistance
DMF	dimethylformamide
PAN	polyacrylonitrile
PTFE	polytetrafluoroethylene
Pt/C	carbon supported platinum
TP_METHOD_ (1,2,3)	through-plane electronic resistance method 1,2 or 3

List of symbols

Symbol	Unit	Description
F	$\text{C}\cdot\text{mol}^{-1}$	Faraday constant
i	$\text{A}\cdot\text{m}^{-2}$	current density
i_0	$\text{A}\cdot\text{m}^{-2}$	exchange current density
\vec{i}	$\text{A}\cdot\text{m}^{-2}$	current flux
\vec{E}	$\text{V}\cdot\text{m}^{-1}$	electric field
E_{cell}	V	cell potential
$E_{cathode}$	V	cathode potential
E_{anode}	V	anode potential
$E_{e,electrode}$	V	equilibrium electrode potential
$E_{e,cell}^0$	V	equilibrium cell potential at standard state
$E_{e,cell}^T$	V	equilibrium cell potential at temperature T and standard activities
η_{act}	V	activation overpotential
η_{MT}	V	mass-transport overpotential
η_{OCV}	V	OCV overpotential
T	K	temperature
ρ	$\Omega\cdot\text{m}$	resistivity
$\rho_{(x,y,z)(x,y,z)}$	$\Omega\cdot\text{m}$	resistivity in direction according to subscript
ρ_{θ}	$\Omega\cdot\text{m}$	resistivity in direction θ
ρ_{air}	$\Omega\cdot\text{m}$	resistivity of air phase
ρ_{carbon}	$\Omega\cdot\text{m}$	resistivity of carbon phase
R_s	$\Omega\cdot\text{sq}^{-1}$	sheet resistance
R_{cell}	$\Omega\cdot\text{m}^2$	cell resistance
$R_{BPP-PTL}$	Ω	contact resistance between BPP and PTL
R_{PTL}	Ω	resistance of PTL
R_{PTL-CL}	Ω	contact resistance between PTL and CL
R_{CL}	Ω	resistance of CL
R_{CL-mem}	Ω	contact resistance between CL and membrane
R_{mem}	Ω	resistance of membrane
$R_{PTL-anvil}$	Ω	contact resistance between PTL and anvil
$R_{PTL-PTL}$	Ω	contact resistance between PTL and PTL
$R_{z,single}$	Ω	observed resistance in z direction, for singular PTL
$R_{z,double}$	Ω	observed resistance in z direction, for stack of two PTLs

R_z	Ω	observed resistance in z direction
R_x	Ω	observed resistance in x direction
R_y	Ω	observed resistance in y direction
t	m	observed (stack) thickness
$t_{average}$	m	PTL average thickness
t_0	m	thickness at zero strain
A	m^2	area of sample
$L_{(x\ or\ y)*}$	m	equivalent isotropic sample length
ϕ	$m^3 \cdot m^{-3}$	porosity
ϕ_0	$m^3 \cdot m^{-3}$	porosity at zero strain
S_{water}	$m^3 \cdot m^{-3}$	volume fraction of water saturation
ϵ	$m \cdot m^{-1}$	strain
τ	$m \cdot m^{-1}$	tortuosity
D	$m^2 \cdot s$	diffusivity
D_{eff}	$m^2 \cdot s$	effective diffusivity
β	degrees	angle between FAD and MD
θ	degrees	angle between x and MD
α	degrees	$\theta - \beta$
$m_{carbon} V^{-1}$	$kg \cdot m^{-3}$	bulk density of carbon in a PTL
W_{areal}	$kg \cdot m^{-2}$	areal weight of a porous transport layer
W_{PTFE}	$kg \cdot kg^{-1}$	mass fraction of PTFE in a porous transport layer
\tilde{g}_j	$J \cdot mol^{-1}$	Gibbs free energy of compound j
R	$J \cdot K^{-1} \cdot mol^{-1}$	universal gas constant
$\Delta \tilde{S}_{rxn}^0$	$J \cdot K^{-1} \cdot mol^{-1}$	reaction entropy change at standard conditions
e^-	n/a	electron
n	n/a	number of electrons
n_{rds}	n/a	number of electrons in rate determining step of Butler–Erdey-Grúz–Volmer equation
n_{PTL}	n/a	number of samples in PTL stack
n_{cycle}	n/a	cycle number of cyclic strain application
$\Delta_{Single\&Double}$	n/a	average percent difference between $R_{z,single}$ and $R_{z,double}$
M_j	n/a	compound j
v_j	n/a	stoichiometric number of compound j
a_j	n/a	activity of compound j
α_a	n/a	anodic charge transfer coefficient
α_c	n/a	cathodic charge transfer coefficient

<i>a&b</i>	n/a	Tafel parameters
<i>E₀, b, R, m, n</i>	n/a	fit parameters for polarization curve
<i>x, y, z</i>	n/a	frame of reference directions
<i>superscript ' </i>	n/a	principal direction alignment

Acknowledgements

I would like to thank everyone for tolerating me. I would not have made it this far (or at least in as timely a manner) without some help!

I first express my gratitude to my supervisor Dr. Walter Mérida and supervisory committee: Drs. Steven Rogak and Frank Ko, for their patronage throughout the years. Having been at UBC for so long, I wish to extend this gratitude to the faculty who have provided mentorship since my undergraduate programme. I must also thank the support staff who let me break their tools!

I acknowledge the agencies that funded my research: the Natural Sciences and Engineering Research Council of Canada (NSERC), the Catalysis Research for Polymer Electrolyte Fuel Cells Network (CaRPE-FC), and the University of British Columbia (UBC). I would also like to acknowledge the equipment access offered by UBC's Advanced Fibrous Materials Laboratory; and the help of its personnel: Sophia Chan, Ryan Huizing and Heejae Yang.

Thanks to past and present members of Dr. Mérida's research group for their aid and friendship. Thank you Maximilian Schwager for your counsel, for doing the most to keep the lab running, and for sharing a drink when it is and is not. Thank you Shankar R. Dhanushkodi for asking difficult questions and letting me ask some in return. Further thanks are deserved by Mauricio Escalante Soberanis and Sarah Flick for sharing the start of the adventure.

Special appreciation is reserved for my parents, grandparents, and siblings: Caylin and Katrina. My thesis is done, please stop asking about it!

Finally, I express my love for Monica – who leads me to sail the ocean and climb mountains.

To mom,
dad,
and my sisters.

1 Introduction

1.1 Brief history and current status of the fuel cell

Fuel cells are electrochemical devices which extract useful work from redox chemical reactions by mediating otherwise uncontrolled electron exchange. Originally pioneered by Schönbeim (1799-1868) and Grove (1811-1896) in the nineteenth century, it was Bacon (1904-1992) in the mid-twentieth century who resolved many of the hurdles baring practical (alkaline cell) application. New-archetype proton exchange membrane (PEM) fuel cells in particular were pursued in the 1950's by Grubb at General Electric [3]; and 1966, the industry standard membrane material Nafion was introduced by DuPont. It was not until the later technological push of Ballard Power Systems in the 1980-1990's that PEM fuel cells would become a dominant division of the industry.

Today's fuel cell industry sees PEM systems dominate automotive applications. However widespread deployment of consumer fuel cell vehicles is seemingly deadlocked by unwillingness of automobile manufacturers to act in an environment devoid of fuelling infrastructure – and policy makers unwilling to support infrastructure for a non-existent automobile fleet.

1.2 Motivation

Energy – its acquisition, storage, transportation, distribution, and end-use application has been at the heart of human endeavour since civilization. Disappointingly, our current energy paradigm centred on the exploitation of non-renewable and depleting hydrocarbon resources is wholly unsustainable.

Renewable energy solutions including: wind, tidal, geothermal, solar; offer a progressive avenue for human development. However, such systems face difficulty in widespread deployment for reasons of storage and transport. Hydrogen is a promising candidate for bridging the divide

between energy extraction and end-user application [4,5]. Here, fuel cells are the devices which permit efficient transformation of stored chemical energy into useful electrical work.

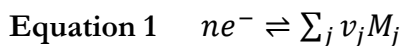
The present thesis advances the state-of-the-art of PEM fuel cell characterization techniques and materials synthesis; facilitating understanding of fuel cell function and supporting integration into the future energy complex. Electrospinning technology is applied towards component synthesis in this thesis, demonstrating: technological feasibility, refinement opportunities, and diagnostics applications. Required to validate said components, and prompted by realization that existing state-of-the-art methods are inadequate, complementary work progresses on ex-situ characterization techniques. The following sub-sections provide further introduction; whilst thesis objectives are detailed at the end of this chapter.

1.3 Electrochemistry and fuel cells

Electrochemistry is the study of chemical reactions occurring at the interface between an electronic conductor (electrode) and ionic conductor (electrolyte) where electron transfer occurs between said media. A fuel cell can be generalized as a device which implements an electrochemical reaction(s) to generate work (electricity); where reactants and products are introduced and extracted from reaction site(s) during operation. In contrast, a battery is composed of its reactants and products e.g. in the electrodes or electrolyte. This definition of a fuel cell permits innumerable chemistries. Concerning H₂-O₂(air), systems may be broadly categorized by the electrolyte configuration; which directly impacts the choice of operating conditions as well establishes much of the cell and balance-of-plant design requirements. The present thesis contends with H₂-O₂ PEM fuel cells and further discussion will occur in this context; though many of the background, ideas, and research and results are extensible to other electrochemical systems (e.g. alcohol fuel cells, PEM electrolyzers, supercapacitors, etc.).

1.4 Electrochemistry and reversible thermodynamics

Electrochemistry is fundamentally governed by Faraday's laws of electrolysis and the laws of thermodynamics. The former establishes proportionality between the quantity of a substance altered and the quantity of charge transferred at an electrode; the latter establishes the energy exchanges of the process. A control volume analysis may be applied to one electrode (half-cell) of an electrochemical device with a general half-cell reaction:



, this is illustrated in Figure 1.

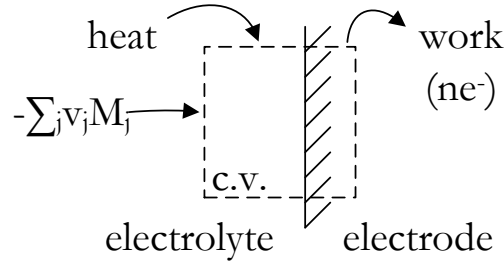


Figure 1: General half-cell reaction and encompassing control volume.

In the absence of irreversibilities, and assuming isothermal and isobaric conditions, energy and entropy balances for this system may be solved for the maximum work available. Treating electrons as solely work carriers; on a per coulomb of charge transferred basis this is:

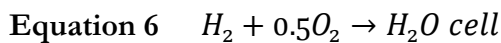
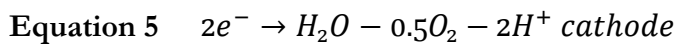
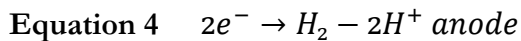
Equation 2
$$E_{e,electrode} = -\frac{\sum_j v_j \tilde{g}_j}{nF}$$

Net reaction progression can only occur if work interaction exists across the system boundary. An electrode in isolation or a cell configured in open-circuit will have no net current fluxes, and is said to be in electrochemical equilibrium. Realizing an electrochemical cell requires a pair of electrodes, each supporting a half-cell reaction. The reduction process at the cathode consumes the electrons released from the oxidation process at the anode; whilst ions are exchanged with the electrolyte and the electrons are shunted through a load or power source external circuit. The equilibrium potential for a cell is:

Equation 3
$$E_{cell} = E_{cathode} - E_{anode}$$

The cell potential is the difference between cathode and anode potentials; that which is accessible to measure across device terminals. The anode reaction progresses in the oxidation direction, so its electrode potential contribution to cell potential (defined in the reduction direction) is subtracted. Whether a system is galvanic (work producing, positive cell potential) or electrolytic (work consuming, negative cell potential) is based on the user's intent. It is important to define which half-cell reaction is anodic and which is cathodic.

The half-cell and cell reactions for the H₂-O₂ fuel cell are:



Applying Equation 3, equilibrium cell potential at standard-state ($T=298$ K and $a_j=1$), $E_{e,cell}^0$, for a H₂-O₂ fuel cell is 1.23 V. To correct a standard-state equilibrium cell potential for non-standard conditions, one approach is to first correct for temperature using the Maxwell relation:

$$\text{Equation 7} \quad \left(\frac{\partial E_{e,cell}^0(T)}{\partial T} \right)_p = \frac{\Delta \tilde{s}_{rxn}^0(T)}{nF}$$

The equilibrium cell potential at temperature T , $E_{e,cell}^T$, is then corrected for species activities via the Nernst equation:

$$\text{Equation 8} \quad E_{e,cell} = E_{e,cell}^T - \frac{RT}{nF} \ln \left(\prod_j a_j^{v_j} \right)$$

Alternatively, if the Gibbs free energies of the species are already known at the conditions of interest, Equation 2 and Equation 3 may be applied directly. Under some circumstances it is more efficient to determine Gibbs free energies directly from state-equations; rather than make approximations or compensate for real effects in ideal relationships. An example of the direct approach is detailed by Todd et al. in [6], where H₂-O₂ reversible cell potentials were determined for temperatures and pressures up to 1000 K and 100 MPa respectively.

Equilibrium potential reflects the maximum work extractable from (or minimum work required into) an electrochemical device. In real devices, irreversibilities create more complex scenarios; this is discussed in section 1.6 for the PEM fuel cell.

1.5 PEM fuel cells

PEM fuel cells are characterized by application of a gas impermeable, electronically resistive, ionically (proton) conductive, polymer-based membrane to effect isolation of oxidation and reduction reactions at their respective electrodes; whilst facilitating ion exchange between reactions and electron redirection through an external circuit. The present thesis specifically contends with perfluorosulfonic acid based membranes. A cross-section schematic of a contemporary PEM fuel cell is offered in Figure 2.

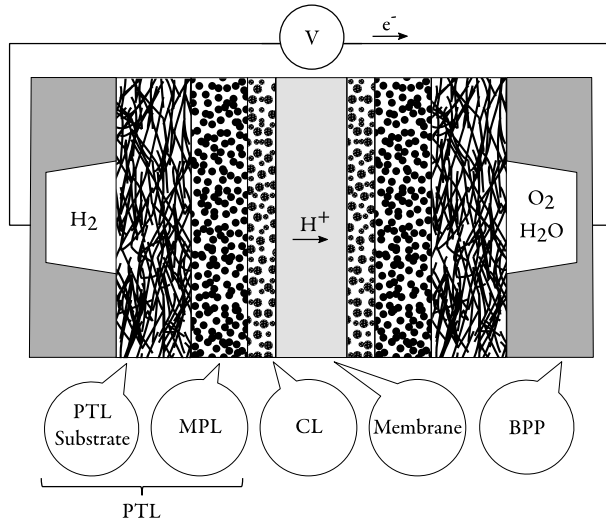


Figure 2: Cross-section of a contemporary PEM fuel cell.

The cell consists of several unique components:

1. Porous transport layers (PTLs)
 - 1.1. PTL substrate
 - 1.2. (optional) microporous layers (MPLs)
2. Catalyst layers (CLs), a.k.a. electrodes (though this may also include PTLs)
3. Proton exchange membrane (or just “membrane”)
4. Bipolar plates (BPPs)

1 through 3 together form the membrane electrode assembly (MEA). 2 and 3 together form the catalyst-coated membrane (CCM). Finally, 1.1 in the absence of 1.2 may also be referred to as PTL. While other terms exist in the PEM community for describing these and similar components e.g. gas diffusion layers, gas diffusion electrode; the present thesis will maintain the aforementioned nomenclature.

The idealized fuel cell operates as follows:

1. H_2 and O_2 reactant gases are fed to the anode and cathode respectively via flow-field channels formed in the BPP.
2. H_2 reacts at the anode, each molecule splitting into a pair of protons ($2H^+$) and releasing two electrons (e^-).
3. Protons travel through the membrane, while electrons are shunted through the BPP to an external circuit.
4. Protons and electrons rejoin at the cathode, reacting with O_2 to produce H_2O .

Note that a functional PEM fuel cell module requires more than the aforementioned components; the-balance-of plant includes: gas conditioning and delivery, power electronics, instrumentation and controls. Further, multiple unit cells are configured in series to form a stack with greater power and more serviceable voltage.

1.5.1 Bipolar plates

The purpose of the BPPs is to provide inter-cell electronic connectivity and to manage the distribution and recovery of reactants and products over a cell's active area. Graphite is the conventional material as it possesses good electronic conductivity while being tolerant of the chemical and electrochemical environment present in the fuel cell. Polymer options are under research, while metallic options are growing in popularity for cost reasons [7,8].

1.5.2 Porous transport layers

The purpose of the PTLs is to facilitate charge and mass transport from the CLs to the BPPs and flow-fields. Sheets of carbon fibre papers, felts or textiles, impregnated with polytetrafluoroethylene (PTFE), are the conventional materials. The MPL is an optional addition to the PTL, interposed between primary PTL substrate and CL. It is a water management device comprising sub-1 μm pores and treated with hydrophobic agents.

1.5.3 Catalyst layers

The CLs are the sites of chemical energy to work transformation within a fuel cell. At the minimum, a CL requires: catalysed reaction sites, ionic connectivity to the electrolyte, electronic connectivity outwards, and physical access for reactive species.

1.5.4 Proton exchange membrane

The purpose of the membrane is to isolate the half-cell reactions. The membrane permits conduction of ions, while being impermeable (ideally) to gaseous species and electronic charge. The prevalent materials are perfluorinated ionomers, of which Nafion is an example. Membranes may also incorporate structures for mechanical reinforcement and greater gas impermeability; details of which are trade-secrets amongst manufacturers.

A critical property of the ionomer's behaviour is its water saturation dependent ionic conductivity. Fully hydrated ionomer achieves maximum conductivity whereas the inverse is true for the dry case. The water available for ionomer conductivity in the membrane and CLs must be balanced against flooding of the MEA which restricts performance; this constitutes the topic of water management in PEM literature, and is addressed further in section 2.2.

1.6 PEM fuel cells and irreversibilities

Thermodynamic irreversibilities are incurred in real electrochemical devices. The irreversibilities are functions of net current density (i), and may also exist at open-circuit. In the PEM fuel cell they are categorized into: open-circuit voltage (OCV) losses, activation losses, ohmic losses, and mass-transport losses. They may be expressed as terms which subtract from cell potential:

$$\text{Equation 9} \quad E_{cell} = \left(E_{e,electrode} + \eta_{act}(i) + \eta_{MT}(i) \right)_{cathode} - \left(E_{e,electrode} + \eta_{act}(i) + \eta_{MT}(i) \right)_{anode} - \eta_{OCV} - |i|R_{cell}$$

By convention, a negative overpotential drives a reaction in the reduction direction and a positive overpotential drives a reaction in the oxidation direction. Overpotentials are the deviations of actual electrode potential from equilibrium electrode potential; and are functions of the electrode-electrolyte interface. Ohmic losses are omnipresent and always penalize. The following subsections shall address each contribution in turn; for further detail, the reader is directed to [9].

1.6.1 Open-circuit voltage overpotential

The OCV overpotential in a PEM fuel cell is the difference between the equilibrium cell potential and the real potential measured across open cell terminals. Mixed potentials created by H₂ cross-over is the accepted theory for its existence. Briefly, the membrane is not fully impermeable to H₂ gas; a finite amount can diffuse (cross-over) the membrane and react along with O₂ on the cathode CL. The effect of H₂ cross-over is most pronounced at zero current density. As current densities increase, the activity of H₂ at the anode CL available to drive diffusion decreases.

1.6.2 Activation overpotential

Activation overpotentials are attributable to irreversibilities in the electrode reaction kinetics. Electrode reactions may be composed of multiple chemical and electron transfer reaction steps. Each reaction step has an associated rate law and rate constant; generally one is assumed to be the rate determining step whilst the others are in quasi-equilibrium. Activation overpotentials are often modelled by the Butler–Erdey–Grúz–Volmer equation, which for an electrode where both oxidation and reduction may occur is given by:

$$\text{Equation 10} \quad i = i_0 \left(e^{\frac{\alpha_a n_{rds} F \eta_{act}}{RT}} - e^{-\frac{\alpha_c n_{rds} F \eta_{act}}{RT}} \right)$$

, where the exchange current density (i_0) is the key parameter reflecting CL activity. At larger overpotentials where one exponential term dominates, Equation 10 simplifies to the Tafel equation:

Equation 11 $\eta_{act} = a \pm b \log(i)$

, where a and b are the Tafel constants for a given condition. In practice with H₂-O₂ PEM fuel cells, the sluggishness of the ORR is assumed to dominate the activation overpotential of the cell, and the contribution from the hydrogen oxidation reaction is neglected. Refinement to electrode specific activation (or other) overpotentials requires a cell configured with a reference electrode, unavailable and/or unfeasible in most cell designs.

1.6.3 Ohmic irreversibilities

The ohmic irreversibilities are the losses incurred by current travelling through the finite conductivity cell media. For a PEM fuel cell, it may be written via Ohm's law:

Equation 12 $|i|R_{cell} = |i|[(R_{BPP-PTL} + R_{PTL} + R_{PTL-CL} + R_{CL} + R_{CL-mem})_{cathode} + (R_{BPP-PTL} + R_{PTL} + R_{PTL-CL} + R_{CL} + R_{CL-mem})_{anode} + R_{mem}]$

It comprises contributions from electronic conducting media, ionic conducting media, and the contact resistances at their interfaces. Complications posed by in-plane current transport are neglected for simplicity. Cell resistance is often ascribed to the membrane, as ionomer is less conductive than the other materials. However this is a gross simplification; ionomer exists also within the CL, and other components and their contact resistances are significant. In normal practice, cell resistance is determined experimentally rather than modelled. The topic of cell resistance, in the context of PTL contributions, is discussed in Chapters 4 and 5 .

1.6.4 Mass-transport overpotential

The mass-transport overpotential represents the penalties incurred in providing reactants to (or removing products from) reaction sites at an electrode surface. At equilibrium, bulk species concentrations and (electrode) surface concentrations are equal. In operation, reactants are consumed and their surface concentrations tend to zero with increasing current. At any time, the relationships (e.g. the Nernst equation) defining equilibrium potentials may hold at the electrode surface, therefore decreasing reactant concentrations (activities) suppress the potential. The limiting current density, which is the maximum current attainable, occurs when surface concentrations of reactants tend to zero.

In PEM fuel cells, species must travel through the tortuous and possibly liquid water saturated porous structures of the MEA. Tortuosity decreases the driving activity gradient while O_2 diffusion through liquid water is severely inhibited.

1.6.5 Irreversibilities consolidated

The interaction of irreversibilities with equilibrium cell potential in a PEM fuel cell is effectively communicated in a polarization curve. Figure 3 offers a schematic example.

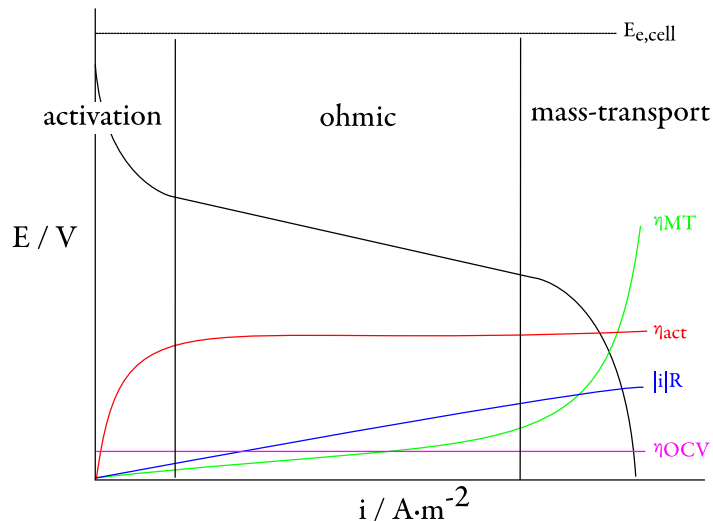


Figure 3: Schematic polarization curve demonstrating losses in a PEM fuel cell.

Neither mass-transport nor activation overpotentials are resolved for individual electrodes; determining the individual contributions of anode and cathode requires a reference electrode which is difficult to incorporate into a PEM fuel cell. It is normally assumed the cathode ORR reaction dominates behaviour. Further, each type of loss mechanism tends to dominate different levels of current density; thus activation, ohmic and mass-transport regions may be identified.

The loss of power into irreversibilities goes towards heat production; which may then require active cooling solutions. Balance-of-plant (pumps, compressors, heat exchangers, control circuits) diminishes fuel cell module efficiency, but is outside the present thesis's scope of study. Also out-of-scope is consideration of unwanted side-reactions in a cell.

1.7 Nanofibres and electrospinning

Fibre structures are a ubiquitous component in nature and industry. Fibres are typified by a slender, flexible, one-dimensional shape. They may be arranged randomly or ordered, and may exist in isolation or as part of a composite material. As diameter scales contract, nanofibres can present particular properties. Firstly, mechanical effects include: molecular alignment along fibres, fewer defects, and availability of functional textured surfaces. Secondly are incredible specific areas (e.g.: $10^3 \text{ m}^2\cdot\text{g}^{-1}$), which for interfacial chemical and physical processes economizes material and volume. Finally is the possibility to enable nanoscale phenomena to affect macro-scale material functionality. As length scales decrease, existing phenomena change in relative importance and new phenomena may develop. Examples include: capillary forces, intermolecular forces, catalysis, super-paramagnetism, tunnelling current, quantized electrical conductance, and size-dependent electromagnetic response.

Contemporary PEM fuel cell transport layers are carbon fibre based. Most common are paper types; these are manufactured similarly to wood fibre paper, but with pre-prepared carbon fibres. The resulting porous structure permits energy and mass transport through its' solid and void phases respectively. Further manufacturing and function information is detailed in section 2.1. Although research continues on non-fibre based transport layer designs (e.g. sintered powders or micro-machined sheet materials, see section 2.4); these often display poor performance, and may not as readily benefit from the theoretical and experimental advances tailored to their fibre-based equivalents. These reasons motivate the present thesis' approach of: maintaining the accepted fibre-based standard, but challenging the means of synthesis to enable heretofore unavailable morphological control.

Fibre generation pathways with possible transport layer applicability include: melt, wet, and dry spinning. Further pathways, geared towards smaller fibre geometries, include: nanofibre drawing, meltblowing, template extrusion, self-assembly, phase separation, vapour deposition, and electrospinning. These methods differ in characteristics of: polymer compatibility; fibre dimensions (e.g.: size, shape and length); product form (e.g.: deposited sheet or wound filament); ease of production scale-up; and laboratory convenience. Electrospinning is used for the present thesis; this selection is guided by the technology's capacity to deliver single step generation of free-standing cohesive layers, with additional promise of fibre and layer level morphological control.

Electrospinning is a technique for the preparation of fibres via acceleration of a precursor solution (dope) through an electrical field. Its origins exist in the eighteenth century work of Bose (1710-1761) who studied the high-voltage atomization of liquid; it was not until the early

twentieth century that patents for devices which spray liquids [10,11] and later electrospin polymers [12] via electrical potentials appeared. The technology remained relatively dormant until the 1990s, when interest swelled with the promulgation of nanotechnology [13].

Reviews addressing electrospinning technology are abundant [13–29]. The technique has been applied in: filtration, textiles, sensorics, electronics, energy devices and bio-medicine. In the present thesis only the most salient information is discussed. The greatest advantages of electrospinning technology are its versatility and ease of execution.

Fibres may be produced over a wide range of diameters, from a few dozen nanometres to tens of micrometres. They may be electrospun from nearly any polymer solution or melt, with innumerable possible additives. Such additives include: metal or ceramic precursors, carbon nanotubes, functional nanoparticles, and biological agents. Fibres may be produced from a single spinneret or a multi-nozzle arrangement, each with possibly different dopes. Furthermore, the morphology of fibres is variable. It is possible to produce core-shell, hollow, or porous fibres; and fibres of constant diameter, ribbons, or bead-on-string shape. Finally, fibres may be spun into nonwoven mats (standard), sheets of aligned fibres, pseudo-woven sheets and continuous yarns. Post-treatment of electrospun products enables further options: thermal treatments for carbon fibre and/or inorganic material synthesis; reduction of precursors to synthesize pure metals in-situ; and fibre surface functionalization and/or decoration.

Relating to manufacturability, for PEM fuel cells to displace combustion engines in automotive applications, inordinate volumes are required. Debe suggests 4.50 billion MEAs (with active areas of approximately 300 cm² each) per year to satisfy an annual vehicle production rate of 15 million (10% of the 2030 world market) [30]. This environment is challenging for development, as new functional layer constructs require inherent manufacturing scalability. Electrospinning offers simplified single-step generation of fibre structures, unlike present methods, and efforts in developing mass-production electrospinning methods are encouraging [31]. Leveraging multi-jet spinning and reel-to-reel manufacturing, sufficient throughput is foreseeable.

The elementary components of an electrospinning apparatus comprise: a pumping device with capillary tip, a grounded target, and a high-voltage power supply biasing the two. These are presented in Figure 4.

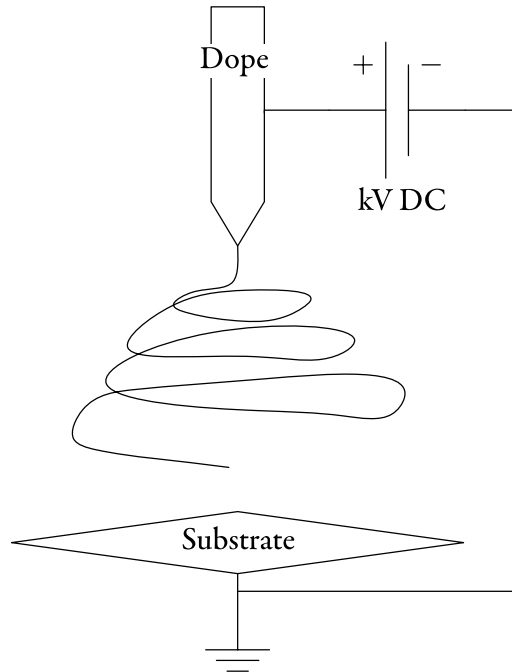


Figure 4: Schematic of electrospinning apparatus.

The mechanism of electrospinning follows:

1. Dope from the capillary tip is drawn towards the target, forming a conical meniscus known as a Taylor cone [32].
2. A critical point occurs (when electric field strength exceeds surface tension), where a jet erupts from the cone. As the jet accelerates towards the target, it is drawn out whilst solvent evaporates.
3. Radial instabilities create chaotic oscillations of the jet, nominally building a randomly aligned nonwoven fibre mat upon the target.

The morphological properties of the product are dependent upon a large number of parameters. Such parameters may relate to the polymer itself, to the spinning dope, and to the electrospinning process. Excursions from ideal parameters may produce undesirable results such as electrospraying or melting of fibres into a sheet upon the target. Consequently, while the procedure may be simple, modelling is challenging. General trends are presented in [13,27] and summarized in Table 1.

Table 1: Selected electrospinning parameters and associated effects.

Parameter	Effect
Polymer concentration increases	Fibre diameters increase, uniform cylindricity increases
Polymer concentration decreases	Fibres diameters decrease, propensity for bead formations increase, eventual lack of electrospinning
Solution conductivity increases	Bead formation is suppressed
Solvent volatility increases	Textured fibre surfaces promoted, may lead to filming
Voltage increases	Fibre diameters decrease, then increase
Distance increase	Fibre diameters decrease
Flow rate increases	Fibre diameters increase, may promote bead formation

1.8 Objectives

Electrospun transport layers are sought to improve comprehensive H₂-O₂ PEM fuel cell performance (inclusive of: output power, durability, and cost); not necessarily by intrinsic material properties, but by leveraging electrospinning's faculties for rational design and manufacturing versatility. For automotive applications, targets are published by the United States Department of Energy's U.S. DRIVE programme [33]. It is interesting to note while explicit performance metrics and targets for CLs are provided, PTLs are obfuscated within MEA targets. This may reflect an indifference or perhaps capitulation to the limited patterns of PTLs available.

Contemporary commercial PTLs are available in limited morphological permutations. The high-volume paper-making manufacturing methods are not conducive to manipulating deposition nor composite designs. In contrast, electrospun fibre layers with structured: fibre diameters, pore-sizes, thicknesses and anisotropy; might be tailored for specific cell designs and/or operating point(s). This optimization of transport layers comprises an advanced expression of electrospinning's potential. However, contemporary understanding of PEM fuel cell operation is insufficient to define what collection of properties constitutes an improved layer. Much of the challenge originates from the coupled multi-phase, multi-physics, and multi-scale interactions. Moreover, the limited selection of contemporary transport layers reduces the attractiveness of studying hypothetical structure optimization. The present thesis offers a means to realize such structures; and applies them to probe the importance of select properties.

A research programme of incremental material synthesis parameter permutation was incompatible with available laboratory resources. Instead, the present thesis addresses the divide between materials development and application. This approach capitalizes on existing

PEM fuel cell expertise and tools developed within the research group. Figure 5 is a schematic layout of the thesis.

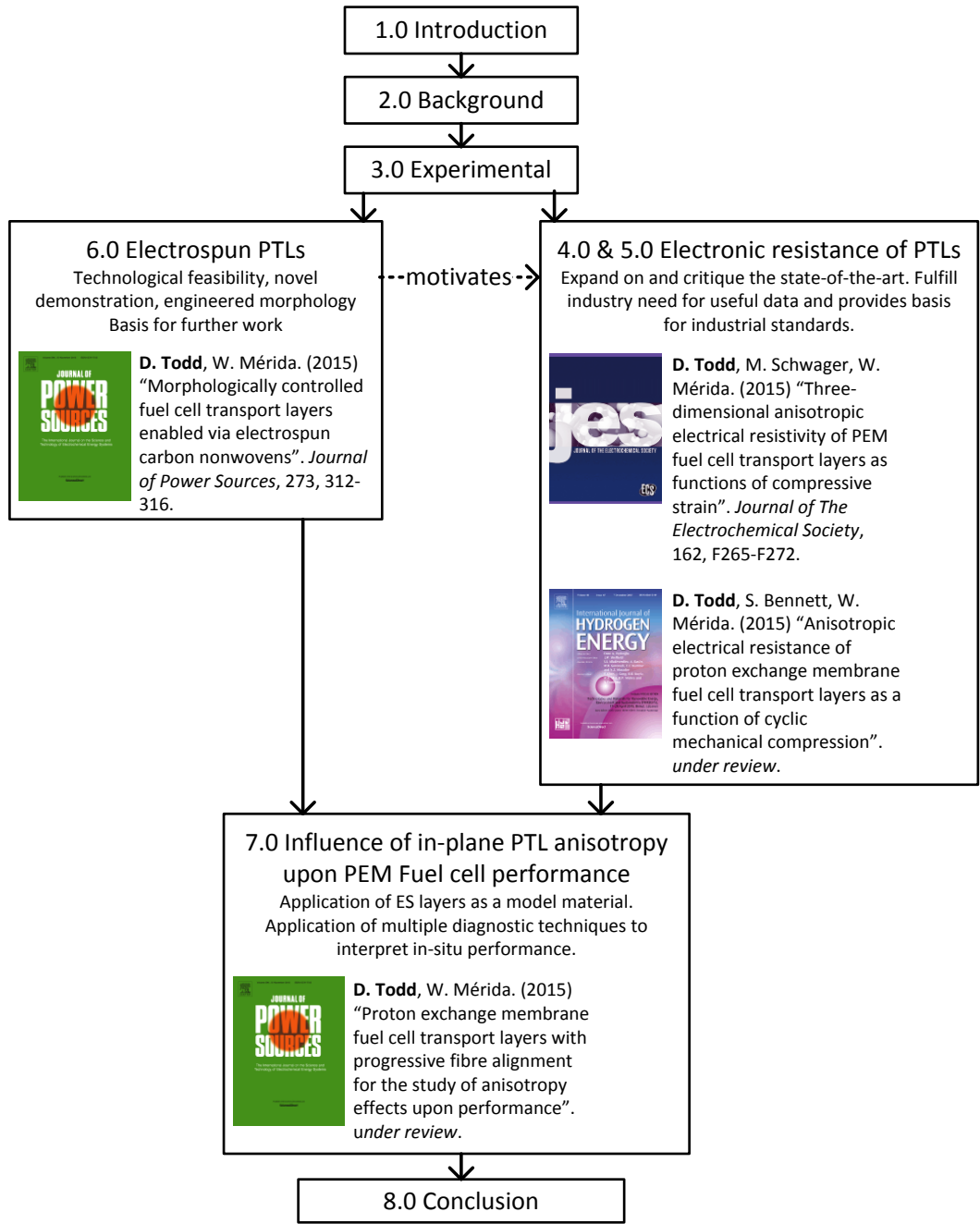


Figure 5: Schematic describing the thesis layout.

The research objectives and strategies comprise:

- Demonstrate the effectiveness of electrospun transport layers for fuel cell application. Proof-of-concept transport layers are synthesized and tested within a fuel cell
- Control the structure of transport layers. Transport layers are created with novel control over fibre diameters and alignment.
- Improve the state-of-the-art for electronic resistance characterization of PEM fuel cell transport layers. Existing approaches are critiqued and a novel method for acquisition of in-plane resistivities as a function of strain is presented.
- Establish the importance of transport layer within-plane anisotropy. A test framework is introduced which uses novel PTLs produced with progressive and quantified anisotropy.

Following the first and second objectives, a procedure is developed for the novel manufacture of electrospun transport layers. The capacity to engineer fibre layer morphology is demonstrated by controlling fibre diameter. This parameter's interplay with porosity, tortuosity, and consequently transport coefficients, make it an attractive opening for investigation. These layers are characterized both ex-situ and in-situ in a research cell. Results are compared to those obtained with a commercial product. These efforts constitute Chapter 6 of this thesis.

A concern for the synthesized layers was obtaining adequate electronic conductivity; necessitating development of apparatus to quantify the property. A literature review of PEM fuel cell transport layer electronic transport characterization revealed significant gaps in the state-of-the-art. Specifically, through-plane direction resistance analysis is rife with incompatible methods; whilst in-plane direction analysis lacks rigorous methods altogether. Novel apparatus are developed to characterize PTL resistance, and assumptions underpinning analysis methods in the literature are methodically critiqued. These efforts constitute Chapters 4 and 5 of this thesis. Of specific interest is treatment of the anisotropic nature exhibited by the fibre-based layers; this may have direct impact upon fuel cell performance and its investigation is complemented by electrospun transport layer development.

The culminating Chapter 7 details investigation into the influence of transport layer anisotropy upon PEM fuel cell performance. The implications of both: anisotropic structure orientation and magnitude of anisotropy are probed. This work is a unique contribution to the literature. Preceding electrospun transport layer and fuel cell characterization developments are harmonized. Electrospinning is adapted to synthesize model materials; whilst the characterization tools inform analysis

2 Background

2.1 PEM fuel cell transport layers in detail

Proton exchange membrane fuel cell PTLs are macro-porous carbon layers with typical thicknesses in the vicinity of 200 μm . They bridge the macro-scale to the nanoscale and must:

- Provide electronic continuity between CLs and BPPs. Both in-plane and through-plane performance is important because BPPs are not in continuous contact with the PTL area.
- Provide thermal conductivity to dissipate heat produced within a cell outwards.
- Permit transport of gaseous species between BPP flow-channels and CLs.
- Mediate transport and retention of liquid water within a cell.
- Tolerate the chemical and electrochemical environment without degradation.

Unsurprisingly, some of these functions are at odds with each other. The best thermal and electronic conduction would be achieved with a solid substrate, while the best mass-transport would be achieved with an infinitely porous material. Conventional PTLs attempt to reconcile the disparity by using permeable paper, felt or woven morphologies; these are illustrated in Figure 6.

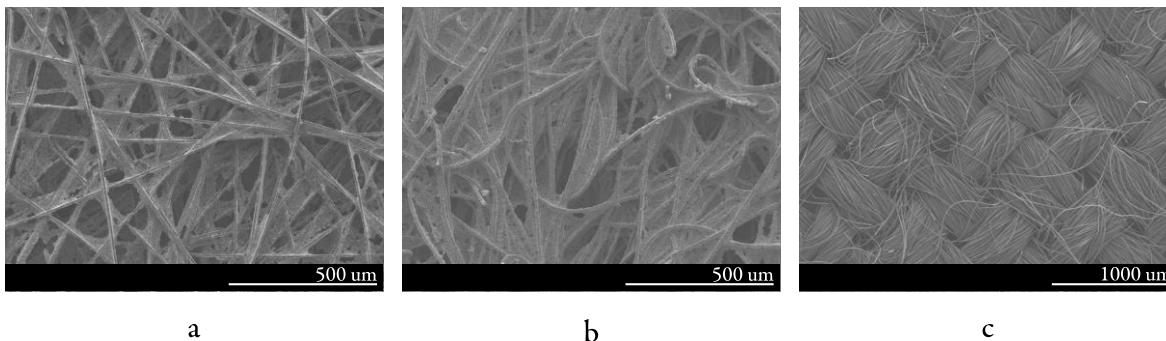


Figure 6: SEM images of different PTL types: paper (a), felt (b) and cloth (c).

PTL substrates are fabricated from chopped carbon fibres, derived from solvent spun polyacrylonitrile (PAN) copolymer; which are subsequently processed with paper-making or textile forming technology. Further processing may entail carbonization, resin impregnation, particle filling, moulding, and/or graphitization steps. As a final manufacturing step, substrates are usually impregnated with PTFE to enhance and stabilize the material's hydrophobicity. Mathias et al. offer more detail [34].

The MPL was originally developed to reduce membrane mechanical damage from adjacent functional layers; but it was also found to improve water management within PEM fuel cells. Conventional manufacture entails dispersions of carbon or graphite particles in polymer binder applied to substrates by any number of means; with subsequent sintering to fuse the unit. The result is an approximately sub-50 μm thick hydrophobic layer, possessing minute pores but also surface defects of larger size. The granular or clay-like structure, which contrasts the substrates of Figure 6, is illustrated in Figure 7.

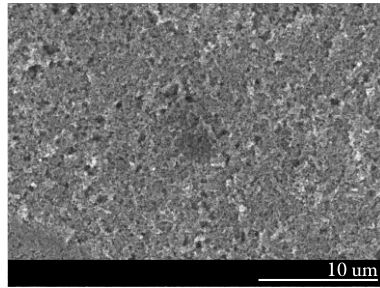


Figure 7: SEM image of MPL.

The design parameters available to the fuel cell assembler are limited. They may comprise: thickness, MPL presence, and PTFE content.

2.2 Transport layer transport

This section introduces in greater detail the energy and mass transport mechanisms interacting with PTLs. The porous structure of the PTL comprises a solid (carbon, binder and optional PTFE) and a void phase. General porous media can be described porosity and tortuosity. For PTLs it is appropriate to also consider fibre diameter and arrangement.

The interaction between morphological parameters and their resulting transport characteristics may be approximated by effective medium theories. A general theory to determine the effective transport coefficients in either: randomly assembled conductive fibers in non-conductive matrix; or non-conductive fibres in conductive matrix; has been developed by

Tomadakis, Robertson and Sotirchos [35–38]. Using Monte-Carlo simulation scheme, they based their method on the mathematical analogs of Fick’s second law of diffusion in order to represent generalized transport-structure effects via formation factor. Their theory is particularly attractive for modelling PTLs due to its: composition of fibres, and accommodation of fibre orientation. It has already seen application in describing PTL anisotropic fluid permeability [39]. However, this theory (and others from the literature) has not been developed to consider within-plane preferential fibre alignments. Moreover, there is missing treatment of the interactions between fibres, which may dominate conduction in the solid phase. Finally, a general weakness of effective medium theories is the translation of solid phase transport data to void phase transport data and vice versa.

2.2.1 Energy transport

Transport of electric charge to and from the CLs is required to sustain the electrochemical reactions. In addition, there must be thermal management to ensure cells remain within their temperature envelopes. In automotive scale fuel cell systems, excess heat must be removed from the cell; in smaller research scale cells, heat must often be introduced. PTLs transmit both electrical and thermal energy between CLs and BPPs. In the case of electrical transport, electrons are transmitted through the carbon fibre network. In the case of thermal transport, there is transmission through both the fibre network and via the fluid within the void phase.

Within the fibre phase, electrical and thermal transport are governed by Laplace’s equation; modeling solutions are challenged by: geometric complexity, what constitutes credible geometry, material heterogeneity (i.e. carbon versus binder or PTFE), and treatment of the inter-fibre connectivity. Adding the fluid contribution to thermal energy transport requires knowledge of the mass-transport and phase-change processes; which are themselves functions of PTL material and structure – and fuel cell operating point. Although some studies (experimental and modelling) attempt to incorporate a liquid water contribution, there remains uncertainty in whether the forced distributions are realistic. The outcome is that the energy transport properties of PTLs are predominantly determined experimentally ex-situ and dry, see section 2.3.

2.2.2 Mass transport and water management

PEM fuel cells operate effectively only within a narrow envelope. For effective reaction kinetics elevated temperatures desired, but these are limited to typically 100°C by membrane stability [40]; the temperature (and pressures) permit the existence of liquid water within a cell. This product water coexists with, and generally obstructs, the gaseous reactant transport required to sustain the electrochemical reactions. Water management is a major field of

research for PEM fuel cells [41]. Its importance relates to membrane hydration and electrode flooding. Contemporary PEMs require hydration to obtain useful proton conductivities. Excess water in the MEA however may lead to flooding; where liquid water inhibits reactant transport to CL reaction sites and results in greater mass-transport overpotentials. Regulating water is non-trivial, water transport mechanisms present in PEM cells include:

- Electroosmotic drag, where water molecules are carried along by protons as hydronium and hydration shells from anode to cathode.
- Diffusion, where water moves from areas of higher activity to lower activity (e.g. from cathode to anode through the membrane).
- Hydrodynamic transport, where bulk pressure differentials drive flow (e.g. across the membrane due to uneven pressure drop along flow-field channels).
- Water vapour convective transport, where water is carried by gaseous species.
- Capillary water transport, where water is transported or inhibited by surface energy phenomena. Its description in PEM fuel cells is complex due to: finite size and structure effects; and heterogeneous wettabilities.

Although not featured in the present thesis, MPLs are commonly applied to regulate water transport. Together with the PTL substrate, they modify performance by altering the nature of mass fluxes (most notably at the cathode), but there is currently no agreement upon the exact mechanisms. Explanations proposed in the literature include:

- MPLs promote (or wick) liquid water transport out of the CL and into the PTL [42]. It is suggested this occurs as a result of liquid water seeking equilibrium capillary pressure in two media. Greater mass-transport impediment may be expected of the PTL, and lower from the CL.
- Similar to above, water vapour is transmitted from the CL, through the MPL, and condenses in the PTL [43]. The hydrophobicity of the MPL then inhibits liquid phase transport back into the CL.
- MPLs promote liquid water transport out of the CL via focused conduits in the PTL [44]. These dedicated conduits leave the remainder of the PTL unsaturated with liquid water, and therefore conducive to gaseous species transport. Greater mass-transport impediment may be expected of the CL, and lower from the PTL.
- MPLs fundamentally inhibit liquid water transport into the cathode PTL where it would otherwise create mass-transport resistance [45]. Liquid water instead hydrates the membrane and departs the MEA through the anode.

It may be all these possibilities, with different weighting depending upon operating conditions. Further complication arises from the current density dependent rate of water production at the cathode. At low currents, without humidified reactant feeds or water retaining PTLs, cells are prone to dehydrate. At high currents, cells are prone to flood without concerted water removal effort.

The mass-transport of reactants through the PTLs (from the BPPs to CLs) is governed by Fick's diffusion. Where the effective diffusivity may be estimated by:

Equation 13
$$D_{eff} = \frac{\phi}{\tau} D(1 - s_w)$$

Where the open diffusivity of a pair (e.g. O₂ in N₂) is scaled by: the fraction of void space not occupied by liquid water; and by the convoluted path through the layer. As implied in the water management discussion above, the challenge is quantifying the value of s_w .

2.3 Transport layer characterization techniques

Comprehension of PEM fuel cell transport layer function is challenged by an ambiguous structure-property-performance relationship. The first link in this relationship establishes the properties of the PTL as a function of morphological and material composition; the second link establishes expected in-situ performance as a function of layer properties. The important parameters in each group and the mechanisms which interlink them are the subject of contemporary research. The mechanisms by which PTL design interacts with in-situ performance are not easily quantifiable. Contemporary experimental works elucidating the mechanisms are constrained by limited (in number and data quality) in-situ diagnostic techniques and ex-situ techniques which may oversimplify the problem. Contemporary modelling work is often constrained by oversimplification of the multi-scale, multi-phenomena problem and a lack of quality input data.

Refinement of experimental methods is vital to PEM fuel cell development. This section overviews established and experimental techniques in the literature to contextualize later chapters, see [9,46] for additional information.

2.3.1 *Electron microscopy techniques*

SEM is commonly used to visualize surface topology and MEA layer cross-sections [47]. For fibrous structures, it may be used to measure fibre diameters and estimate porosity. Energy-dispersive x-ray, often available in SEM machines, permits spatial analysis of composition; however resolution and species identification can be inadequate (e.g. distinguishing carbon

from fluorine). Transmission electron microscopy often finds use in characterizing supported catalysts. Individual catalyst particles are perceptible and their distributions may be quantified [46].

2.3.2 General and electrochemical techniques

Polarization curves are omnipresent in PEM fuel cell research. They may be generated for a complete or half-cell. These curves exhibit domains of kinetic, ohmic and mass-transfer dominance from which critical parameters (e.g.: exchange current density, cell resistance and limiting current density) may be extracted.

Electrical impedance spectroscopy (EIS) facilitates elucidation and approximate quantification of catalytic activity and reaction mechanisms [48]. Demonstrations of its applicability to mass-transport and flooding characterization are available [49]. More straightforward, the high-frequency resistance (HFR) delivers cell direct-current resistance.

Anode water removal methods apply increasing anode flow rates to stimulate diffusion transport of water from cathode to anode and out of the cell [50]. The method may be used to determine the presence of cathode flooding and to isolate its contribution to mass-transport overpotential.

Cyclic voltammetry facilitates in-situ or ex-situ qualitative assessment of reaction mechanisms and catalyst performance. Reversibility, degradation, kinetic rates, and electrocatalytic surface areas may be estimated [9]. Cyclic voltammetry can also serve as an accelerated degradation mechanism; the author has published in this discipline [51].

2.3.3 Ex-situ techniques

While not direct PEM fuel cell performance measurements, ex-situ techniques may characterize constituent layer design and/or function. Consideration is required for functional layer construction and how the ex-situ environment may or may not reflect the in-situ environment (e.g. the influences of anisotropy [44] and compressive strain).

Brunauer-Emmett-Teller theory is an adsorption isotherm providing means for specific surface area measurement; dedicated equipment provides energy of adsorption and monolayer coverage data from which area is estimated. Extending the measurement to multilayer adsorption allows estimation of pore size distribution via additional theory.

CL catalytic area may be estimated from carbon-monoxide chemisorption analysis. Metered CO is fed to a sample where it binds to Pt sites; when such adsorption ceases, the quantity of adsorbate correlates to catalytic area.

Thermal conductivity measurement of functional layers may be acquired in-situ or ex-situ. In-situ acquisition may be obtained from temperature sensors embedded within the MEA [52]. Whereas ex-situ measurement have been demonstrated with dedicated test apparatus (e.g. guarded heat flux meters) [53–59].

Electronic conductivity of the PTL can often be overlooked as the membrane is a dominant (ionic) impediment to charge transport. Through-plane bulk and PTL-BPP electronic contact resistances may be acquired with two or four point probe (2PP or 4PP) apparatus [60–64]. While PTL-CL resistances have been estimated using H_2/H_2 cells [65]. In-plane resistances might be measured using four-point probe (4PP) apparatus following the corrections of Smits [66].

Liquid, gas and two-phase permeability coefficients of Darcy's law can describe pressure driven transport through the PTL structures. Techniques generally impose a known flow rate through a sample and measure the resultant pressure drop, examples are offered in [62,63,67,39,68–73,43]. Vis-à-vis modelling, the Tomadakis-Sotirchos(-Robertson) model offers a structure aware solution [35].

2.3.4 Water management techniques

Water management research comprises capillary and interfacial property characterization of PTLs. However fallacies can exist in this literature [74]. The problem centres on the real structure of materials. The general Young-Laplace equation describes the pressure differential across an arbitrary curved fluid interface; meanwhile ubiquitous simplifications (viz. Washburn equation) are only strictly applicable to straight cylindrical capillaries. Washburn applied Young-Laplace and Poiseuille relationships to describe the dynamic uptake of a wetting fluid into a single capillary and bundle of capillary tubes of different radii [75]. Other less-than-ideal relationships in PEM fuel cell literature were originally developed for geological formations [76]. The fibrous structure of PTLs is different from a bundle of capillaries or a granular medium. A summary of common techniques follows, further reading exists in [77].

Porosimetry is the determination of total pore volume and pore size distribution of a sample. Conventional techniques include mercury intrusion porosimetry and method of standard porosimetry. For the reasons above, translation of pressure to radius data via the Washburn equation lends these methods questionable accuracy.

PTL contact angles and surface energies may be estimated from multiple approaches. Sessile drop and Wilhelmy type techniques are the simplest [63,43,78,79]; however results are only applicable to the interface (i.e. PTL-MPL and PTL-flow-fields). This is due to the heterogeneous surface topography and composition. Internal structure contact angles and surface energies may be estimated from Washburn imbibition or single-fibre Wilhelmy experiments [79,80]; these may be subsequently generalized via Zisman plots and Owens-Wendt theory.

Capillary pressure versus liquid saturation curves may be experimentally acquired for a PTL configuration and applied directly in modelling. Procedures involve either pressure or volumetrically controlled intrusion and drainage of liquid (e.g. water), ideally cycled to observe hysteresis [44,71,72,81–86]. Simpler approaches can determine breakthrough pressure alone [67,87].

Visualization techniques are more qualitative for comprehending PTL behaviour. Experiments have been conducted in-situ, in simulated flow-fields, and in complete isolation ex-situ. Imaging approaches include: conventional microscopy[88–90], fluorescence microscopy [91], environmental SEM [92,93], and nuclear imaging [94].

2.4 Transport layer strategies

Compared to the CL and membrane, PTL development is restricted. Efforts are generally limited to modifications of commercial substrates and/or permutations of MPL composition. Empiricism is the means by which PTLs are developed and selected for application. Strategies in the literature for improving PEM fuel cell performance through PTL design follow:

PTFE impregnation to increase hydrophobicity is ubiquitous. It is commonly suggested that the process produces a network of hydrophobic and hydrophilic channels conducive to gas and liquid transport respectively [74]. Dissenting hypotheses suggest the result is a medium with neutral wettability where transport behaviour is dominated by structure [86]. The outcome is a reduction of PTL saturation and improved mass-transport. Other means of hydrophobizing include fluorinated ethylene propylene and, more experimental, tetrafluoromethane plasma treatment [95].

Other modifications to PTLs include micro-machining of channels and/or perforations, so as to create dedicated water transport conduits [94,96]. Consideration is required for the choice of micro-machining technique; it was found laser milling degraded hydrophobicity about cut features, to detrimental effect for the cell.

Alternative composition or additives for MPL fabrication have been explored. Kannan et al. studied the use of nano-chain carbon and multi-wall carbon nanotubes as the carbon MPL component [97,98]. Lin et al applied vapour-grown carbon fibres with dispersion agent in the MPL ink and found improved performance versus their baseline MEA in single cell tests [99]. Chun et al. used pore-forming agents in the ink to produce MPLs of variable porosity [100]; it was determined the process generated mostly macropores, with the optimum quantity dependent upon PEM fuel cell operating conditions. Schweiss et al. incorporated hydrophilic aluminosilicate cylinders in the ink to impart wicking behaviour out of the CL [101]; improved performance was observed especially at higher humidification and current densities. Quite unusual, Hiramitsu et al. applied a dry-deposition technique using comparatively little material and yielding a more granular versus mud-cake appearance of the MPL [102].

Dedicated water management layers feature in studies of perforated graphitic [103,104] and metal sheets [105] positioned within or about the MEA. Other designs have utilized hydrophilic polyaniline interlayers to retain moisture in the CL [106]. More radical, Buie et al. integrated active electroosmotic pumping structures at the cathode [107]; they noted a net increase in maximum power density upon activation of the pumps.

One may also identify a category of composite PTLs. Antolini et al. describe PTLs with MPLs applied to both faces of the substrate [108]. It was observed at low current densities, the properties of the MPL adjacent to the CL determined performance; while at higher current densities, the exterior MPL became relevant to cell performance. Chun et al. produced a double layer MPL where the confined layer was less hydrophobic (they incorrectly called it hydrophilic) than the layer adjacent to the CL [109]. Improved performance was observed versus a baseline PTL; however their argument is contentious.

Next are examples of gradient MPL properties in the through-plane direction. Tang et al. produced a PTL with triple-layer MPL of decreasing porosity in the direction of the substrate via pore-forming agent addition [110]. Improved performance versus non-gradient MPL equipped cells was noted, especially at higher current densities; but their rationale is contentious. Kannan et al. produced a quadruple-layer MPL, to increase hydrophobicity towards the substrate, by varying PTFE and carbon particle morphology distributions [111]. Higher limiting current and peak power densities were observed with the functionally, as opposed to porosity, graded MPL in air breathing cells; but baseline equivalent performance was noted with pure O₂ operation. Similarly, by PTFE content variation, Weng et al. produced triple-layer MPLs with gradient wettability hydrophobic towards the substrate [112]; the performance benefit was shown to be a function of individual layer PTFE contents and PEM fuel cell operating condition, necessitating application specific optimization.

Unorthodox PTL solutions exist which completely eschew conventional materials and/or manufacturing techniques. Tang et al. and Du et al. describe similar means of producing a hybrid PTL/CL [113,114]; a layer of carbon nanotubes is grown upon a commercial PTL substrate by chemical vapour deposition, then sputtered with Pt. It was thought the non-catalysed nanotubes trapped within the structure effect the role of an MPL. Chen-Yang et al. produced homogeneous PTLs by calendaring and pressing mixes of carbon black and PTFE [115]; these demonstrated half the performance of commercial PTL solutions. The same group later attempted the addition of carbon nanofibres to the mix and found improved, but still less than baseline, performance [116]. Comparably, Gao et al. produced PTLs by sintering a mixture of carbon nanotubes, PAN carbon fibres and PTFE [117]; they observed superior mass-transfer and electronic conductivity versus a commercial Toray product. Metal PTLs have been explored in various morphologies including perforated sheets [118,119], meshes/cloths [120,121], foams [122], and metallized polymers [123]. Campbell et al. proposed the use of glass-fibre networks filled with conductive media [124]. Yakisir et al. describe PTLs created by selective dissolution of phases from an immiscible two polymer composite film [125,126]; in-situ test results are not published, but ex-situ characterization reveals lower electronic conductivity versus commercial PTLs.

Finally, through a fuel cell there exist gradients in species concentrations, reaction rates, pressure and temperature. An optimal PTL might therefore vary in function across the active area. Wood et al. employed a segmented cell to study the performance of a collage PTL of different PTFE contents, observing an improvement in current density at moderate cell potential [127].

The novel PTLs introduced as part of the present thesis are entirely different from the above, distinguished by their manufacture via electrospinning technology. Also distinct is the integration of nanoscale design, which is prevalent in CL development, but comparatively absent from transport layer literature.

2.5 Electrospinning applications in PEM fuel cells

The application of electrospinning towards PEM fuel cell technology has thus far been directed at CL and membrane development; Cavaliere et al. [128] and Dong et al. [17] offer reviews for general energy applications. A literature survey was conducted on electrospinning's application in CLs and PTLs. CL literature is reviewed in Appendix B. Only two works pertaining to PEM fuel cell transport layers [129,130] were identified; their scopes and contributions were limited and are addressed in Chapter 6 .

3 Experimental

The general experimental section complements the methods outlined in later manuscript-adapted chapters.

3.1 Materials

The materials used in the research supporting this thesis are listed in Table 2.

Table 2: Materials used in the present thesis.

Item	Supplier	Notes
CCM	W. L. Gore & Associates	
PTL	SGL Group	Various types
PAN	Scientific Polymer Products	150000 Mw
DMF	Fisher	Certified ACS
Air	Praxair or diving compressor	Breathing grade
Nitrogen	Praxair	4.8
Argon	Praxair	5.0
Hydrogen	Praxair	5.0
Water	Barnstead E-Pure 1090	$\geq 18 \text{ M}\Omega\cdot\text{cm}$

3.2 Apparatus

3.2.1 Electrospinning

Electrospinning is performed using one of two systems. The first is Kato tech Co. (Kyoto, Japan) NEU Nanofiber Electrospinning Unit. Principal features are: horizontal spinning orientation; 0.33 m long, 0.15 m diameter rotating drum target; syringe needle capillary tip; capillary horizontal translation; and 0-40 kV power supply. Figure 8 is a photograph of the system.



Figure 8: Photograph of NEU electrospinning apparatus.

The second is MECC Co. (Ogōri-shi, Japan) NANON Electrospinning machine for laboratory use. Principal features are: vertical spinning orientation; 0.20 m long, 0.20 m diameter rotating drum target; 100-3000 rpm drum rotation speed; syringe needle capillary tip; capillary horizontal translation; and 0-40 kV power supply. Figure 9 is a photograph of the system.



Figure 9: Photograph of NANON electrospinning apparatus.

3.2.2 Fuel cell research cell

A new fuel cell research cell was developed by the author for this thesis. A new cell was required to allow testing smaller active area MEAs, a restriction imposed by synthesis limitations (viz. the diameter of tube furnace available for thermal treatments). The cell was developed in-house, as commercial small cells did not offer features consistent with the group's pre-existing larger-sized platform. Principal features of the cell include:

- 15x15 mm² active area, adaptable from 10x10 to 30x30 mm² with new BPPs. BPPs are machined from Eisenhuth Melange D blanks.
- Aluminium Pneumatic bladder for consistent and homogeneous cell compression.
- Polyetherimide polymer hybrid fixture and manifold to reduce heat loss (thermal bridges).
- Thermocouples positioned at BPPs for accurate cell and inlet gas temperature control.
- Liquid thermal regulation (hot/cold) integrated into BPP verso to reduce number of inter-component interfaces.
- Additional manifolding to permit future reference electrode integration.

Figure 10 is a photograph of the compression hardware; Figure 11 is a photograph of a fitted MEA and BPP (post-experiment).

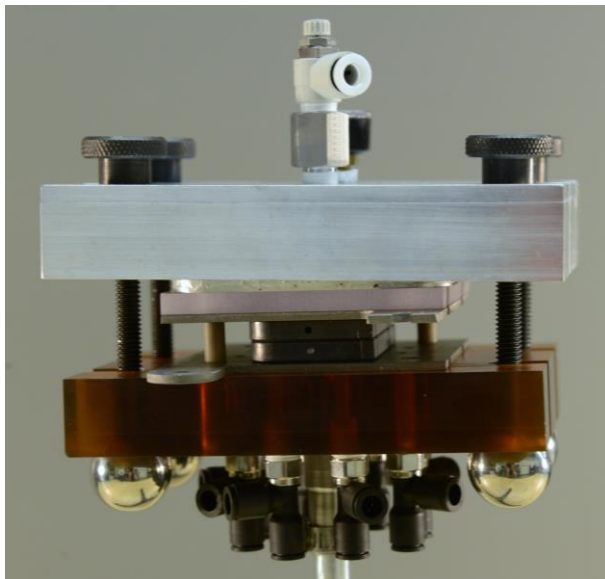


Figure 10: Photograph of research cell compression hardware. The graphite pieces are not the final BPPs.

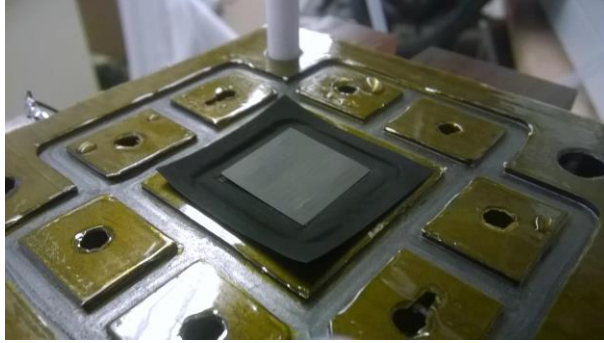


Figure 11: Photograph of MEA and BPP in small cell hardware.

3.2.3 Fuel cell test station

A Greenlight Innovation G20 fuel cell test station was procured for this thesis. It was specified explicitly for smaller active area cells ($\leq 49 \text{ cm}^2$) with a customized loadbank capable of potentiostatic operation. Principal features include:

- Greenlight 80 A loadbank with zero volt option.
- Bi-functional air/ O_2 cathode mass-flow controller (2.0 NLPM, 100:1 turndown).
- N_2 /He cathode mass-flow controller for in-station mixed nitrox/heliox (1.5 NLPM).
- Bi-functional H_2 / N_2 anode mass-flow controller (1.5 NLPM).
- Bubbler style reactant humidification.

Apart from the loadbank and flow controllers, the system features standard options. Figure 12 is a photograph of the station.

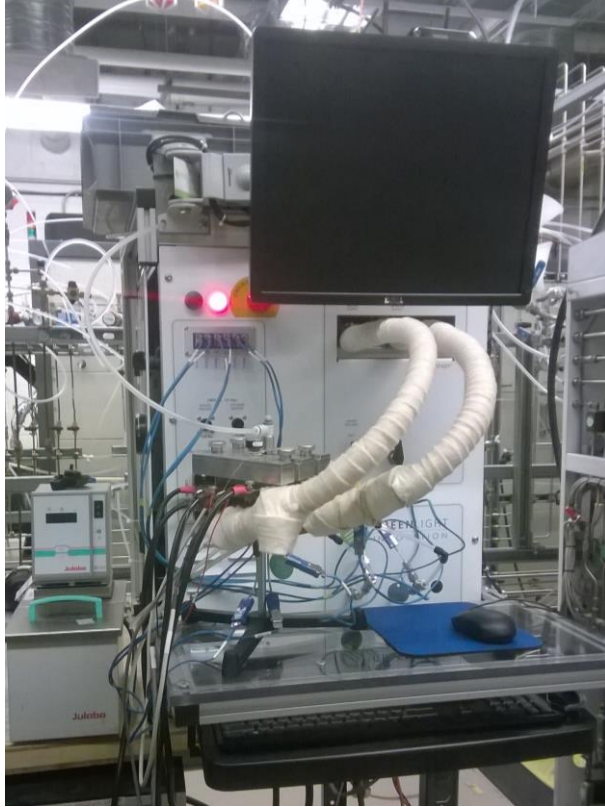


Figure 12: Photograph of fuel cell test station.

4 Three-dimensional electronic resistance of PEM fuel cell transport layers

We report on a method and apparatus for the determination of the three-dimensional electronic resistance of PEM fuel cell PTLs as a function of compression. Attention is given to the anisotropic nature of the fibre-based materials; between through- and in-plane directions and the differences within in-plane. For the first time, in-plane resistivities are resolved as functions of strain with a square 4PP arrangement; these are acquired in multiple directions to determine the principal components of resistivity. Through-plane information is acquired with a linear 4PP apparatus with concurrent capture of sample stress and strain. Results are presented for a selection of PTLs of different PTFE contents and thicknesses. In-plane resistivities exhibit linear decreases in resistivity with increasing compressive strains. We estimate an order of magnitude lower resistivity in-plane versus through-plane. Further, we reinforce that anisotropy in-plane undermines the validity of reports based on two or less measurements. Three methods are presented and compared for analysing data in the through-plane direction. We demonstrate the limitations of common assumptions regarding contact resistances and of using PTLs of different thicknesses. It is proposed that a total area resistance approach is presently the most accessible and communicable metric for the fuel cell community.

4.1 Introduction

Proton exchange membrane fuel cells and hydrogen are a bridge between renewably sourced primary energy and end-user applications, with particular interest for automotive use. Though reversibly very efficient, PEM fuel cells suffer operating losses which may be categorized into kinetic, ohmic, and mass-transport. The ohmic loss is the product of net current and cell resistance, which may be subdivided into contributions from individual cell components and

their interactions. In practice, these are functions of: cell materials and design, assembly methods, and operating parameters. It may also be insufficient to describe ohmic losses as an exclusively one-dimensional problem (in space, normal to the active area). Due to gradients (e.g.: temperature, potential, humidity, etc.) across a cell active area, the resistance and current density becomes functions of local environmental and mechanical conditions [131].

Though the predominant resistance contribution in a PEM device may arise from the ionomer phase, the contribution from the PTLs may still be correlated to cell performance [34]. We report on a method and apparatus to determine the three-dimensional anisotropic components of electronic resistance of PEM fuel cell transport layer material under different states of mechanical compression. Results are presented for several commercially available materials. Owing to a non-random three-dimensional distribution of constituent fibres, PTLs can not be described as isotropic; however this is often how their electronic resistivity is modelled. Our treatment of anisotropy acknowledges the differences in current transport over three orthogonal directions which includes resolving within in-plane. Further, we illuminate deficiencies of contemporary literature by replicating published methods and appraising results. Lastly, though significant inter-fuel cell component contact resistances have been reported [60,63–65], this study targets a description of the PTL material itself (bulk or intensive, of the carbon-void space composite). This is rationalized by suggesting that bulk data are more pertinent for the wider PEM fuel cell community versus contact data. Whilst still important, the latter may be much more a function of individual cell design than the former (e.g.: bipolar plate material and topology; and functional layer assembly). We are motivated by the need to establish PEM fuel cell material characterization techniques as industry presses for standardization. Information arising from such techniques at the isolated, ex-situ, component level can facilitate the communication between fuel cell systems manufacturers and component vendors.

4.2 Background

A coordinate system is required to describe three-dimensional material properties. In the present study: x and y directions are within the plane (in-plane) of the layer, and z is normal to the plane (through-plane). x and y are aligned with the cut edges of a given sample. Further, the manufacturing process establishes machine (MD) and cross-machine (CD) directions, which are taken to be aligned with the edges of supplied sheets. Finally, fibres may be preferentially aligned and not necessarily coincident with MD [132,133]; therefore fibre-aligned (FAD) and fibre-cross (FXD) directions exist. These directions are summarized in Figure 13.

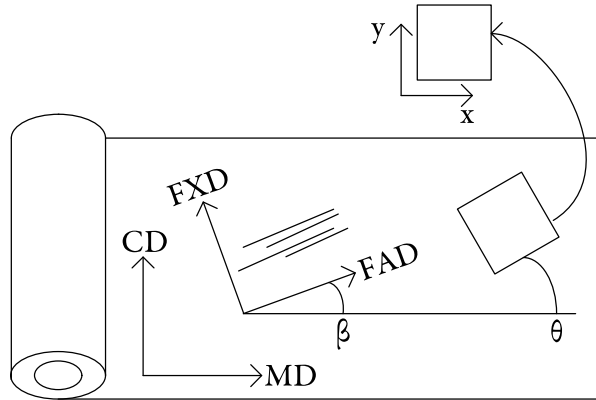


Figure 13: Coordinate system and important directions used in this study.

The importance of a through-plane electronic path is apparent, as current generally flows between the CLs and bipolar plates. The in-plane continuity is however also critical, because the contact between PTL and bipolar plates is non-continuous over flow-field lands and channels. Current is carried from the CL regions exposed in the channels, along the PTL, and into the bipolar plates at land regions. It is surmised the thin films used in CLs are inefficient conductors for this purpose due to their narrow geometry and higher resistivity [134]. Additionally, operating gradients in a fuel cell may give rise to net currents across the active area carried by the parallel paths of CL, PTL and bipolar plates.

The in-plane resistivity of paper based PTLs has been reported over an order of magnitude less than that of the through-plane direction [34]. Cell modelling work has identified the importance of this characteristic for electronic resistivity [135,136] (assuming a unique in-plane value) and for related thermal resistivity [137] (fully anisotropic). The difference through-versus in-plane may be attributed to the fibre structure of the layers. In-plane conduction benefits from current travel along fibres, whereas through-plane conduction requires current travel across inconsistent fibre-to-fibre contacts. Following the argument of fibre alignment, it stands to reason that different resistivities would be observed along different in-plane directions for a non-random fibre distribution; this raises implications for transport layer orientation strategy during cell assembly. The relative orientation of preferential fibre direction to bipolar plate geometry may impact fuel cell performance [138,139].

Acquisition of planar material resistance in the through-plane direction is often achieved by interposing a sample between two plates (anvils) and measuring the voltage as a known current is applied. The configuration of electrical leads directly impacts what resistances are actually measured. Pertaining to PEM fuel cell PTL characterization, 4PP measurements have been applied with leads bonded to said anvils [60–62]. While a 4PP measurement is superior to the

two-point equivalent, in that measurement system contributions are eliminated; when current and sense leads share the anvils, sample-to-anvil contact resistances are included in the measured resistance. An alternate 4PP approach applies micro-electrodes for voltage sensing directly at the PTL which excludes contact resistance effects [140]. Here the challenge lies in implementing sufficiently small micro-electrodes, such that the perturbation in the current distribution about the electrode is minimized. Moreover, as the micro-electrodes approach the length scales of PTL structures, structural inhomogeneities may distort measurement. The two configurations for through-plane resistivity acquisition are illustrated in Figure 14.

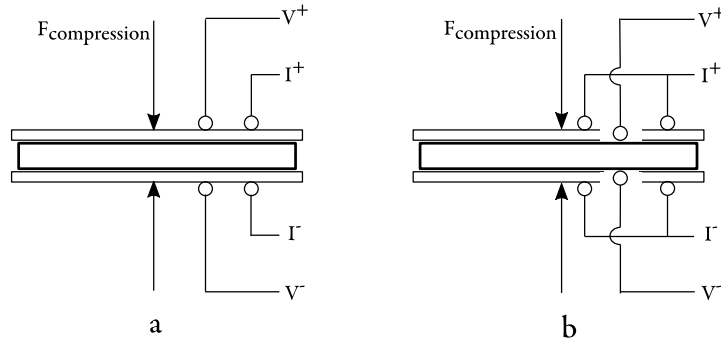


Figure 14: Illustration of through-plane 4PP electrode arrangements in conventional (a) and micro-electrode (b) configurations.

Unlike the electronics literature where resistivity characterization is facile, the fuel cell community is lacking adequate methods to measure the through-plane property of its PTL materials. Equation 14 describes the observed resistance when using an electrode arrangement as illustrated in Figure 14(a):

Equation 14
$$R_z = 2R_{PTL-anvil} + \rho_{z'z'}A^{-1}t$$

This equation may be applied to estimate contact resistance when the bulk resistivities are known a-priori [141,142]. Were bulk resistivity unknown, it could be obtained via a supplementary measurement with another, thicker, specimen or using an altogether different geometry (e.g. a slender wire effecting one-dimensional behaviour). This is not possible with PEM fuel cell PTL materials at the consumer level; the available products are restricted in geometric diversity. As such, it is not readily possible to distinguish contact (be it from ex-situ measurement apparatus or in-situ between cell components) from bulk material resistance contributions in the through-plane direction. Approaches to resolve this problem exist in the literature, three of which are adopted and compared in this study (see Section 4.3.3). Briefly, the first comprises assumptions about negligible contact resistances in the measurement

method; the second utilizes what different thickness PEM fuel cell materials are available; the third includes contact resistance in the reported property.

Acquisition of planar material resistivity in the in-plane direction may be achieved with linear arrangements of electrodes upon a sample. More approachable than through-plane measurement when applied to PTLs; results using two-point probes have been reported [138], though more common are 4PP measurements [34,60,140,143] which might apply the geometric corrections developed by Smits [66] to convert the measured resistance to material resistivity. Some of these studies attempted to capture the anisotropic components of in-plane resistivity [60,138,140]; though none considered the implications of misalignment between MD and FAD, nor was the application of a linear 4PP arrangement ideal for a sample exhibiting anisotropy – the method of Smits assumes isotropic resistivity. A general solution which might be applied more generally was offered by Wasscher [144]. Wasscher, following the ideas of van der Pauw [145], demonstrated the mapping of an anisotropic sample to an equivalent isotropic sample; but concludes that a linear 4PP is less sensitive for detecting anisotropy than a rectangular (or square) arrangement of electrodes. The alternative square 4PP method, as rendered by Montgomery [146], builds on the works of van der Pauw and Wasscher to provide a means of determining the resistivities of an anisotropic material. The square arrangement is advantageous owing to: its greater sensitivity, tolerance in electrode positioning, and the ease of making two orthogonal measurements by only switching voltage and current leads. Figure 15 illustrates the linear and square 4PP configurations.

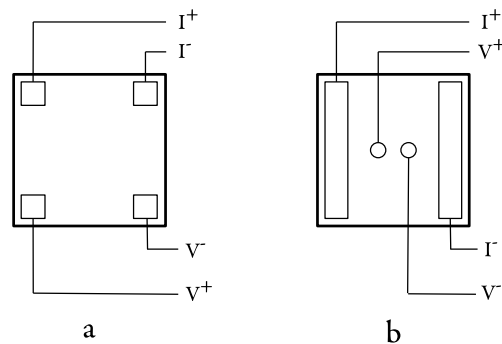


Figure 15: Illustration of in-plane 4PP electrode arrangements in square (a) and linear (b) configurations.

Application of the Montgomery method to PEM fuel cell PTLs has been reported by Morris and Gostick [132]. These authors also considered possible disagreement between MD and FAD, and suggested repeating x and y measurements for samples cut at 45° to each other to capture the principal resistivity values and the angle separating MD and FAD. Note that

knowledge of resistivity in two (arbitrary) directions alone is insufficient to determine the principal values or directions. While the authors established the compressive force of electrodes against a sample was non-important, they did not explore the effect of compressive force upon the sample itself.

Conventional PEM cell designs employ a compressive load in the through-plane direction to both connect and seal components. These loads impart strains in the fuel cell components, which in the case of PTLs may decrease the apparent resistivity of the layer. Of the aforementioned studies examining PTL resistance, several references [34,60–62,140] incorporated the effect of mechanical compression, reporting data as a function of applied stress. Assuming that the underlying cause for changes in resistivity is structural change, reporting values as a function of sample thickness (or strain) may be more useful than stress; which is clouded by any non-linearity in the stress-strain characteristic of the material.

The aforementioned publications investigating the electronic resistance of PTLs are summarized with the objectives of the present study in Table 3. Due to differences in methods and analyses an objective compilation and comparison of results is unfeasible. Reported data may or may not account for contact resistances from measurement apparatus or simulated bipolar plates. Data can also depend on the objective of a given study; if contact resistance itself is desired, the bulk PTL contribution might be: modelled, assumed constant, or otherwise tenuously estimated.

Table 3: Summary of experimental studies investigating PTL electronic resistance.

Authors	Through-plane method	In-plane method	In-plane anisotropy considered?	FAD vs. MD misalignment considered?	Through-plane compressive load considered?
Mathias et al. [34]	4PP 0.005-0.030 $\Omega \cdot \text{cm}^2$	linear 4PP 0.26-0.38 $\Omega \cdot \text{square}^{-1}$	N	N	only through-plane R
Ismail et al. [60]	4PP ~ 1000 $\Omega \cdot \text{cm}^2$	linear 4PP $1.6-4.0 \times 10^{-4}$ $\Omega \cdot \text{m}$	Y	N	only through-plane R
Chang et al. [62]	4PP 0.025-1.0 $\Omega \cdot \text{cm}^2$	n/a	n/a	n/a	only through-plane R
Escribano et al. [61]	4PP:10 stack 0.010-0.50 $\Omega \cdot \text{cm}^2$	n/a	n/a	n/a	only through-plane R
Kleemann et al. [140]	μ 4PP 0.004-.050 $\Omega \cdot \text{cm}^2$	linear 4PP $0.5-2.5 \times 10^{-4}$ $\Omega \cdot \text{m}$	Y	N	in- and through-plane R
Han et al. [138]	n/a	linear 2PP $2.4-4.8 \times 10^{-4}$ $\Omega \cdot \text{m}$	Y	N	fixed value, only through-plane R
Williams et al. [143]	n/a	linear 4PP $0.43-2.1 \times 10^{-4}$ $\Omega \cdot \text{m}$	N	N	N
Morris and Gostick [132]	n/a	Montgomery 4PP $0.6-3.58 \times 10^{-4}$ $\Omega \cdot \text{m}$	Y	Y	N
Todd et al. (this study)	4PP	Montgomery 4PP	Y	Y	in- and through-plane R

The present study distinguishes itself from the existing literature by identifying complete resistance information of PTLs as a function of through-plane compressive strain. This is done with special attention to resolving MD and FAD incongruity. To the authors' knowledge, this study is the first to report Montgomery 4PP acquired resistivities of PTLs under compression. We critically assess contemporary methods to resolve through-plane contact resistance effects; and propose, what we believe, is the best solution available within the constraints of the state-of-the-art.

4.3 Method

4.3.1 Materials

Commercially available transport layers are examined. The selection, tabulated in Table 4, comprises examples of different thickness and PTFE content. All samples of a given material are extracted from the same sheet. No materials feature microporous layers.

Table 4: PEM fuel cell transport layer materials evaluated in this chapter.

Manufacturer	Model	PTFE (wt%)	Specified thickness (10^{-6}m)
SGL SIGRACET	25 AA	0	190
	25 BA	5	190
	25 DA	20	190
	35 BA	5	300

4.3.2 Theory

The relationship between electric field and current density for arbitrary x, y, z directions is provided in Equation 15:

$$\text{Equation 15} \quad \vec{E} = \begin{bmatrix} \rho_{xx} & \rho_{yx} & \rho_{zx} \\ \rho_{xy} & \rho_{yy} & \rho_{zy} \\ \rho_{xz} & \rho_{yz} & \rho_{zz} \end{bmatrix} \vec{i}$$

The principal resistivities and their directions correspond to the eigenvalues and eigenvectors of the resistivity tensor. The present study assumes that the through-plane direction and z' are coincident, and that the other principal directions coincide with FAD and FXD. Subsequently, the resistivity tensor of Equation 15 may be rewritten as:

$$\text{Equation 16} \quad \begin{bmatrix} \rho_{xx} & \rho_{yx} & \rho_{zx} \\ \rho_{xy} & \rho_{yy} & \rho_{zy} \\ \rho_{xz} & \rho_{yz} & \rho_{zz} \end{bmatrix} = \begin{bmatrix} \cos(\alpha) & -\sin(\alpha) & 0 \\ \sin(\alpha) & \cos(\alpha) & 0 \\ 0 & 0 & 1 \end{bmatrix} \begin{bmatrix} \rho_{x'x'} & 0 & 0 \\ 0 & \rho_{y'y'} & 0 \\ 0 & 0 & \rho_{z'z'} \end{bmatrix} \begin{bmatrix} \cos(\alpha) & \sin(\alpha) & 0 \\ -\sin(\alpha) & \cos(\alpha) & 0 \\ 0 & 0 & 1 \end{bmatrix}$$

$$\text{Equation 17} \quad \alpha = \theta - \beta$$

, where θ is the angle between x and MD about z and β is the angle between FAD and MD about z . The tools presented for acquiring resistivity yield principal values only when

measurement axes are aligned with principal directions. To estimate the in-plane principal components without a-priori knowledge of FAD and FXD, resistivities at different θ are acquired and analysed (Section 4.3.4). Results of this study are presented in terms of principal values instead of rotated to match MD and CD. The assumption is MD to FAD misalignment may not be consistent over a production run (or cut sheet), and therefore the more condensed representation is chosen.

4.3.3 Through-plane resistance

Through-plane resistance is acquired from a purpose-built apparatus. The instrumentation comprises: 4PP arrangement bonded to polished gold plated anvils, load cell, LVDT displacement sensor, and regulated pneumatic cylinder. These are secured in a cylindrical body designed to ensure alignment and concentricity. Resistance is acquired with an Agilent 34420A micro-Ohm meter, while data acquisition is made with National Instruments hardware and the LabVIEW environment. Figure 16 is a composite photograph and schematic of the executed design. Combined displacement and load measurement allows resolution of resistance as functions thereof and stress-strain profiles. Samples have force applied step-wise; allowing equilibration before measurands are acquired (until there is no discernable change in observed resistance or thickness). To resolve strain as a function of stress, a strain-stress point cloud is compiled from all measurements of a given material and fit with a power-law function.

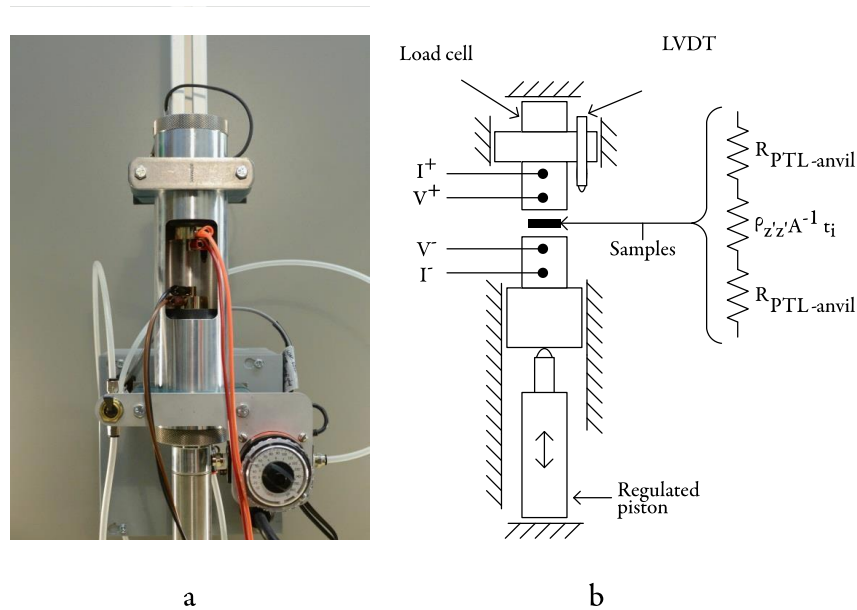


Figure 16: Photograph of through-plane resistivity apparatus (a). Schematic of through-plane resistivity apparatus (b).

As indicated earlier, a through-plane 4PP system whose voltage and current probes share anvils capture also sample-anvil contact resistance. Different methods may be taken to resolve the resistances; relying upon stacks of samples or samples produced in thicker size. Equation 18 describes the observed resistance of a stack of n PTL:

$$\text{Equation 18 } R_z = 2R_{PTL-anvil} + (n_{PTL} - 1)R_{PTL-PTL} + \rho_{z'z'}A^{-1}t$$

By using measured thickness, the present study is distinguished from other literature which may rely solely upon the number of discrete samples in a stack. Observations during development suggested using the number of samples in a stack and an average sample thickness was a sub-optimal approximation for t ; the discrepancy being attributable to variability over the PTL sheet and/or interaction between stacked samples.

One method (TP_METHOD_1) relies upon measuring progressively taller stacks of samples and making a linear fit to the data. This alone is insufficient to isolate any of the resistances; apparent from Equation 19:

$$\text{Equation 19 } R_z = [2R_{PTL-anvil} - R_{PTL-PTL}] + n_{PTL}[R_{PTL-PTL} + \rho_{z'z'}A^{-1}t_{average}]$$

, where for clarity t has been simplified by the number of stacked samples multiplied by an average thickness. A solution can be obtained if $R_{PTL-PTL}$ is assumed zero. Burheim et al. experimentally determined this was acceptable for analogous thermal resistivity (both phenomena being described by Laplace's equation) [54]. Nitta et al. [57] and Nitta et al. [147] argued, for thermal and electronic resistivity respectively, $R_{PTL-PTL}$ could be neglected if PTLs were sputter coated with conductive material. We are not convinced sputtering is an appropriate solution. Having attempted it ourselves, we did observe a drop in observed resistance; but owing to the open structure of the PTL, the process must have affected the bulk. Nitta et al.'s argument to the contrary is based on [148], but that study examined sputtering penetration into an un-catalysed carbon black and PTFE coated E-Tek PTL – not an uncoated SGL PTL. Upon the assumption that $R_{PTL-PTL}$ is negligible versus the PTL and PTL-anvil contact resistances (e.g. we approximate a stack of samples to a singular thick sample), measurements of stacked (un-sputtered) samples are performed. PTL resistivity is subsequently solved by fitting data to Equation 18; which is reconciled over a mechanical loading profile by treating $R_{PTL-anvil}$, $\rho_{z'z'}$ and t as functions of stress. Data analysis begins with three independent resistance-stress-thickness profiles acquired for each of x1, x2, x3, and x6 sample stacks. Individual profiles are linearly interpolated to a common stress abscissa. This yields for each stress: twelve values of R_z and t , with which a linear curve fit can be applied to

Equation 18 to extract PTL-anvil contact resistance and PTL resistivity. Error bars reported for through-plane resistivity are the 95% confidence bounds of the fitted parameters.

A second method (TP_METHOD_2) to isolate PTL resistivity for which we also provide data and analysis, leverages PTLs manufactured with similar PTFE treatment but different thicknesses. The same data from TP_METHOD_1 for SGL 25 and 35 BA, are used in a two-dimensional (t and n_{PTL}) fit of Equation 18. TP_METHOD_2 is distinguished from TP_METHOD_1 in that the different thickness materials allow closure of Equation 18 without neglecting any contact resistance terms. The different thickness materials disconnect the number of pieces in a stack (n_{PTL}) from the total thickness of the stack (t). We note that capitalizing on the aforementioned variability in PTL sheet and stack thicknesses of a single material is too small to effect the same.

A final method (TP_METHOD_3) does not distinguish between PTL-anvil contact resistance and sample resistance, and report instead the observed total area resistance. It is a compromise where precise bulk property information is forgone for the advantages of fewer measurements and ease of reproducibility. Fewer measurements are required, for our results we use x1 stack data alone. Reproducible, in that equivalent method and apparatus development are accessible to the general fuel cell community.

4.3.4 In-plane resistance

In-plane resistivity is acquired from a purpose-built apparatus. Instrumentation comprises: spring-loaded square 4PP arrangement, electronically non-conductive anvils, ultra-fine adjustment screw, and Mitutoyo digital indicator. These are secured in a rectangular frame, with mobile elements guided by four linear rails. Resistance is acquired with an Agilent 34420A micro-Ohm meter. The apparatus permits application of a prescribed sample thickness independently of the electrode seating force. Figure 17 is a composite photograph and schematic of the executed design.

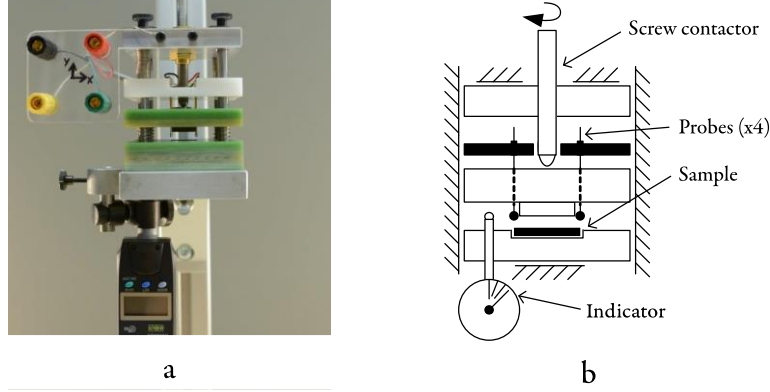


Figure 17: Photograph of in-plane resistivity apparatus (a). Schematic of in-plane resistivity apparatus (b).

Samples are cut with x directions at $0, 15, 30$ and 45° to MD using a rule die. For each sample, R_x and R_y resistances are measured for progressively decreasing thicknesses. The resistivities are determined by using the Montgomery method for a thin sample using the simplified expressions introduced by dos Santos et al. [149]. The anisotropic sample is first mapped to an equivalent isotropic sample with different edge lengths whose ratio is given by Equation 20:

$$\text{Equation 20} \quad \frac{L_{y^*}}{L_{x^*}} = 0.5 \left[\pi^{-1} \ln(R_y R_x^{-1}) + \sqrt{[\pi^{-1} \ln(R_y R_x^{-1})]^2 + 4} \right]$$

, written for the case where R_y is the greater resistance. The ratio is then applied to geometric corrections for a finite-sized isotropic rectangular sample to determine resistivities in x and y directions:

$$\text{Equation 21} \quad \rho_x = 0.125\pi t \left(\frac{L_{x^*}}{L_{y^*}} \right) R_x \sinh\left(\pi \frac{L_{y^*}}{L_{x^*}}\right)$$

$$\text{Equation 22} \quad \rho_y = \rho_x \left(\frac{L_{y^*}}{L_{x^*}} \right)^2$$

Three samples each are prepared for the aforementioned angles to MD. The outcome is three replicated multiple measurements of resistivity at $0, 15, 30, 45, 90, 105, 120$ and 135° to MD, enabled by the simultaneous capture of orthogonal pairs. These data are fit to an expression for resistivity as a function of θ and principal resistivities, derived from Equation 16:

$$\text{Equation 23} \quad \rho_\theta = 0.5(\rho_{x'x'} + \rho_{y'y'}) + 0.5(\rho_{x'x'} - \rho_{y'y'}) \cos(2\beta - 2\theta)$$

, where $\rho_{x'x'}$ and $\rho_{y'y'}$ are functions of strain and β is an unknown constant for the sheet of material. The principal resistivity components are determined as follows: linear interpolation of individual measurements to establish a consistent strain abscissa; an estimate of beta is made; fitting of Equation 23 at each strain to resolve $\rho_{x'x'}$ and $\rho_{y'y'}$; modification of beta to minimize the least-squares error between modelled and observed ρ_{θ} over the two-dimensional strain- θ space; repetition of fitting with modified beta until convergence. Error bars reported for in-plane resistivity are the 95% confidence bounds of the fitted parameters ($\rho_{x'x'}$ and $\rho_{y'y'}$). The present analysis is distinguished from those proposed by Morris and Gostick [132], in that the principal components are targeted directly and without invoking the concepts of anisotropy ratio nor van der Pauw average resistivity.

4.4 Results and discussion

PTL strain behaviour is presented in Figure 18. For materials of similar manufactured thickness, but different PTFE contents, we cannot discern any difference. The carbon substrates are surmised to be consistent by comparing thicknesses and the density of carbon in the bulk material via Equation 24:

Equation 24 $m_{carbon}V^{-1} = W_{areal}t^{-1}(1 - W_{PTFE})$

, which based on manufacturer data are consistent over the 25 series materials. The result suggests that addition of PTFE to this consistent PTL substrate does not alter layer stiffness. While we are unable to distinguish results for materials of similar PTFE content but different series (25 and 35); these materials may not be simply thinner or thicker versions of each other. The implications of this idea are probed further using resistivity results.

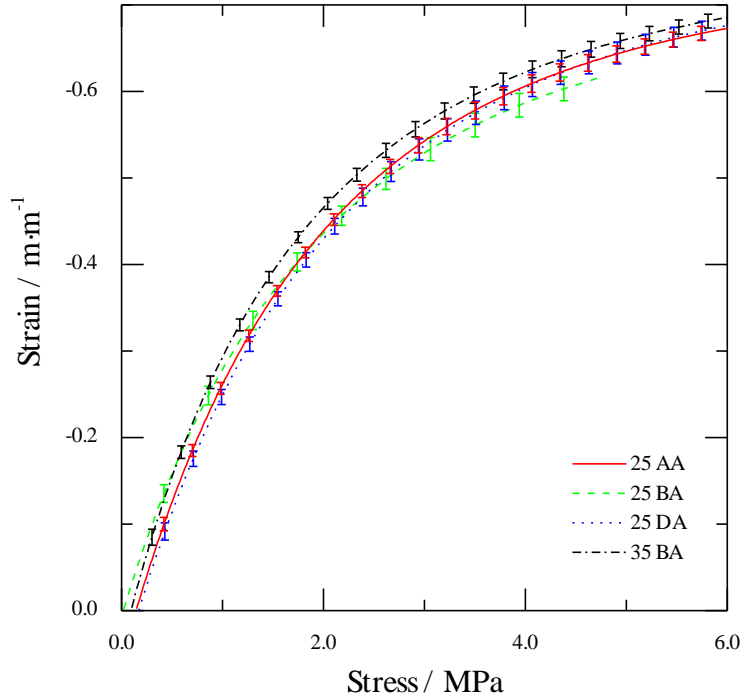


Figure 18: Compressive strain as a function of applied stress. Data are compiled from all through-plane measurements of a given material and fit to a power-law function; the error bars correspond to the 95% confidence bounds of the mean.

Figure 18 is developed from equilibrium data for only the first loading; not represented are creep (as layers equilibrate at load steps) and plastic deformation hysteresis information; these are considered outside the scope of the present study. Qualitatively however, as PTFE contents increase, greater lengths of time are required at a given load for strain and observed resistance to stabilize. We hypothesize this caused by PTFE redistribution as is undergoes mechanical creep. While measurements with cyclically applied load demonstrate an initial loading profile distinct from subsequent loading and unloading profiles.

Direct comparison of resistivities of different PTL models warrants caution. Our specific results are limited in an important manner: drawing samples from single sheets. Manufacturing batch-to-batch (and within-batch beyond our sheet) variability is not captured in the present study. We also do not report β 's, as-supplied sheets may not be cut in exact alignment with the manufacturing direction (i.e.: our defined MD and the real MD may not correspond).

In the following sections we report versus strain; this is distinct from other work which might report resistances versus other measures (e.g.: thickness, stress, even threaded fastener torque).

We argue the strain basis is more tractable for connecting PTL deformation to their resistivities. For example, the literature which reports resistivity as functions of applied stress can have results obfuscated by non-linearity and hysteresis in stress-strain behaviour.

4.4.1 Through-plane

Based upon TP_METHOD_1, the through-plane principal resistivities ($\rho_{z'z'}$) of the investigated PTLs are presented in Figure 19. At face value, the resistivities are decreasing with strain and there is a trend of increasing resistivity with PTFE content for similar thickness substrates. The quality of this method might be judged by examining the PTL-anvil contact resistance, which is calculated together with the resistivity, presented in Figure 20.

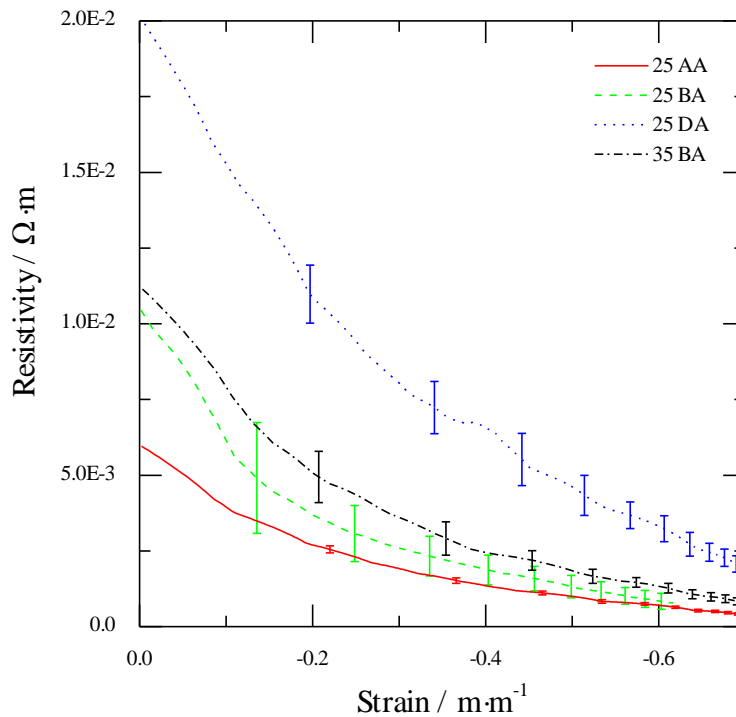


Figure 19: Principal resistivity through-plane as a function of PTL strain calculated via TP_METHOD_1.

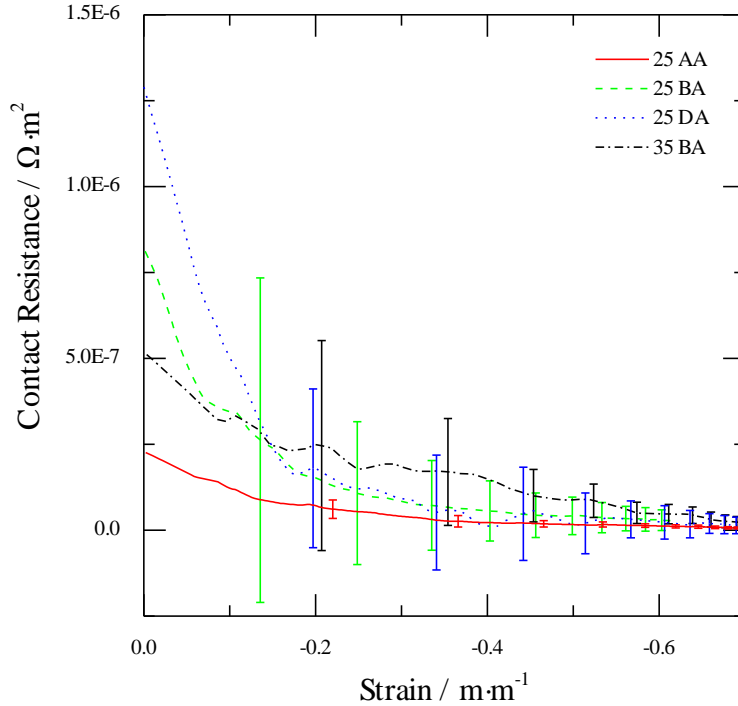


Figure 20: PTL-anvil contact resistance as a function of PTL strain calculated via TP_METHOD_1.

While mean results appear reasonable, the confidence bounds which extend into the unrealistic negative domain are worrisome. It would appear the assumption of small PTL-PTL contact resistance in a stack of samples is weak; and may be further scrutinized by examining the average percent difference observed between single- and double-stack resistances:

$$\text{Equation 25 } \Delta_{Single\&Double} = (2R_{z,single} - R_{z,double})R_{z,single}^{-1} = [(4R_{PTL-anvil} + 2R_{PTL}) - (2R_{PTL-anvil} + R_{PTL-PTL} + 2R_{PTL})]R_{z,single}^{-1} = [2R_{PTL-anvil} - R_{PTL-PTL}]R_{z,single}^{-1}$$

Equation 25 can offer an impression of the difference between PTL-anvil and PTL-PTL contact resistances; a positive number for $\Delta_{Single\&Double}$ is evidence in support of TP_METHOD_1's fundamental assumption. The result is plotted in Figure 21.

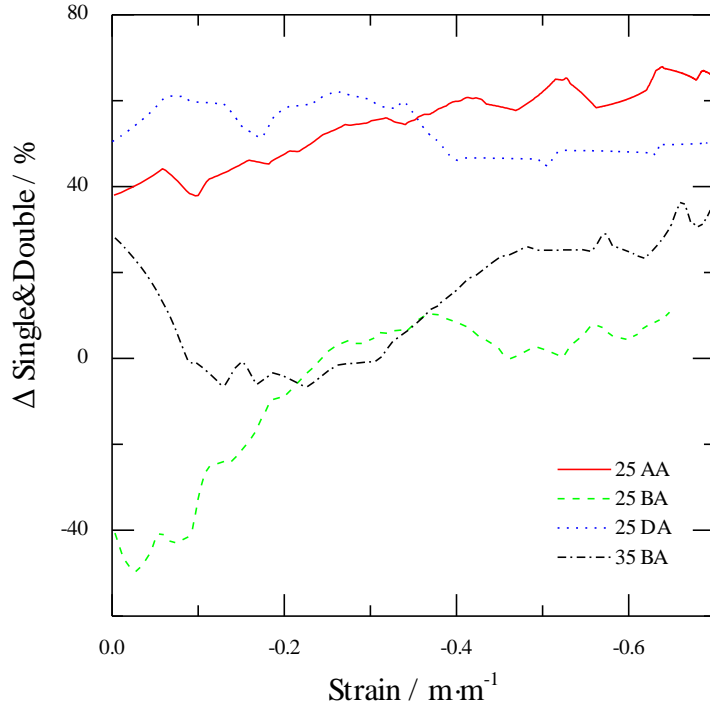


Figure 21: Relative difference between two PTL-anvil contact resistances and one PTL-PTL contact resistance as a function of PTL strain.

Strictly, the magnitudes can not be used as a measure of assumption quality, nor should comparison be made between different PTL models. Factors which may independently impact the two contact resistances include PTFE at one or both adjoining surfaces, and/or the difference in mechanical compliance between PTL and anvil surfaces. We are not convinced of TP_METHOD_1's validity; the negative values observed under some conditions suggest the assumption of negligible PTL-PTL contact resistances is erroneous (one $R_{PTL-PTL}$ must be at least half the magnitude of two $R_{PTL-anvil}$). Further, the error shall only compound when stacking samples. How this result contrasts similar thermal conductivity literature, where the assumption may be appropriate, could be the product of non-zero thermal conduction offered by the (malleable) PTFE addition.

Contrasting TP_METHOD_1, TP_METHOD_2 does not assume domination of a single contact resistance; instead PTLs of different thickness are used to manipulate t independently from n in Equation 18. However, there is a central assumption that bulk material resistivities are consistent. The result of TP_METHOD_2 for 25/35 BA is presented in Figure 22.

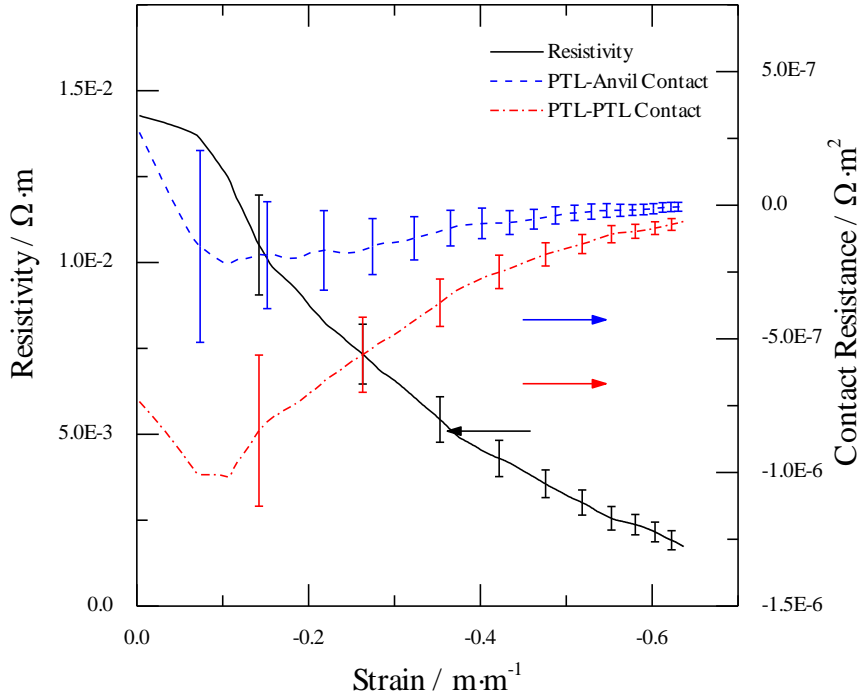


Figure 22: Principal resistivity through-plane as a function of PTL strain calculated via TP_METHOD_2. Also plotted are the PTL-PTL and PTL-anvil contact resistances. 25/35 refers to the assumption that BA model material properties are consistent across manufactured thicknesses.

Immediately questionable are the negative contact resistances for the PTL-anvil and PTL-PTL interfaces. If TP_METHOD_2 is to output a reliable measure of resistivity, all secondary outputs ought to be, at the minimum, physically reasonable. We attribute the failure of TP_METHOD_2 to the through-plane bulk resistivity of 25 and 35 BA being different (i.e. the central assumption is erroneous). This shall be further enforced by in-plane results. We suggest that this analysis pitfall may extend to other model and thickness combinations. Our results raise serious implications for analyses in the literature which make use TP_METHOD_2; it may be incorrect to assume (with the consumer level of control) that select properties of different PTL models are inherently shared. Our results are corroborated by similar studies of PTL structure and thermal conductivity [150,151].

The results of TP_METHOD_3 are plotted in Figure 23.

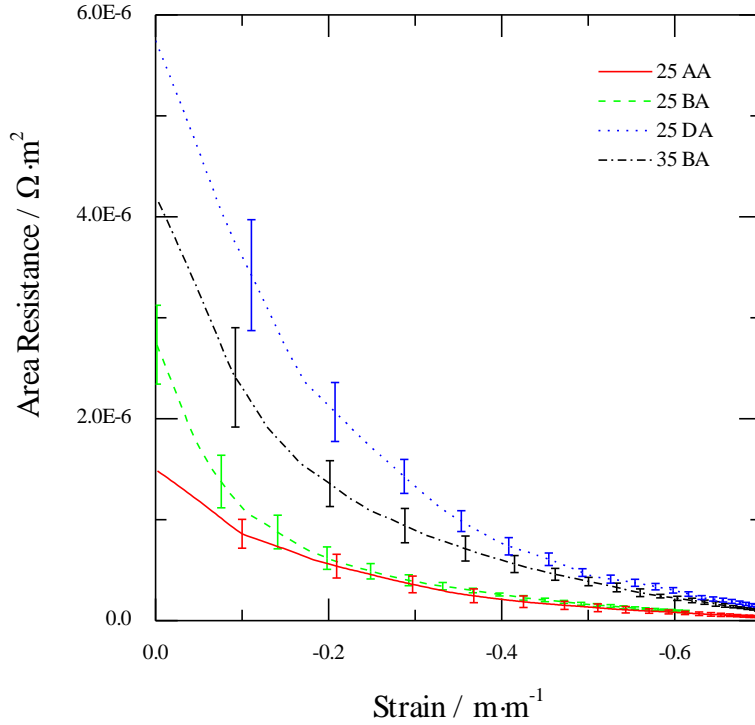


Figure 23: Total area resistance in the through-plane direction as a function of PTL strain calculated via TP_METHOD_3. Values capture contributions of the bulk sample and of two PTL-anvil contacts; without separating the contact contributions, calculating a resistivity ($\Omega\cdot\text{m}$) is misleading.

An increase of area resistance is observable with increasing PTFE contents; it is uncertain by how much this is attributable to bulk or contact resistance manipulation. While Mathias et al. concluded that there is negligible effect on the bulk resistivity with increasing PTFE [34], their study (based on TP_METHOD_2) was limited to PTLs with contents of 0 and 3.5 wt%. For PTLs with similar carbon substrates, the addition of a non-conductive filler (PTFE) to displace void space would presumably not alter bulk resistivity. However assuming through-plane current travel relies on vertically adjacent fibre-fibre interaction, it is conceivable that PTFE may become entrapped between individual fibres during manufacturing and modify the bulk resistivity. Were resistivity determinable from our through-plane measurements, insight would come from examining whether changes in bulk resistivity are attributable to improved connectivity of the carbon phase or simply from more conductive material per unit volume. Equation 26 describes bulk resistivity as the harmonic mean of resistivities of the different phases:

$$\text{Equation 26 } \rho = (\phi\rho_{air}^{-1} + (1 - \phi)\rho_{carbon}^{-1})^{-1} = \rho_{carbon}(1 - \phi)^{-1}$$

, where we have made the simplifications of treating air and PTFE as a single infinite-resistivity phase; and ρ_{carbon} represents the resistivity contribution of the carbon matrix composing the PTL, not to be confused with resistivity of a single fibre or of solid carbon. Invoking the definition of porosity and mechanical strain, and assuming neither the planar sample area nor the volume occupied by carbon changes as the bulk is compressed, Equation 26 may be rewritten as:

Equation 27 $\rho = \rho_{carbon}(\epsilon + 1)(1 - \phi_0)^{-1}$

, where bulk resistivity is shown to be a linear function of strain. With experimentally determined resistivity, ρ_{carbon} may be plotted to judge whether it decreases with compression (i.e. improving fibre-fibre connectivity as observed in [152]) or remains a constant.

We propose that TP_METHOD_3 can be a robust comparative tool, given it lacks difficult-to-manufacture apparatus (e.g. micro-electrodes) or flawed assumptions in data analysis. With establishment of comparison standards, PTLs might be monitored in a manufacturing quality assurance context and/or experimental PTL concepts might be screened versus established products. However a stipulation on TP_METHOD_3 is measuring a determinate number of discrete samples between anvils (ideally a single). Averages of flexible stack counts, perhaps imposed by instruments of too low resolution, would include indeterminate inter-sample contact resistances.

4.4.2 In-plane

In-plane resistivities ($\rho_{x'x'}$ and $\rho_{y'y'}$) of the investigated PTLs are presented in Figure 24. Consistent with the literature, in-plane resistivities are approximately an order of magnitude less than the through-plane resistivities if TP_METHOD_1 through-plane results are taken as approximate.

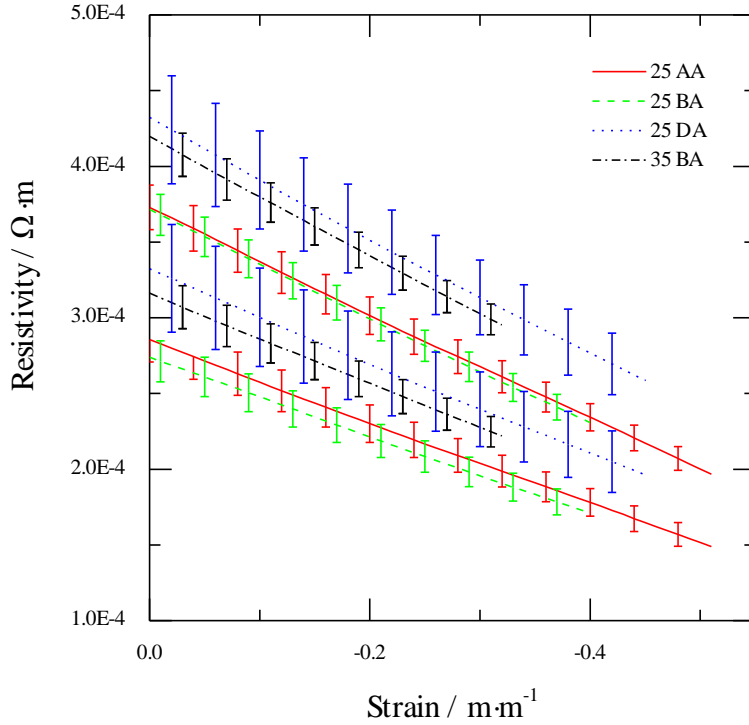


Figure 24: Principal resistivities in-plane as a function of PTL strain. For a given material, the upper curve corresponds to FXD and the lower curve to FAD.

With application of compressive strain, in-plane bulk resistivities decrease nearly linearly. In-plane resistivities are anisotropic; as hypothesized from preferential fibre alignments. By virtue of anisotropy existing, we stress that capturing a correct measurement of in-plane resistivity requires either: more than two measurements, or two measurements with known alignment to a-priori known principal directions. Two unaligned, orthogonal, measurements would incorrectly estimate the resistivity in other directions. This argument is presented graphically in Figure 25. Additionally, assuming a set of principal directions based on a cut sheet edge is unreliable, unless the relation to manufacturing (machine) direction is preserved; which still does not address the possibility of manufacturing direction versus deposited fibre direction inconsistency.

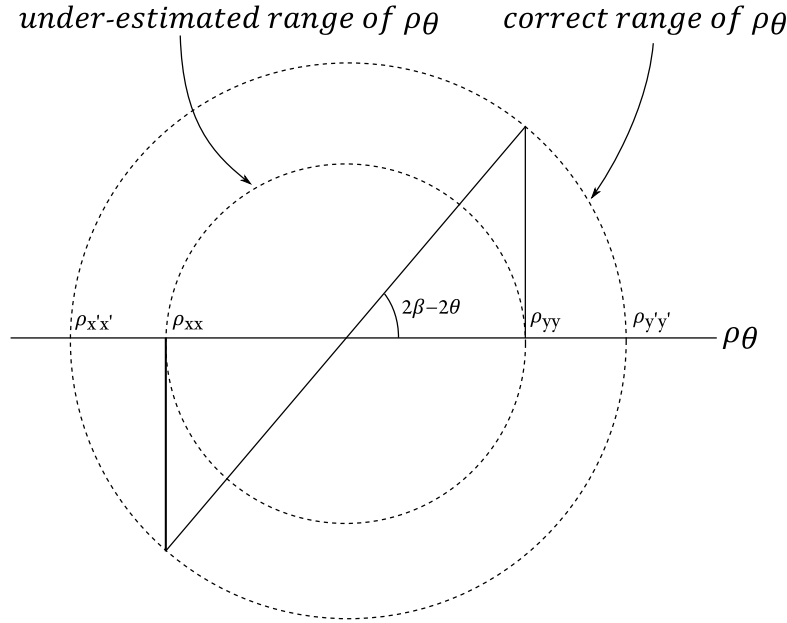


Figure 25: Diagram representing in-plane resistivity as a function of direction. The principal components define the interval of possible values. If two orthogonal measurements are incorrectly assumed to coincide with principal directions, the interval width is under-estimated. However if the alignment of said orthogonal measurements to the principal direction is known, the true interval may be reconstructed.

Further addressing in-plane resistivities; we do not observe a correlation between resistivities and PTFE contents for similar substrate PTLs. However the resistivities, over both principal directions and different materials, fall within approximately $1.5 \times 10^{-4} \Omega \cdot m$ of each other and share a similar rate-of-change with strain. This might support, but not confirm, hypotheses that PTFE content does not alter bulk resistivity, and/or that the trends observed through-plane are PTL-anvil contact resistance dominated. These hypotheses are tempered by recognizing the nature of in-plane current paths is distinct from that through-plane in a two-dimensional oriented fibre structure. Continuing, 35 BA demonstrates a definitively higher resistivity than 25 BA in-plane, suggesting these materials do not share common bulk properties. This observation reinforces the critique leveled at TP_METHOD_2.

We attribute the widths of resistivity confidence bounds to the intrinsic resistivity variation over a PTL sheet; from which multiple samples must be taken to determine principal components. Morris and Gostick [132] mitigated the issue by devising an apparatus which measured an original square sample, followed by a (smaller square) cut-out out of said original sample set at 45° . While their method provides resistivities in four directions for a consistent

piece of material, it cannot be applied with a compressive load profile. Plastic deformation of the PTL prevents sweeping over the compression range before extracting the 45° cut-out; while acquiring the four resistivities together at each progressive load would quickly shrink the sample with repeated cut-out steps. Ultimately, multiple samples are required for capture of PTL in-plane principal resistivities as a function of compression using Montgomery analysis.

4.5 Summary

A method for acquiring three-dimensional electronic resistance information of PEM fuel cell PTLs has been reported; and data has been produced for four commercial materials. Unique was the in-plane anisotropic resistivity being resolved via square 4PP arrangement over a through-plane mechanical load profile. This observed anisotropy forced the reconsideration of MD and CD oriented data in the literature and the desirability of resolving true principal property components and directions. The acquisition of load and thickness information permitted resolution of complementary through-plane stress-strain behaviour. Three approaches from the literature for handling through-plane resistance data were presented. Those approaches neglecting certain contact resistances and/or combining superficially similar but different thickness materials were demonstrated to yield unrealistic results. The inability to resolve through-plane bulk material properties from contact resistances (which may produce ohmic losses of similar magnitude) continues to limit generalization of fuel cell data. Without a consistent description of component bulk properties, contemporary focused studies (e.g. examining contact resistance effects between PTLs and BPPs of difference design, material and textures) shall remain highly specific to the experimental configuration. We close by reflecting that no industry standards are yet established for the control of fuel cell transport layer electronic resistivity. As PEM fuel cell technology moves forwards from early commercialization, materials specifiable and verifiable in a consistent language are compulsory for an effective supply network.

5 Electronic resistance of PEM fuel cell transport layers versus cyclic compression

The present chapter expands the work of Chapter 4 , published as [1] to include the effects of cyclic mechanical loading upon the anisotropic electronic resistance of PEM fuel cell transport layers. This chapter is additionally distinguished by demonstrating the applicability of the electronic resistance measurements as a quality control monitor.

We report on the three-dimensional electronic resistance of PEM fuel cell PTLs as a function of cyclic mechanical compression. Through-plane data are reported as total area resistance (i.e. inclusive of contact resistance contributions), whereas in-plane data are reported as resistivity measurements with resolved anisotropy. In-plane resistivities are acquired via a square 4PP arrangement, which unlike linear 4PP arrangements can resolve the anisotropy. Results are presented for SGL SIGRACET 25 BA. Both through-plane and in-plane data exhibit unique profiles for the initial compressive loading. These are followed by consistent trajectories for subsequent loading cycles, which is in correspondence to material plastic deformation. Plastic deformation damage to PTLs may occur during cell manufacture; to the possible detriment of deployed stack performance. We outline means by which our method can be adapted for on-line monitoring of PTLs as part of a manufacturing quality assurance programme.

5.1 Introduction

Ohmic resistance is detrimental to fuel cell output performance. Minimizing ohmic losses throughout the cell is necessary to realize the benefits of optimized catalyst design and higher power densities. While the resistance of the ionomer is well documented and is significant to overall cell resistance, resistance of the PTLs is less understood. Although contemporary PTL

optimization efforts are focused on the mass-transport (e.g. capillarity), as membranes improve, the electronic properties of PTLs shall feature more prominently in design decisions.

Paper PTL material is used in many contemporary PEM fuel cells; because carbon fibres make up this type PTL, preferential fibre directions may exist which result in anisotropic material resistance. Furthermore, these materials are sensitive to plastic deformation under mechanical compression. Such compression may be imposed statically or cyclically during the component's lifecycle. Events in manufacturing may be intentional during calendaring processes, but also unintentional during MEA subcomponent assembly or roll-to-roll material handling. During stack assembly, excursions might occur during stack compression and fastening. After PEM fuel cell module deployment, thermal or humidity transients may impart stresses beyond the limits of fastening hardware compliancy.

There is an urgent demand from fuel cell assembler and subcomponent manufacturers for material standards and characterization tools. Appropriate controls are needed to detect and prevent failures; in manufacturing and in interpretation of end-of-life data. Understanding the effect that cyclic loading may have on the PTL is requisite for a quality assurance programme.

We report on new methods and apparatus to determine the three-dimensional anisotropic electronic resistance as a function of cyclic mechanical load. Example data are presented for commercial PTL material representing the contemporary standard. Both through-plane and in-plane directions are examined, where full PTL anisotropy is determined by resolving the principal resistivities within in-plane. Anisotropic treatment of resistance is forced by the fibre-based structure of contemporary PTLs; where fibre alignment distributions determine connectivity in different directions (e.g.: through-plane, in-plane along fibres, and in-plane across fibres). The examination of resistances as functions of cyclic compression in the through-plane direction addresses the role of material plastic deformation and underscores the need to consider material history – from layer manufacture to deployed stack. We report hypotheses for the mechanisms altering resistance with mechanical compression. We propose and demonstrate electronic resistance methods to evaluate the quality and history of PEM fuel cell materials. Finally, we suggest that such facile tests may be formulated into otherwise unavailable industrial standards.

5.2 Background

We have previously reviewed the literature addressing ex-situ electronic resistance characterization of PEM fuel cell transport layers in Chapter 4 . There are few studies which consider the cyclic loading effects in general for the transport layers. Escribano et al. presented

mechanical data, stress and thickness, for only two compression cycles [61]; plastic deformation was observed in the materials studied. Mathias et al. produced a study also limited to mechanical data [34]. In these efforts, the residual strains in PTLs cycled between approximately 0 and 2.5 MPa increased from 0 to 25% over ten cycles; most of the change occurred within the first loading. Sadeghi et al. examined thermal conductivity as a function of cyclic loading [153]. After the fifth cycle, no further hysteresis was observed from their Toray PTL material. Kleemann et al. acquired a single mechanical load-unload cycle with electronic resistance [140]; but the data was processed for modelling contact resistance and not actually reported. Kim et al. reported qualitative electronic properties, but in the context of thermal cycling [154]; they speculated that thermal cycling produced plastic deformations of the PTL via ice formation and thermal expansion.

Chapter 4, published as [1], examined PEM fuel cell PTL electronic properties as functions of static mechanical compression. Through-plane resistivity analysis techniques from the literature were methodically evaluated, and a novel method was developed for in-plane resistivity measurement. The present chapter is distinguished from the literature by addressing the electrical characteristics as a function of cyclic compression, and by extending the applicability of our methods to material diagnostics. Our objectives and those of the aforementioned studies are summarized in Table 5.

Table 5: Summary of relevant experimental studies into PTL transport resistance.

Authors	Cyclic load?	Transport property	Anisotropy addressed?
Todd et al. [1]	N	Electronic	Y
Escribano et al. [61]	Y	Nil	N
Mathias et al. [34]	Y	Nil	N
Sadeghi et al. [153]	Y	Thermal 0.8-2.2 KW ⁻¹	N
Kleemann et al. [140]	1	Electronic, not reported	w/o cycling
Kim et al. [154]	Thermal	Electronic (MEA) 0.1-2.5 $\Omega \cdot \text{cm}^2$	N
Todd et al. (this study)	Y	Electronic	Y

The present study targets intrinsic material behaviour. Modelling studies seeking to apply our results must consider the interaction of their specific bipolar plate configuration; results from an appropriate mechanical model may determine at what strain conditions to sample our data, be it resolved as an inhomogeneous property or approximated as an average.

5.3 Method

Figure 13 illustrates the coordinate system describing the three-dimensional directional material properties of a PTL. It captures the important directions where: x and y are in-plane and aligned to a cut sample; z is perpendicular to the plane (through-plane); and MD, CD, FAD and FXD directions are defined as illustrated. We define MD and CD based on the edges of supplied material; this may not coincide with the true MD and CD, as oversight over manufacturing extending to initial layer formation is unavailable. Regardless, FAD and FXD do not necessarily correspond to MD and CD (ours or the true) [1,132,133]. Because of the MD-FAD misalignment, when measuring the in-plane components of PTL resistivity, the principal directions must be determined from measurements in more than two non-parallel directions or known a-priori.

SGL SIGRACET 25 BA is evaluated in the present study. This is a commercial fibre-based PTL featuring: 190 μm nominal thickness, 5 wt% PTFE hydrophobic treatment, and no microporous layer. All samples are extracted from the same sheet of material. In-plane samples

are cut in alignment with respect to principal directions of in-plane resistivity, following the procedure described in Chapter 4 . Measurements are conducted at room temperature and ambient humidity. Humidity is not expected to produce a difference in the (real) resistance; whereas the temperature difference from room to typical cell operation may change the average resistance, but likely not the cyclic load related behaviour. Regardless, the focus of the present study is to investigate a quality control monitor; which need not be acquired at cell temperatures.

The fundamental measurement apparatus and methods are reported in Chapter 4 ; these have been improved upon for the present chapter and are described in the following paragraphs.

Through-plane measurement is acquired using a linear four-point probe (4PP) electrode arrangement affixed to planar anvils which engage and compress the PTL sample. An Agilent 34420A micro-ohm meter measures the resistance. The resolution afforded by our system negates the need for measuring stacks of discrete PTL samples; which introduce indeterminate inter-sample contact resistances, and do not confer any capability to resolve resistivity. Through-plane data are reported as total area resistances (i.e. inclusive of two PTL-anvil contact resistance contributions); separation of bulk and contact resistance effects is not satisfactorily achievable with contemporary non-micro-electrode methods in the literature, as established in Chapter 4 . Cyclic compression for through-plane measurement is achieved via an electronically regulated pneumatic cylinder in a control loop with a load cell. Fresh (un-tested) samples are stressed step-wise, allowing time to equilibrate at each step. Initially from 0.0 to 2.0 MPa, and then cycled between 2.0 to 0.5 MPa ten times. Equilibration at each load step is required to avoid obfuscation of results by the time-dependence of PTL mechanical behaviour (e.g. creep). The duration allotted is established from the time required before any measurand fluctuation fell below instrument resolution. The procedure is fully replicated three times (one sample for each replication).

In-plane measurement is acquired using a square 4PP electrode arrangement in conjunction with non-conductive anvils which engage and compress the PTL sample. An Agilent 34420A micro-ohm meter measures the resistance. The square 4PP electrode arrangement is different from an in-plane linear 4PP configuration, because the square arrangement permits multiplexed x and y measurement by simple switching of current and voltage connections (e.g. it is unnecessary to prepare and measure separate PTL samples for each measurement direction). Furthermore, the method of Smits for interpretation of linear 4PP data are strictly only applicable for isotropic media; whereas the Montgomery method adapted for square 4PP measurements is applicable for isotropic or anisotropic media [66,146]. All samples are cut in

alignment to FAD and FXD, in-plane data are reported as principal components of bulk resistivity. Compression in the in-plane apparatus is via thickness control; strains are cycled between -0.05 and $-0.4 \text{ m}\cdot\text{m}^{-1}$ three times. The non-zero origin facilitates consistent anvil contact and alignment with samples. As with the through-plane procedure, time for equilibration occurs at each step; five minutes was chosen as no measurand changes were observable beyond this period. Although it was desirable to match through-plane data by controlling in-plane measurement stress, this is not achievable with our current apparatus. We therefore select an in-plane measurement peak strain (largest negative strain) consistent with the strain observed in through-plane measurement at peak stress (largest negative stress). The procedure is fully replicated three times (one sample for each replication).

Finally, a complementary in-plane measurement investigates the influence of peak strain. Here, a sample is cycled between $-0.05 \text{ m}\cdot\text{m}^{-1}$ and four evenly distributed progressively greater peak strains up to $-0.4 \text{ m}\cdot\text{m}^{-1}$. This procedure is undertaken only once.

5.4 Results and discussion

Stress-strain results derived from through-plane measurement are presented in Figure 26. We elected to present results as triplet subplots to avoid unclear superimposed profiles.

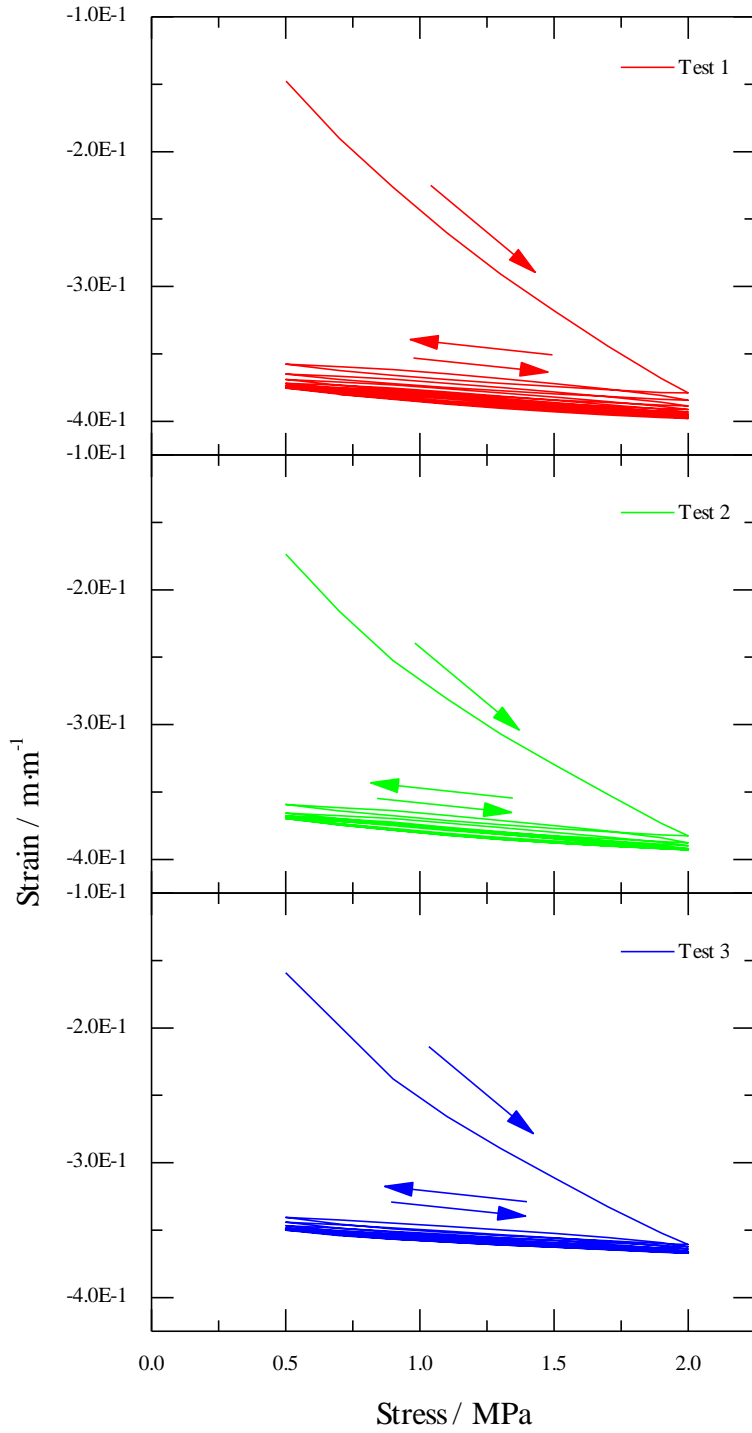


Figure 26: Compressive strain ϵ as function of applied stress.

We observe the majority of plastic deformation occurring as a result of the first compression process; subsequent compressions increase the plastic deformations, tending to a maximum near $-0.4 \text{ m}\cdot\text{m}^{-1}$. During these subsequent cycles, the strain only changes a few percent. Progressive compressions also increase the peak strain along a similar profile extrapolated from the first compression. Finally, the first compression process stress-strain profile is significantly different from all others, suggesting an increase in material stiffness. The aforementioned observations are consistent for all measurements; though their data do not directly lie upon each other. This discrepancy is attributed to the intrinsic variability in the PTL material. We suggest the PTL may be treated as possessing predominantly plastic material behaviour; which may be attributable to fibre and binder breakage, and/or migration of hydrophobic agent. This plastic behaviour is examined in following discussion.

Through-plane area resistance versus strain is presented in Figure 27.

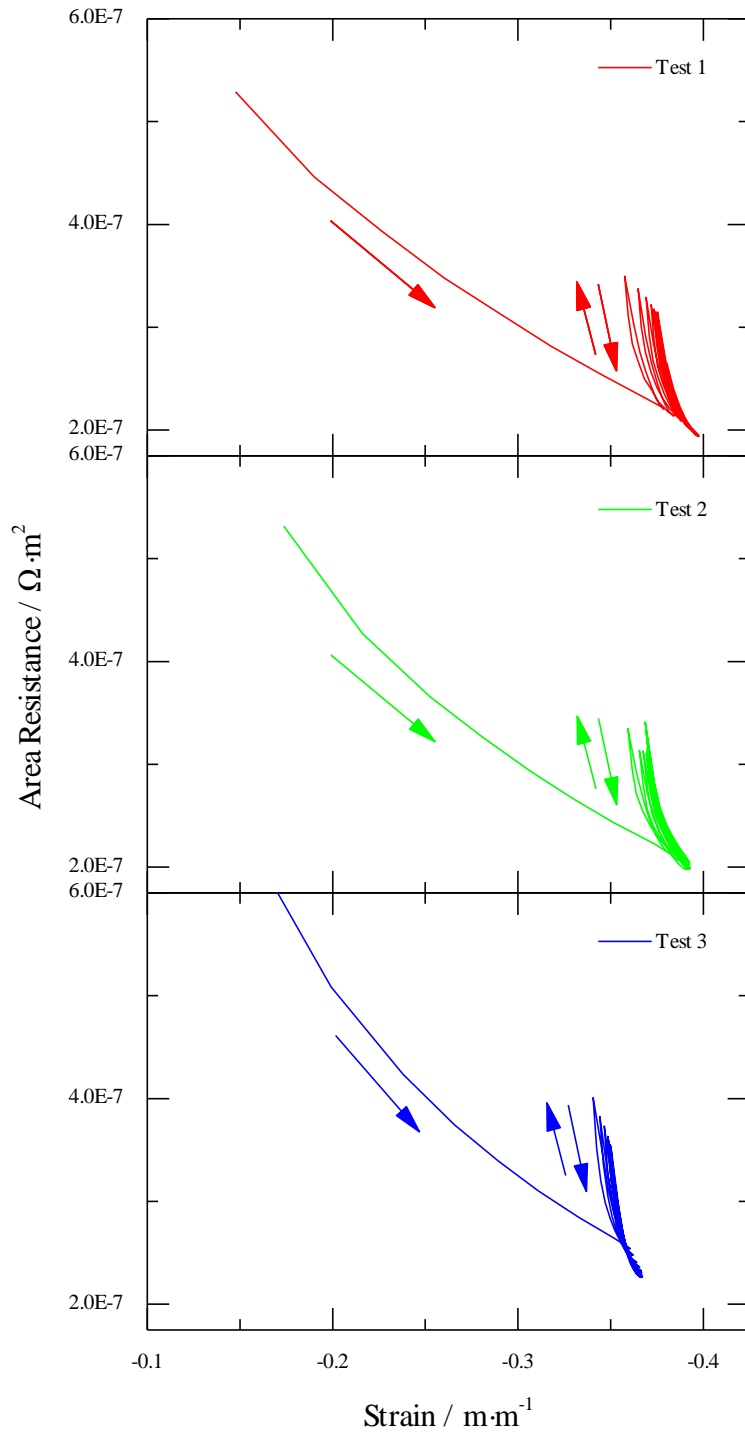


Figure 27: Total area resistance in the through-plane direction as a function of strain.

Observations are similar to those for stress-strain information. The first compression process follows a profile distinct from subsequent compression/decompression processes. Further, area resistance minima at successive peak compressions follow a common line extrapolated from the first compression profile. Although plastic set strains increase after each cycle, maximum resistances after decompression do not show a definitive behaviour. Loading profiles (after the first) do not follow the unloading profile of the preceding cycle; whereby the newest compression process effects a sharper decrease in resistance with strain. Further inferences on the phenomena effecting observed resistance are prevented by not having rigorous distinction between bulk material and contact resistance contributions.

In-plane principal resistivities are plotted versus strain in Figure 28.

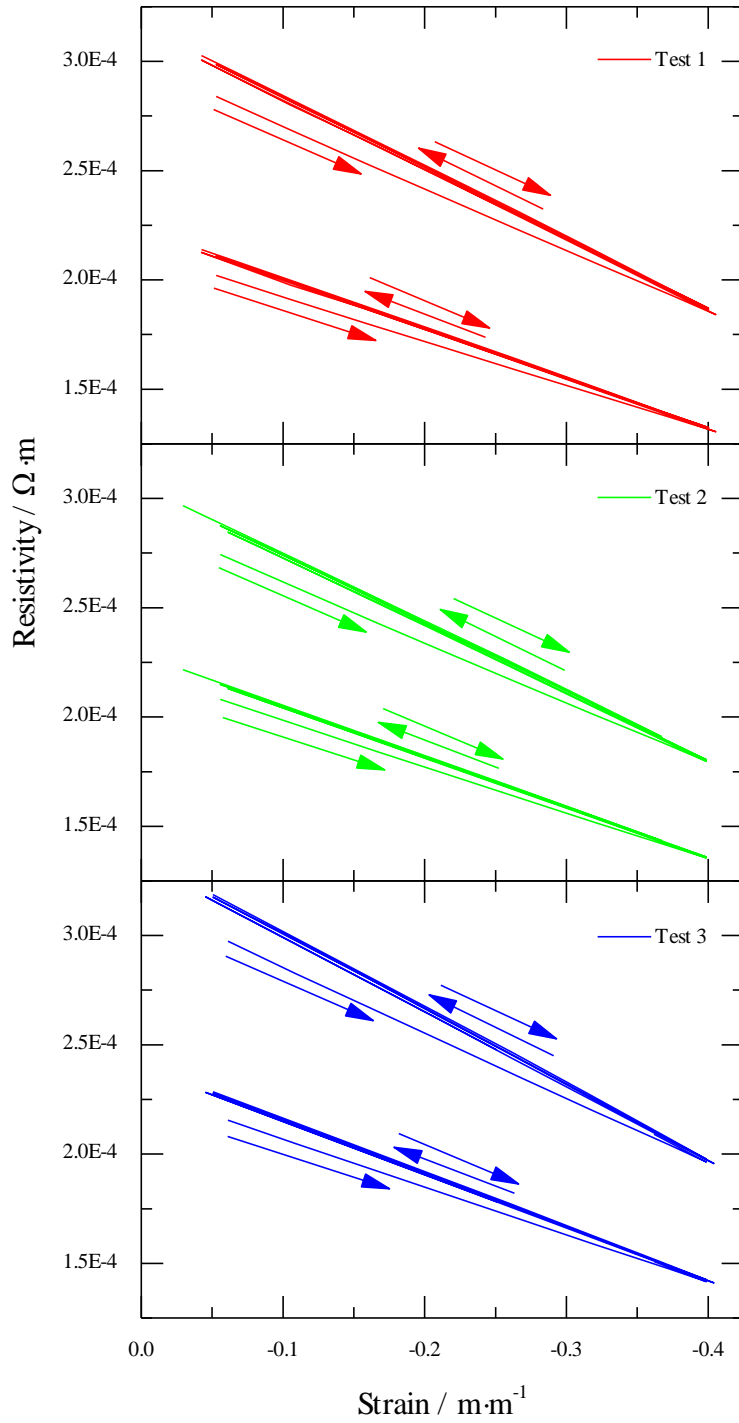


Figure 28: Principal in-plane resistivities as functions of strain. The upper curve corresponds to FXD and the lower curve to FAD.

These are distinguished from through-plane results in being isolated to the PTL material itself, i.e. not including contact resistances. In both in-plane directions, we observe a distinct initial compression profile; whereas subsequent compression/decompression cycles are indistinguishable from each other. In other words, achieving the peak strain permanently altered the rate-of-change of resistivity versus strain. Normalized resistivities are plotted in Figure 29 for comparison of orthogonal components.

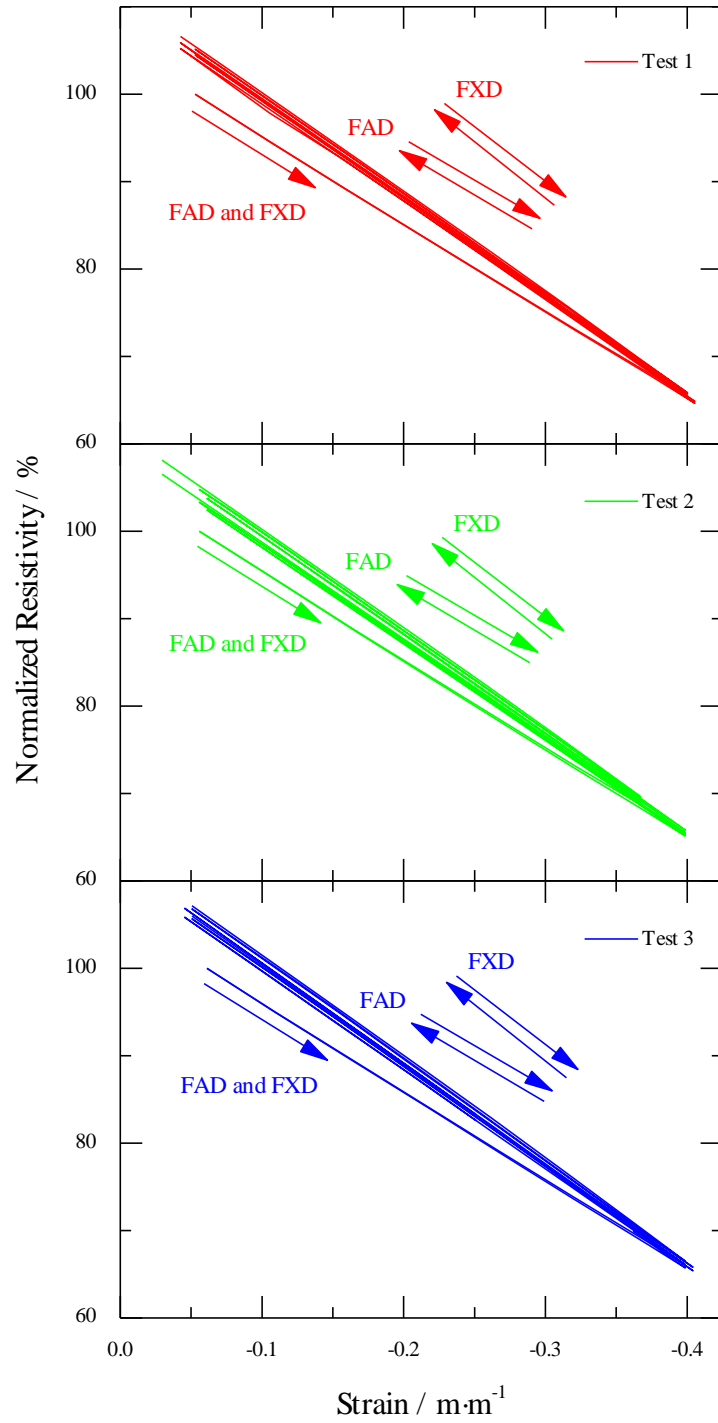


Figure 29: Principal in-plane resistivities, normalized by initial values, as functions of strains.

FXD and FAD data are admittedly difficult to distinguish in the illustration. The profiles are consistent over the first compression, but upon subsequent decompression follow different trajectories for the remaining cycles; where the FXD component of resistivity increases more as a result of the procedure. Assuming conduction occurs on average more along fibres in FAD versus FXD, the greater sensitivity to mechanical compression in the FXD direction suggests damage may preferentially occur at the fibre(-binder)-fibre interfaces versus fibre breakage. Following the first compression, the material's resistivity is increased; this contrasts the decrease observed in the through-plane direction. While in-plane and through-plane data are not strictly comparable due to contact resistance effects and loading scenario; we hypothesize that the damage from through-plane compression negatively affects in-plane conduction along and between horizontally adjacent fibres, whereas through-plane conduction is positively affected via better vertically adjacent fibre-fibre connectivity and/or fibre-anvil conformation.

Freeze-fractured cross-section SEM images of samples, before testing and after three cycles in the in-plane apparatus, were produced. These are illustrated in Figure 30.

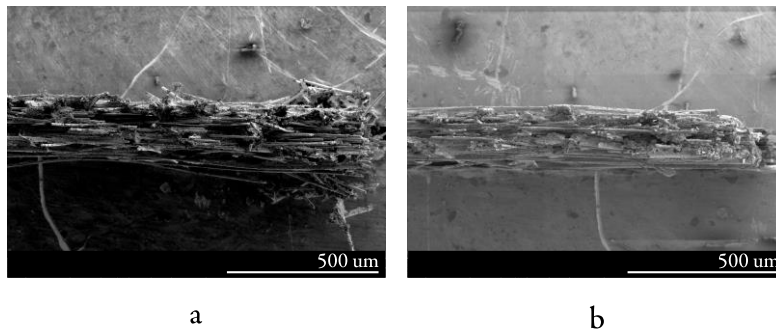


Figure 30: SEM images of PTLs before (a) and after three strain cycles (b) (using the in-plane apparatus).

The procedure for freeze-fracturing comprised immersion in liquid nitrogen, followed quickly by snapping the embrittled material between forceps. A change in sample thickness is apparent; but it is not possible, in examining the series of micrographs encompassing the fractured edges, to discern obvious fibre or binder damage. We are confident from our resistance and mechanical data that damage to the fibre network occurs; however a two-dimensional SEM imaging approach is insufficient to describe this damage.

PTL plastic deformation can change the electronic and mass-transport properties, which may impact fuel cell performance. As described earlier, this may manifest in as-supplied (damaged) PTL material or be introduced during manufacturing. Sheet resistance is an intermediate

calculation of the in-plane resistivity analysis; for a quality assurance application, it would not require simultaneous thickness measurement. Sheet resistance is the bulk resistivity scaled by layer thickness:

Equation 28 $R_s = \rho \cdot t^{-1}$

Figure 31 presents the anisotropic components of sheet resistance as a function of cyclic strain with progressively increasing peak strains.

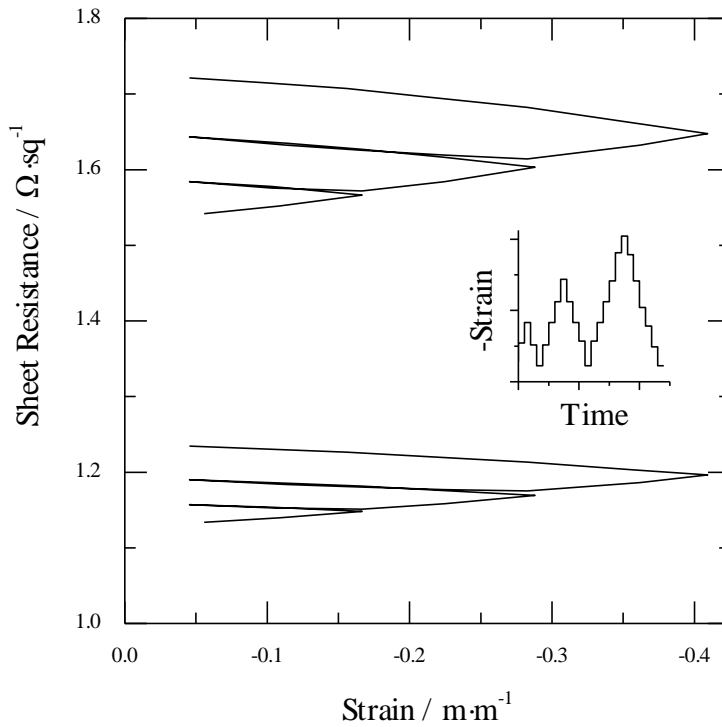


Figure 31: Sheet resistances as functions of strain. Illustrated by the inset, the material is cycled in strain with progressively greater peak (in magnitude) strains each cycle.

We observe that the permanent increase in at-rest sheet resistance is can be correlated to the peak compressive strain experienced by the transport layer. In our experiment this increase may be similar in magnitude to sample variability, however, our system is a small measurement area apparatus configured for experimental materials development. On-line measurement in a manufacturing environment would make use of automotive-size cell active areas; a larger analysis area would homogenize local material variability. We suggest sheet resistance may serve as an indicator for estimating transport layer health because it can quickly estimate the

past compression of the material. Our method is particularly applicable for manufacturing processes as an on-line quality monitoring tool; this is depicted in Figure 32.

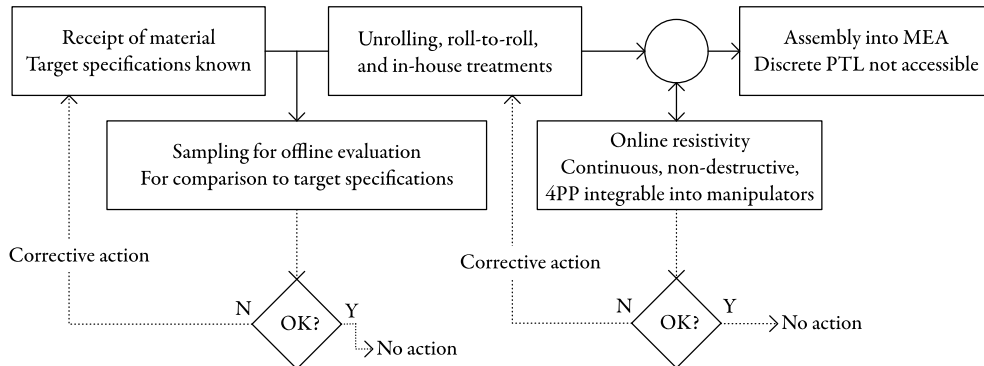


Figure 32: Process diagram depicting where a sheet resistance measurement may integrate.

Continuous, non-destructive, screening may be achieved through integration of the 4PP arrangement into PTL manipulating hardware. Further, the analysis is extensible to arbitrary sample size and (rectangular) aspect ratios; baseline data for a PTL material may easily apply across different cell designs.

An error analysis (e.g. error bars) is not readily possible for the data presented in this chapter. A general estimate of the measurement-to-measurement uncertainty (i.e. sample and system error) could be taken from the complementary figures of chapter 4 . That error would be greater than the cycle-to-cycle evolution in resistance (which exists and is consistent in behaviour across our tests); this may lead to misinterpretation of the cyclic load effects being measurement artefacts. An appropriate solution would separate the variability in sample average resistivity (e.g. the vertical shifts between subplots of figures Figure 26 through Figure 28) from the variability in resistivity response versus (cyclic) load *change*. This could be expressed mathematically for the in-plane measurements as:

Equation 29 $\rho = f(\epsilon, n_{cycle})$

Where the variation of interest is in $\left. \frac{\partial \rho}{\partial \epsilon} \right|_{n_{cycle}}$. Establishing a general function for Equation 29 is the challenge for future work.

5.5 Summary

We have reported a method for acquiring three-dimensional electronic resistance information of PEM fuel cell PTLs under cyclically applied through-plane compression. Acquisition of in-plane resistivity as a function of cyclic load was unique. Our in-plane square 4PP apparatus and Montgomery analysis is an improvement over the state-of-the-art methods. We offer rigorous resolution of anisotropy and principal components within in-plane. These data were complemented by capture of through-plane stress-strain and area resistance information. We quantified plastic deformation of PTLs and related these solid mechanics data to electrical properties. The greatest changes in resistances were observed after the first compression event; where continuity through-plane improved and in-plane diminished. The permanent set in mechanical and electrical behaviour affirms that fibre network connectivity is susceptible to damage at our loads. Samples were visualized via SEM in cross-section before and after testing, but the damage was not obvious. More powerful tomographic visualization might provide clarification at the expense of complicated, likely destructive, testing. However such techniques are not as adaptable for on-line quality monitoring versus our resistance approach. We also remark that a quality control electrical measurement is more facile than a fluid flow measurement; which would need careful manifoldng to capture anisotropy and avoid any small leaks (which can be disastrous to measurement of PTL air permeability). An electrical measurement could supplement an areal weight measurement with information about layer damage (versus only gravimetric information). Moreover, we demonstrate the preliminary feasibility of an in-plane sheet resistance measurement to estimate the peak compressive strain experienced by a PTL. Further study shall be required to elucidate the effects of test environment and harmonize the through-plane mechanical compression with other loading scenarios. Additional study may investigate creation of a mathematical representation for the strain-cycle evolution of resistance to facilitate error analysis. We conclude by suggesting that further study of transport layer behaviour is required to develop the PEM fuel cell structure-property-performance relationship; which is necessary for rational cell design and industry standards establishment.

6 PEM fuel cell transport layers enabled via electrospun carbon nonwovens

We report on the synthesis and performance of carbon nanofibre substrates for PEM fuel cell transport layer applications. Electrospinning is used for fabrication; by manipulation of spinning properties, morphological control is demonstrated in the product. Our application of the technology and its manipulability to PEM fuel cell transport layers constitutes a novel approach to the manufacture of such layers. Ex-situ morphology, electronic resistance and water contact angles are reported in addition to in-situ hydrogen/air fuel cell performance. Electrospun transport layers are compared directly to established commercial products in a cathode PTL role. The electrospun transport layers demonstrate approximately 85% of the commercial limiting current density, swifter water transport characteristics, and markedly more stable operating points.

6.1 Introduction

PEM fuel cells are viable energy conversion devices for a growing number of applications – from transportation electrification to portable devices, to stationary energy storage and recovery. The PTLs, interposed between CLs and bipolar plates, are a critical component of the PEM fuel cell.

Our group is studying the novel application of electrospinning technology for the synthesis of PEM fuel cell transport layers (both PTL substrates and/or MPLs); with the specific objective of leveraging the technology's unique capacities to engineer the morphology of the layers. A general background for PEM fuel cell transport layers is given in Chapters 1 and 2. In contrast to CLs, the development of new PTL structures has received little attention, and the research of transport layers appears focused on the characterization of established materials. Our

research is focused on alleviating the deficiencies and improving the performance of conventional PTL materials, while providing greater system optimization opportunity. General background for electrospinning is given in Chapter 1 ; reviews are available in the literature [15,24]. Applied towards PEM fuel cells, electrospinning has been the basis of materials for novel CLs [155–159], and membranes [160–162]. Further review is offered by Cavaliere et al. [128] and Dong et al. [17] whom address energy applications of electrospinning in general.

Unlike the current state-of-the-art, the electrospun transport layers can be designed with properties (e.g.: porosity, hydrophobicity, or conductivities) which vary continuously or in a prescribed manner in three-dimensions; contemporary literature attempting such manipulation in PEM fuel cell PTLs, none of which incorporate electrospinning, have featured composite or gradient MPLs [109–112] and collages of commercial PTLs [127]. Moreover, electrospun layers may incorporate MPL and PTL functionality in a monolithic, hierarchical, structure whilst avoiding discontinuities and irreproducible interactions at interfaces (e.g.: due to rolling, transfer, or pressing manufacturing processes). Electrospinning might also facilitate periodic or global property variation to match bipolar plate topologies, facilitating energy and mass transport between lands-channels or mediating active area operational gradients. The challenge facing electrospun transport layers is the complexity of the electrospinning process. Though the process can be described in simple terms, predicting and/or controlling the electrospun layer structure and composition can be challenging because the final product is sensitive to numerous parameters.

Our survey of the literature reveals two examples of electrospun transport layers applied to PEM fuel cells. The first is from Duan et al. [129], who manufactured an MPL on a commercial substrate and compared its performance against a self-made conventional MPL. The second is from Hung et al. [130], who implemented an externally sourced electrospun mat in a study comprising several differently manufactured PTLs; no information was offered upon the electrospinning process parameters. Critically, these two studies did not report morphological permutations of the electrospun layer, nor was there recognition of PTL optimization avenues presented by the technology.

We report on the morphology, electronic resistance, interfacial water contact angle, and in-situ PEM fuel cell performance of nonwoven carbon fibre transport layers produced by electrospinning. These layers are produced with different average fibre diameters via manipulation of electrospinning dope composition. We believe our effort is the first published instance where electrospun materials with controlled morphology are applied in a PEM fuel cell transport layer role.

The PTL contribution to PEM fuel cell resistance $|i|R$ loss is often overlooked as the membrane is the dominant impediment to charge transport in a PEM fuel cell. However, this dominance decreases as optimum humidity conditions are achieved and the resistance contribution of the PTL may remain significant to cell performance [34]. For our experimental materials, heat-treatment temperatures are low compared to those used for conventional PTLs (approximately $\sim 2000^\circ\text{C}$ for graphitization) [34,74]. This may yield less graphitization and higher resistivities, thus there is a need to evaluate this property.

Ex-situ resistance notwithstanding, electrospun transport layers may confer advantageous in-situ performance, particularly in the mass-transport domain. We report the in-situ performance from a H_2/air PEM research cell. Results are directly compared to MEAs comprising commercial PTLs.

6.2 Method

6.2.1 Materials

PAN was obtained from Scientific Polymer Products and DMF from Fisher Scientific. These materials were used without further preparation.

6.2.2 Sample preparation

PAN was dissolved into DMF to produce solutions of specific polymer percent weights. The solutions were stirred at approximately 50°C to ensure a homogeneous mixture, and then allowed to cool to room temperature. Electrospinning was performed using apparatus from Kato tech Co.. The system was configured with a voltage bias of 12 kV, a 16 cm tip-to-target distance, 18g capillary tip, and a foil covered drum target moving at $1\text{ cm}\cdot\text{s}^{-1}$ surface speed. The capillary tip was traversed over 14.0 cm at $2.00\text{ cm}\cdot\text{min}^{-1}$. Dope delivery rate averaged $0.033\text{ mL}\cdot\text{min}^{-1}$. Raw spun material was detached from their foil and sandwiched between alumina plates for heat-treatment in a tube furnace. Stabilization was achieved at 240°C with a $1^\circ\text{C}\cdot\text{min}^{-1}$ ramp rate, sustained for 2 hours under an air atmosphere. Carbonization was achieved at 900°C with a $5^\circ\text{C}\cdot\text{min}^{-1}$ ramp rate, sustained for 1 hour under an Ar atmosphere.

6.2.3 SEM and contact angle analysis

Fibre diameters of the electrospun material were determined both before and after heat-treatment. Images were acquired from a Hitachi S3000N SEM, and dimensions analysed using ImageJ software. Example micrographs are offered in Figure 33. Water contact angles were acquired via sessile drop experiment. These angles may be used to quantify the PTL

hydrophilicity or hydrophobicity, but their applicability is limited to the interaction of macroscopic water droplets with the PTL surface.

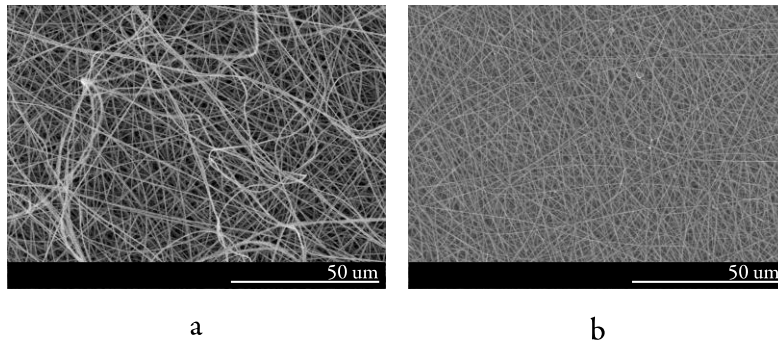


Figure 33: Typical SEM micrographs of electrospun layers (a) pre-heat-treatment and (b) post-heat-treatment.

6.2.4 Electronic resistance and mechanical characterization

Through-plane electronic resistance was acquired with the apparatus detailed in Chapter 4 . Area resistances were obtained with singular samples between anvils, and include the contact contributions of two sample-anvil interfaces. Samples are compressed step-wise in load with pauses to equilibrate at each step.

6.2.5 In-situ characterization

A 2.25 cm² active area H₂/air PEM fuel cell coupled to a Greenlight Innovation G20 test station was used to collect in-situ performance data. MEAs incorporated Gore PRIMEA CCMs and SGL 25 BC anode PTLs; the cathode PTLs were either our electrospun layers or SGL 25 AA. The cell was operated in potentiostatic mode at 70°C and 100% relative humidity, with H₂/air flow rates of 0.060/0.200 NLPM, and atmospheric back pressure.

6.3 Results and discussion

Fibre diameters in the free-standing nonwovens before and after heat-treatment are reported in Figure 34.

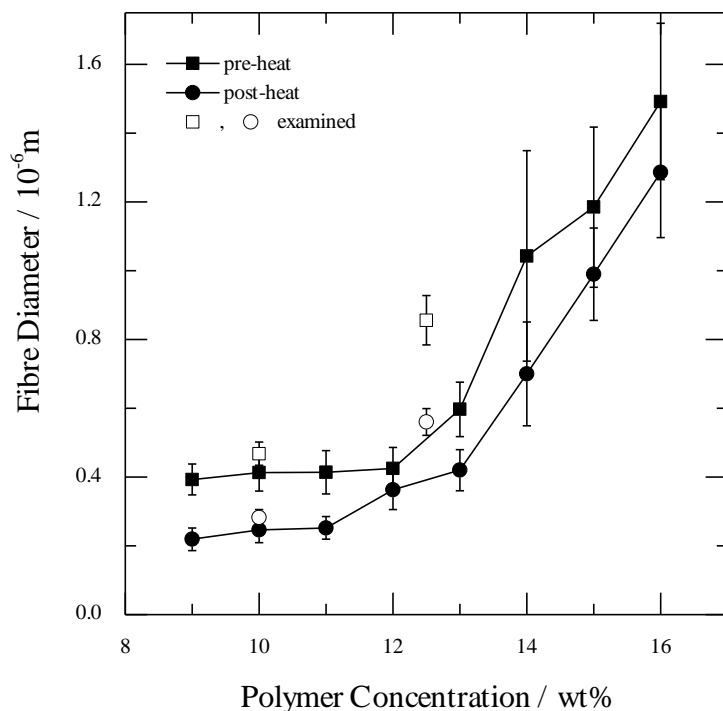


Figure 34: Plot of fibre diameter as a function of polymer concentration in the electrospinning dope.

As polymer concentration increases, an increase in fibre diameters is observed. This is consistent with the literature and may be attributed to increased polymer chain entanglement at higher concentrations, producing greater solution viscosities, which in turn impact the spinning process [15]. The stabilization and carbonization of the raw fibres produced an average diameter reduction of 190 nm. Following Figure 34, a subset of layers with PAN dope concentrations of 10 and 12.5 wt% were selected for further study; these layers were remanufactured with an approximate 38 μm finished thickness. This selection of concentrations would yield appreciably different fibre diameters whilst the moderate dope viscosities facilitate electrospinning. Due to relative humidity variations, fibre diameters of the thicker layers do not lie upon the original curve but follow a similar trend with polymer concentration. Upon examining the morphology, we observe our synthesis yields a continuous fibre nonwoven without defects at the fibre (i.e. broken fibres and shives) or layer (i.e. cracks) levels. We hypothesize that the continuous fibre morphology may reduce the occurrence of cell damage compared to MEAs with carbon paper transport layers without MPLs, where individual fibres may punch holes through membranes. This suggests an electrospun, fibrous,

MPL could supplant contemporary MPL inks; and maintain the mechanical integrity of the CCM.

Electronic through-plane area resistance of the PTLs is plotted in Figure 35. The commercial material has error based on the results of chapter 4 ; electrospun results are for a single measurement (sample) extracted from the electrospun layers (which are limited in area, and must supply all tests).

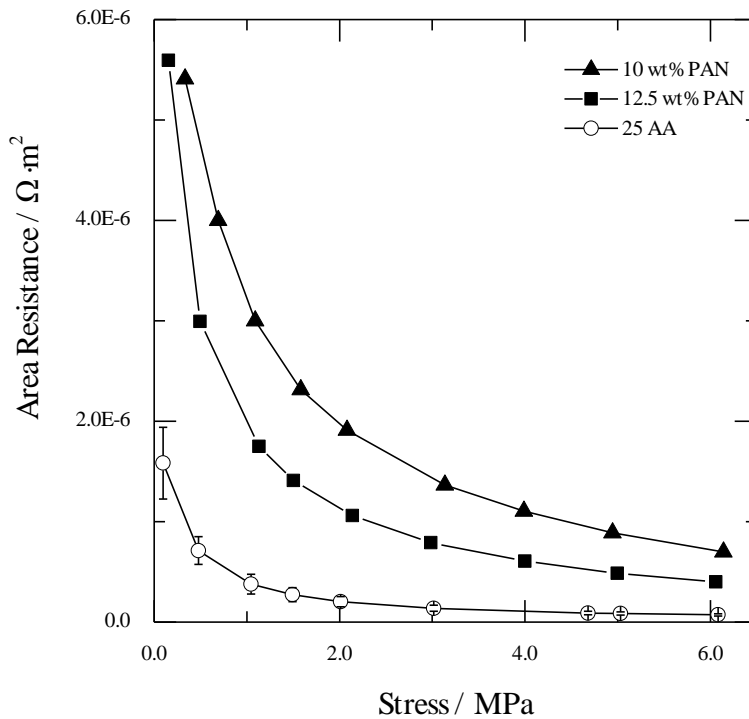


Figure 35: Area resistance as a function of applied stress for experimental materials (post-heat-treatment) and commercial PTL.

As spinning dope polymer concentration increases, there appears to be a trend towards lower resistances. We avoid speculation on whether the effect manifests in the bulk material or the contact interfaces, as a rigorous distinction between contact resistance and material resistivity is unavailable (see Chapter 4). The resistances of our materials are promising for transport layer application (when nominal compression is applied) when compared to contemporary membrane contributions which can be approximately $5.4 \times 10^{-6} \Omega \cdot m^2$ (27.5 μm thick Nafion XL, DuPont); suggesting that the peak temperature used for carbonization is effective. Indeed, permutations to our manufacturing process, such as incorporation of conductive additives (e.g. carbon nanotubes) to the spinning dope, may improve conductivity. However specific

strategies must contend with the parameter sensitivity of the electrospinning process [163] (viz. increasing the current carrying of the dope and consequently altering product morphology). Notably, the electrospun PTLs were not visibly damaged during compression. A concern was breakage (e.g. crumbling) of the layers, whose susceptibility is a function of carbonization temperature. This concern was ultimately placated when electrospun layers were found unbroken post in-situ testing.

Polarization curves from MEAs featuring electrospun PTLs are illustrated in Figure 36.

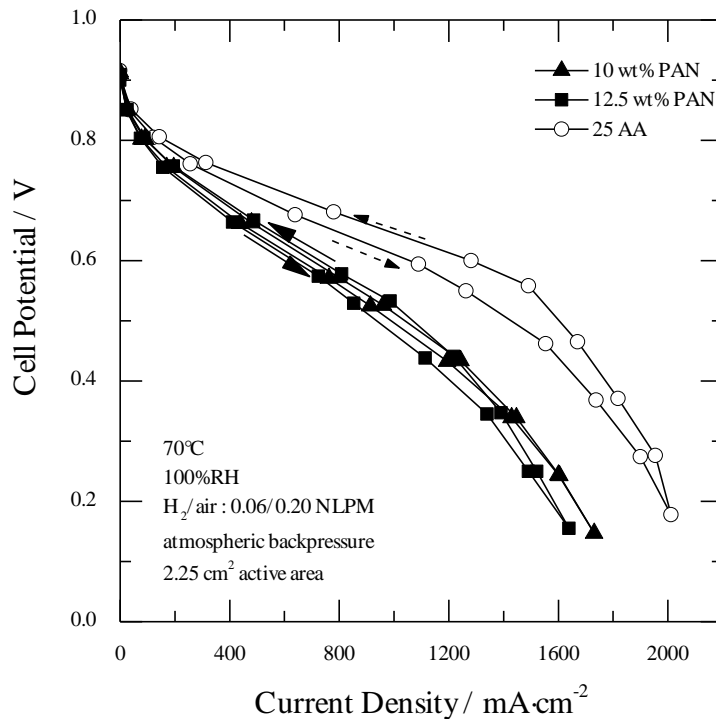


Figure 36: Polarization curves of MEAs featuring cathode PTLs manufactured via electrospinning; also included are results of an MEA featuring a commercial cathode PTL.

Addressing each of the kinetic, ohmic and mass-transport domains in turn: We observe no difference in the kinetic domain for the different transport layer configurations; as should be the case without CL manipulation. The ohmic domain suggests greater resistance in MEAs using electrospun transport layers versus the commercial baseline. Of the electrospun transport layers, we observe no appreciable difference between the 10 and 12.5 wt% PAN. This is congruent with the results from ex-situ area resistance characterization. The relative difference in ohmic contributions in-situ between commercial and electrospun implementations is not as

great as that from ex-situ characterization; but a more appreciable difference between the two electrospun layers might have been anticipated in-situ. Certainly the large ionic resistance of the membrane is a buffer; but other effects manifest in-situ which may confound the cell resistance contributions: the membrane resistance is a function of hydration and is inextricably linked to water transport (and the transport media); the inter-component contact resistances which are structure sensitive; and the distribution of compressive stress, a function of cell and material design. In our experiments the MEAs with electrospun cathode transport layers are thinner than the commercial baseline. It is thought these interact with the cell seal and compression design (which is optimized for commercial MEA thicknesses) to lower overall electrical connectivity between components. The lower connectivity and the proportionally small contribution of PTLs to the total resistance would produce the in-situ similarity between electrospun PTLs, but dissimilarity to the commercial product. However, we suggest that optimization of ohmic losses is only one aspect of electrospun PTLs; and that further improvement over commercial PTLs may be realized in mass-transport performance via the process's morphological control potential. Exploring such improvements are beyond the scope of the present thesis due to insufficient test infrastructure.

The electrospun transport layers operate at approximately 85% of the limiting current density of the commercial product at 0.1 V. The mass-transport overpotential, which is extracted from the empirical fit proposed in [164], is presented in Figure 37.

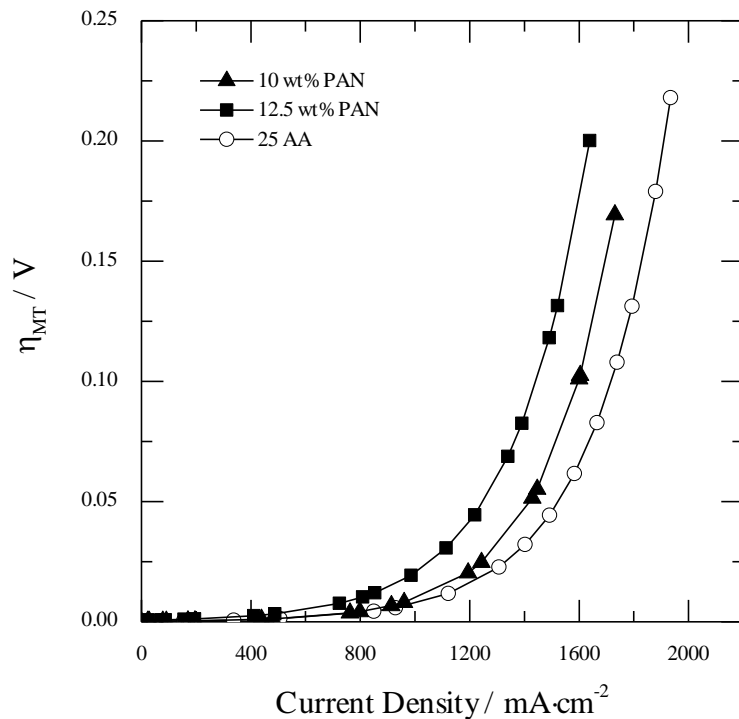


Figure 37: Mass-transport overpotentials of the different MEAs calculated from a voltage breakdown analysis.

The 10 wt% PAN electrospun layer produces a lower overpotential than the 12.5 wt% PAN, whilst both exhibit a greater mass-transport overpotential versus the commercial product. Both electrospun and commercial layers had sessile drop contact angles measured to be $140 \pm 5^\circ$, see Figure 38, suggesting similar affinity for water at layer peripheries.

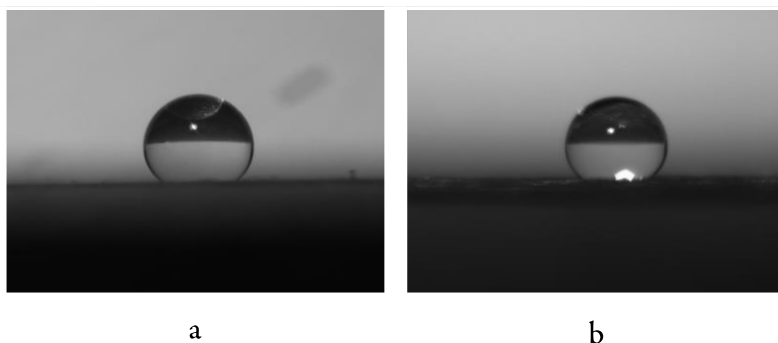


Figure 38: Images of sessile drop contact angle measurement (a) 10% PAN electrospun and (b) commercial PTL. The observed contact angles of the electrospun (10 wt% and 12.5 wt% PAN) and commercial PTLs were indistinguishable at $140 \pm 5^\circ$.

Based on these measurements, we suspect that similar in-situ water interactions may exist at the CL-PTL and BPP-PTL interfaces, and therefore our observed differences in mass-transport overpotential might be attributable to bulk phenomena within the layers (e.g.: internal water distribution, effective diffusivities, etc.). Further diagnosis is beyond the scope of the present study; the structure-property-performance relationship remains a contemporary challenge in the PEM fuel cell community.

Further comparing electrospun and commercial products, there is greater hysteresis in the forwards and backwards polarization curve sweeps of the commercial MEA. Progressing with a step-wise polarization curve from high-to-low average current densities requires at each new step the expulsion of excess liquid water from the previous step(s). This excess water better hydrates the ionomer phase, producing a transient of higher performance. As the equilibration time allotted at a given step is consistent for electrospun and commercial layers; the smaller difference between forwards and reverse sweeps for the electrospun layers suggests this excess water condition is more quickly alleviated. Assuming similar water saturation at the limiting current, we posit that the commercial cathode transport layer has a higher tendency to retain water (viz. a slower evacuation of liquid water from the MEA when approaching equilibrium at a new operating point). Depending on the application, the longer retention may or may not be a desirable behaviour, e.g. in a shutdown procedure drying the MEA of water can be desirable to avoid ice-damage in freezing climates. Not depicted in Figure 36, but observed during testing, was a greater propensity for cell flooding with the commercial transport layer versus the electrospun layers. Figure 39 presents polarization curves including time-series information in quantile form. The bounds represented by the boxes and whiskers represent the 5, 25, 50, 75 and 95% quantiles of the observed current densities at a given potentiostatic set-point.

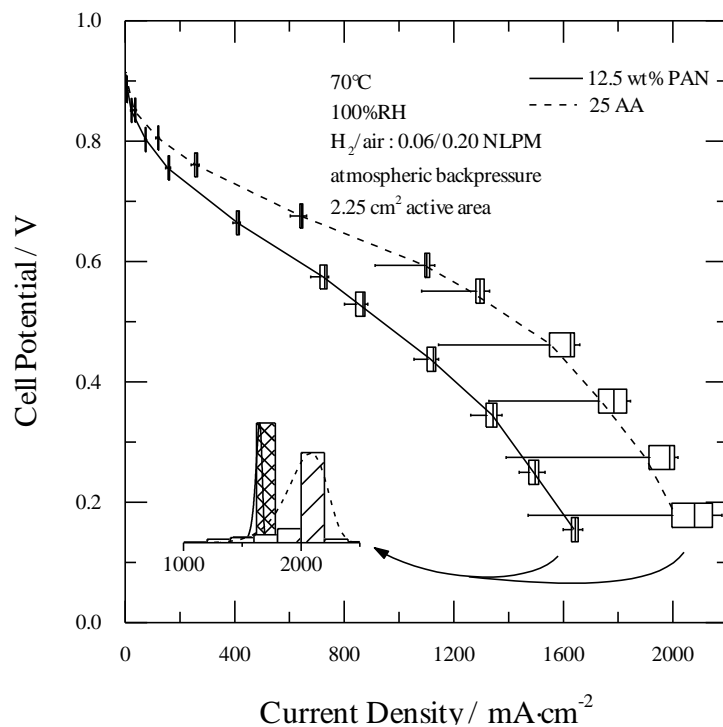


Figure 39: Polarization data of 12.5 wt% PAN electrospun and commercial PTLs presented as 5, 25, 50, 75 and 95% quantiles of observed current at fixed potential. The inset plot comprises histograms and Weibull distributions of the currents densities at minimum potential. 10 wt% PAN and reverse polarization sweep data are not presented for sake of clarity.

As the average current density increases, so does water production. Liquid water creates flooding transients which widen and skew distributions of current densities. The electrospun PTL equipped MEA has a demonstrably narrower distribution versus the commercial product; this is reinforced in the inset of Figure 39 which plots current density histograms and associated Weibull distributions. In real applications, the greater fuel cell operating point stability conferred by electrospun PTLs may simplify control algorithms and regulating electronics.

6.4 Summary

PEM fuel cell transport layers were produced by the novel application of electrospinning. By varying polymer concentration in the spinning dope, control over fibre diameters in the nonwoven layers was demonstrated. The materials demonstrated acceptable mechanical stability for cell assembly, whilst electronic resistances were comparable to commercial material

ex-situ and in-situ. Contact angle measurements suggest similar surface hydrophobicity for electrospun and commercial materials. We demonstrate promising in-situ performance from cell tests; with electrospun layers achieving approximately 85% peak currents of the commercial baseline, faster water transport, and greater output stability. We remark that this cell had been optimized for the commercial materials, design modifications may close the performance gap. With synthesis refinements, further performance can be expected over our currently non-optimized materials. The flexibility inherent in electrospinning techniques may enable deterministic links between structure, properties, and function in PTL materials.

7 Implication of PEM fuel cell transport layer in-plane anisotropy

We report on a novel method for the synthesis of fibre-based PEM fuel cell PTLs with controllable fibre alignment. We also report the first application of such layers as a diagnostics tool to probe the effect of within-plane PTL anisotropy upon PEM fuel cell performance. These structures are realized via adaptation of electrospinning technology and a high-speed drum target. Electrospun layers with progressive anisotropy magnitude are produced and evaluated. This novel approach is distinguished from the state-of-the-art, as an equivalent study using commercially available materials is impossible due to lack of structurally similar substrates with different anisotropies. Transport layer anisotropy is visualized via SEM microscopy, and quantified using electronic resistivity. We confirmed our capability to achieve fibre alignment, and the associated impact on transport properties. A framework is presented for assessing the in-situ performance, whereby transport layer anisotropy orientation versus bipolar plate flow-field geometry is manipulated. While an effect upon the commercial baseline could not be discerned, electrospun transport layers with greater anisotropy magnitude suggested greater sensitivity to orientation; where greater performance was obtained with fibres predominately cross-aligned to flow-field channels.

7.1 Introduction

PEM fuel cell systems command attention in the nascent hydrogen energy paradigm. The MEA is the critical component which facilitates the chemical to electrical energy transformation. MEAs themselves comprise multiple (sub-)functional layers; of which the PTL is one. The PTLs are interposed between CL and bipolar plates, and between them mediate energy and mass-transport. As the PEM fuel cell industry moves towards production

emphasis, there is a growing demand for refined characterization and optimization capabilities at material, cell, and system levels.

Contemporary PTL research comprises: the characterization of ex-situ structural and transport properties, and the in-situ description of water-transport phenomena. Generally, these efforts draw from a limited pool of commercial PTL products; often derived from carbon fibre papers. Compared to CL or membrane synthesis research, few transport layer studies have investigated unconventional structures or synthesis paths.

Functional (planar) layers within the fuel cell can demonstrate anisotropic material behaviour; obvious are the property differences between through-plane and in-plane directions, more subtle are the different principal components within in-plane. The latter case is demonstrable in fibre-based porous transport media [1,39,132]. Furthermore, PEM fuel cells exhibit operational inhomogeneities; these may occur at flow-field land-to-groove scale, or at the active area scale [51,131,165]. The literature, experimental and modelling, which acknowledges fuel cell material anisotropy is sparse.

We report on an experimental investigation of transport layer anisotropy implications upon PEM fuel cell performance. We escape the restrictions imposed by limited transport layer permutations by leveraging electrospinning synthesis. Our previous efforts demonstrated the proof-of-concept for this method of transport layer creation [2]. In this study, we employ the technology to create structures with controlled in-plane anisotropic structures. Our two-fold aim is to further the viability of electrospinning: as a means of creating rationally designed transport media; and also as a diagnostics tool to elucidate the PEM fuel cell structure-property-performance relationship.

7.2 Background

Three directions may be used to resolve the properties of fibre-based transport layers: within-plane are FAD and FXD directions; and through-plane direction. The transport layers interface with adjacent functional layers within the fuel cell: CL or MPL, and bipolar plate flow-field channels. Owing to different transport characteristics along different directions, by rotating a transport layer we may expect a performance effect. Assuming isotropy of the CL (or MPL), transport layer orientation within the cell can be described by the alignment of FAD versus flow-field channel geometry. Figure 40 illustrates this study's definitions of aligned and cross-aligned orientations.

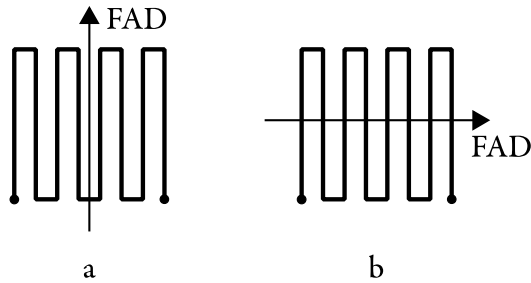


Figure 40: Illustration of transport layer anisotropy orientation versus flow-field channel geometry: aligned (a) and cross-aligned (b).

The effects of transport layer in-plane anisotropy may manifest within its bulk and/or at the interfaces with adjacent layers. Furthermore, transport layer anisotropy may interact with the operational inhomogeneities at the land-channel and/or active area length scales. While the former is relatively more studied (e.g. in unit cell modelling), implications of the latter may develop as commercial systems move towards higher aspect ratio designs. There is presently no consensus on which mechanisms determine the contribution to cell performance, nor if said contribution is significant in magnitude. Figure 41 illustrates possible mechanisms.

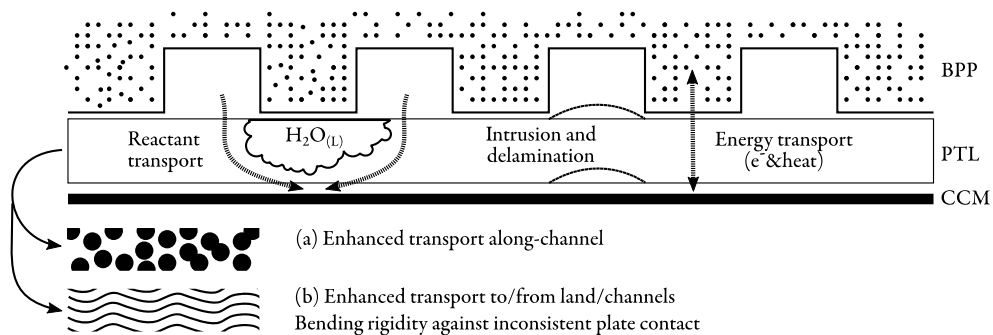


Figure 41: Illustration of transport layer interaction with adjacent functional layers: FAD aligned to major length (a), and FXD aligned (b).

Han et al. investigated the relation between anisotropic PTL bending stiffness and PEM fuel cell performance [138]. Ex-situ, they measured a greater bending stiffness in the machine direction versus the cross machine direction. In-situ, they tested both aligned and cross-aligned transport layer orientations; a consistently lower high-frequency resistance for the cross-aligned configuration produced better performance. Han et al. attributed this to delamination between the PTL and CL caused by PTL bending from non-continuous bipolar plate contact, whereby the PTL orientation which better resisted the bending yielded less delamination (and flow-field channel intrusion). Soe Naing et al. investigated the role of PTL orientation from a water management perspective [139], using a visually accessible cell to monitor in-situ liquid water

motion at the cathode. They observed smoother water removal for the cross-aligned PTL configuration. Additionally, a second cell platform was used to freeze water in-situ. Imagery suggested greater liquid water saturation of PTLs below lands for aligned configurations, and a more even land-to-channel distribution for the cross-aligned configuration. Soe Naing et al. attributed their orientation dependent cell performance to this difference in liquid water saturation. Additional performance influences may derive from preferential in-plane transport for: reactants [39], charge [1,132], and heat [137].

The aforementioned studies are encumbered by limited selection of commercial PTL products. Soe Naing et al. reported results for one substrate, while Han et al. reported for a pair each of papers and felts. To probe the influence of transport layer orientation, it may be desirable to evaluate substrates with differing magnitudes of in-plane fibre alignment. Selecting commercial paper and felt substrates might offer two points on this spectrum, but there is no progression in between. Moreover, the morphology between these substrates is so strikingly different, that it may not be prudent to amalgamate results.

Electrospinning offers a synthesis path for producing fibre-based layers not unlike commercial PEM fuel cell PTLs [2]. Electrospinning is a procedure whereby a polymer solution (or melt) is drawn by an electric field from a capillary tip onto a target. The technology is attractive because manipulations of solution, spinning, or hardware configurations can effect different product layer morphology [15]. Methods of creating aligned fibre mats are reported in the literature; these are broadly classified into methods acting mechanically (e.g. rotating drum target) or via electric field perturbation (e.g. parallel strip target). Teo and Ramakrishna offer an illustrated review in [29]. In the present study, we apply the high-speed drum target technique. This permits us to generate layers of consistent general appearance with progressively greater alignment as drum rotation speed is increased – and escapes the major limitation of using commercial substrates. We quantify the alignment within our layers by an electronic resistivity approach. Current may transport preferentially along fibre versus across adjacent fibres, so a higher FXD value is predicted versus the FAD result. This approach is supported by analogous work by Kok and Gostick, who studied the in-plane permeabilities of electrospun membranes [166].

Our study is distinguished by application of our novel PEM fuel cell transport layers. It is beyond the scope of the present study to assign specific mechanisms to observed anisotropy related performance differences. Herein we present a materials and testing framework, upon which future diagnostics may be applied to identify the aforementioned mechanisms. Manipulable anisotropy enables probing the limits of its effect. Moreover, our synthesis approach itself constitutes a unique opportunity for the creation of optimized structures.

7.3 Method

7.3.1 Materials

PAN (approx. 150000 Mw) was obtained from Scientific Polymer Products and DMF ($\geq 99.9\%$) from Fisher Scientific. These were used without further preparation.

7.3.2 Transport layer preparation

PAN was dissolved in DMF to produce solutions of 12 percent weight; this polymer concentration was chosen based on previous experience in controlling spinning parameters [2]. Electrospinning was performed using a MECC Co. NANON device; the system was equipped with a drum collector capable of high rotational speed. The system was configured with a: bias voltage of 11 kV, 100 mm tip-to-target distance, 18g capillary spinneret, and 150 mm spinneret traverse width at $1 \text{ mm}\cdot\text{s}^{-1}$. Solution was delivered at an average rate of $1.0 \text{ mL}\cdot\text{hr}^{-1}$; over the duration of a session, the flow rate was regulated to sustain spinning and prevent drips. Drum rotation speed was manipulated to effect change in fibre alignment of the layers; these are reported in Table 6. Post-processing of the raw spun material follows our previously reported procedure [2]: green layers are sandwiched between alumina plates to maintain shape; stabilized at 240°C for two hours at a $1^\circ\text{C}\cdot\text{min}^{-1}$ ramp rate; and carbonized at 900°C for one hour at a $5^\circ\text{C}\cdot\text{min}^{-1}$ ramp rate. The results are self-supported carbon-fibre mats which directly applicable in the porous transport layer role.

Table 6: Details of the electrospun transport layers produced in this study.

Drum speed [RPM]	Surface speed [$\text{m}\cdot\text{s}^{-1}$]	Thickness [μm]	Fibre diameter [μm]	Anisotropy Ratio [-]
100	1.0	52	0.63 ± 0.06	1.1
500	5.2	51	0.84 ± 0.11	2.3
1000	10.5	54	0.87 ± 0.11	6.2

7.3.3 Ex-situ characterization

SEM micrographs were acquired from a Hitachi S3000N microscope and analyzed using ImageJ software. Anisotropy of transport layers was quantified using an electronic resistivity approach following our previous work [1]. A square electrode arrangement permits facile in-plane FAD and FXD resistivity measurement. Negligible change in the anisotropy ratio was observed as a function of strain, therefore single values are reported. The resistivity measurement was replicated twice for each electrospun layer.

7.3.4 *In-situ characterization*

In-situ cell tests of commercial materials feature membrane electrode assemblies (MEAs) composed of Gore PRIMEA catalyst coated membranes and SGL Sigracet transport layers: 25 AA at the anode and cathode for baseline tests; and electrospun cathode and 35 BA anode transport layers for subsequent tests. The thicker (35 series) anode substrate was chosen to meet the MEA design thickness of our hardware.

The test cell bipolar plates feature single-channel serpentine flow-fields with an average channel/land ratio of 0.68. Anode and cathode flow-field channels run parallel to each other, and deliver gas in counter-flow configuration. The cell is operated at 70°C and 100% relative humidity. Air is used as the cathode oxidant and the H₂ and air flow rates are 0.06 and 0.200 NLPM respectively, and are at atmospheric back pressure.

Subsequent to a common conditioning procedure, polarization curves were acquired potentiostatically using the load bank integral to the test station. Cell potential was stepped from high to low to high potentials, and repeated to verify performance consistency.

A baseline using commercial materials was constructed to investigate the influence of in-plane transport layer anisotropy. MEAs were assembled where both transport layers either had FAD or FXD aligned to the major length direction of the flow-field channels; this is illustrated in Figure 40. Eight cells constructed of commercial materials were tested in-situ for each of the two alignment configurations (sixteen commercial MEAs evaluated in total). Each cell itself had two forwards-backwards polarization profiles measured.

Because performance difference(s) between orientations may be non-obvious, the resulting polarization data were fitted to a model equation by Kim et al. [164]:

Equation 30: $E_{cell} = E_0 - b \log(i) - Ri - m \exp(ni)$

This is an empirical equation chosen to describe the polarization curve in as few parameters possible. These parameters' numerical results are not meant to accurately represent specific physiochemical properties (e.g. limiting current density). The data fitting method is required to compile the data from multiple polarization curves and provide a quantitative (statistically valid) method of testing the null hypothesis: "there is no difference between polarization curves obtained with different orientations". A Fisher statistic was constructed for the regression problem whereby: model 1 had all data fitted to Equation 30, and model 2 had Equation 30 fitted for each orientation group. Model 2 comprised adding additional terms to

the original equation to distinguish between orientation groups and testing whether the additional terms provide a statistically significant improvement to the overall fit.

Electrospun transport layers with progressively greater alignment were investigated at the cathode. MEAs were assembled with FAD of these layers either aligned or cross-aligned to the flow-field channels. The anode PTL orientation was kept consistent (cross-aligned). Due to resource limitations, only one MEA was assembled for each electrospun model and orientation. Four polarization curves were extracted from each of these MEAs.

7.4 Results and discussion

The SEM micrographs of Figure 42 clearly illustrates our approach's capability to produce transport layers of controllable fibre alignment; with a electrospinning drum speed of 100 RPM, the finished transport layer has an seemingly random fibre distributions, whilst at 1000 RPM most fibres have aligned along the direction of surface travel. A consideration for choosing the high-speed drum technique for obtaining fibre alignment was an anticipated allowance for some transversely oriented fibres to maintain structural integrity. These fibres are observable in the SEM imagery. While in practice, electrospun transport layer mechanical failures were not observed in our experiments.

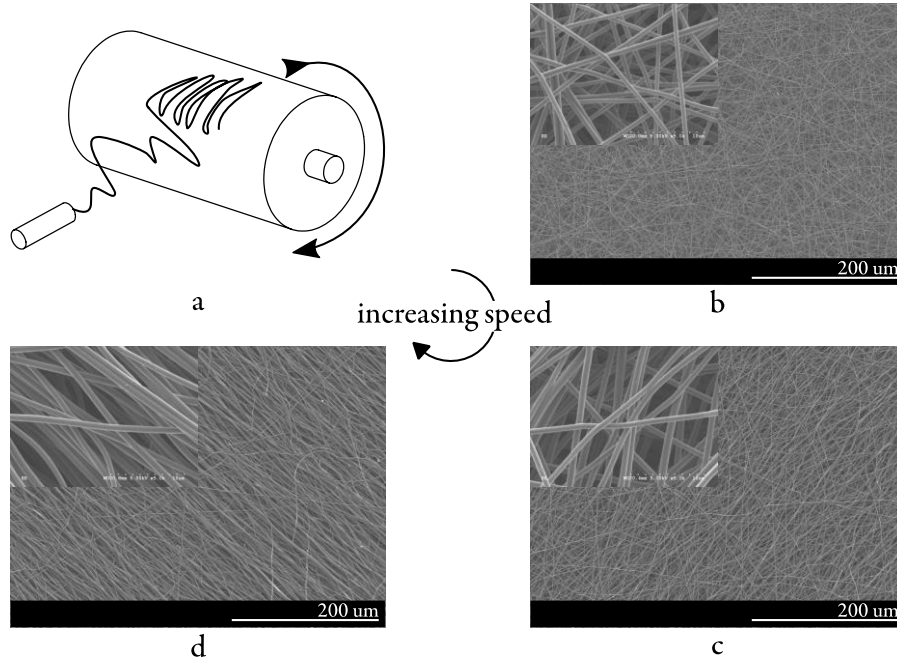


Figure 42: Schematic of electrospinning procedure (a) and SEM micrographs of electrospun transport layers of progressive anisotropy: 100 rpm (b), 500 rpm (c) and 1000 rpm (d).

Electronic resistivity is used to quantify the fibre alignment in the electrospun layers, these results are presented in Figure 43. The anisotropy ratio is the ratio of resistivities in the FXD versus FAD directions. A greater value implies more preferential charge transport along the dominant direction of fibre orientation. The error bars represent the 70% confidence prediction bounds of the least-squares fit to an equation of the form:

Equation 31: $y = ax^b$

The value for SGL 25 AA is also included. As electrospinning target (drum) speed is increased, greater fibre alignment is observed. Effective anisotropy study requires some quantitative measurement technique. The general assumption in electrospinning literature is that, absent from a concentrated effort, the non-woven layers produced are deposited in a random distribution. However we have observed this is not necessarily true. In the early development of the present study, we evaluated the anisotropy (and control thereof) of electrospun layers created using an alternate, slower target speed, platform utilized in our previous work [2] (for both drum and belt). While layers appeared random in SEM imagery, we measured preferential alignment transverse to the target surface speed. Changing target speed within the system's limited range altered the magnitude of anisotropy, but dominant orientation remained in this

non-intuitive direction. We attribute the result to a non-uniform potential field between spinneret and target. Our final choice in electrospinning platform affords the sought control of anisotropy.

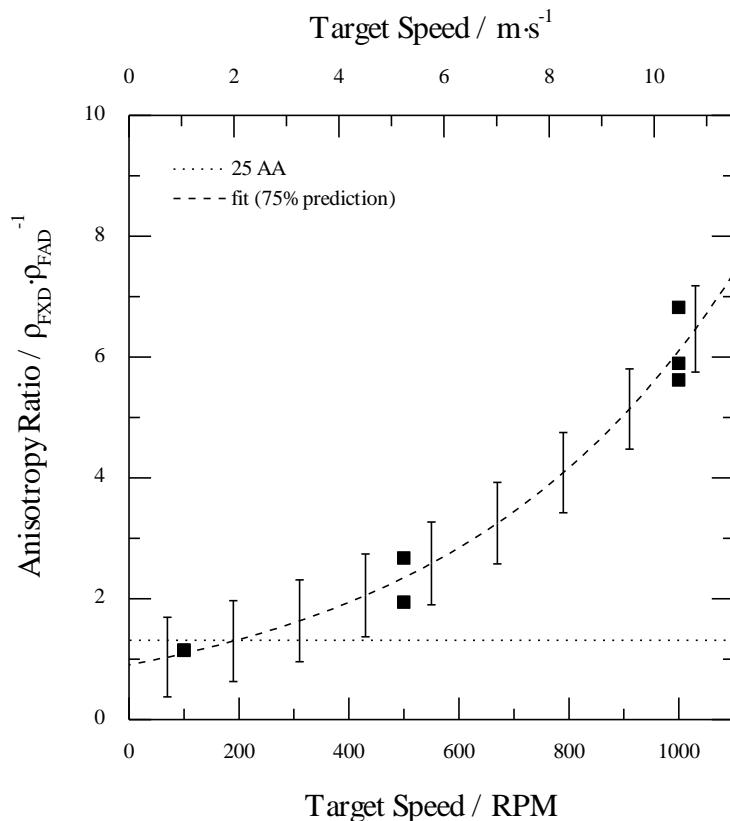


Figure 43: Ratio of resistivities (anisotropy ratio) in the FXD versus FAD directions. A higher value implies greater fibre alignment.

In-situ polarization curve data for cells comprising commercial transport layers with anisotropy either aligned or cross-aligned to flow-field geometry are presented in Figure 44. The contiguous profiles are the fits of Equation 30 with either all data together (i.e. model 1), or with data grouped according to orientation (i.e. model 2). These results represent the cells' steady-state performance. The superimposed normal distributions represent the variability in the point cloud assembled from the sixty-four polarization profiles at each potentiostatic step (2 alignments × 8 MEAs × 4 single direction polarization curve profiles).

Small active area cells are particularly susceptible to performance transients owing to flooding (e.g. water droplet formations and expulsion). In Figure 45 we represent the underlying time-series information. For each potentiostatic step, the deltas between mean and instantaneous

current densities (acquired at 1 Hz) are compiled for all polarization curves of a specific orientation configuration; these are subsequently fit with a Weibull distribution and superimposed over the steady-state polarization curve data. The result is a depiction of the temporal performance variability. Distributions are scaled to compare between FAD and FXD results at any one cell potential.

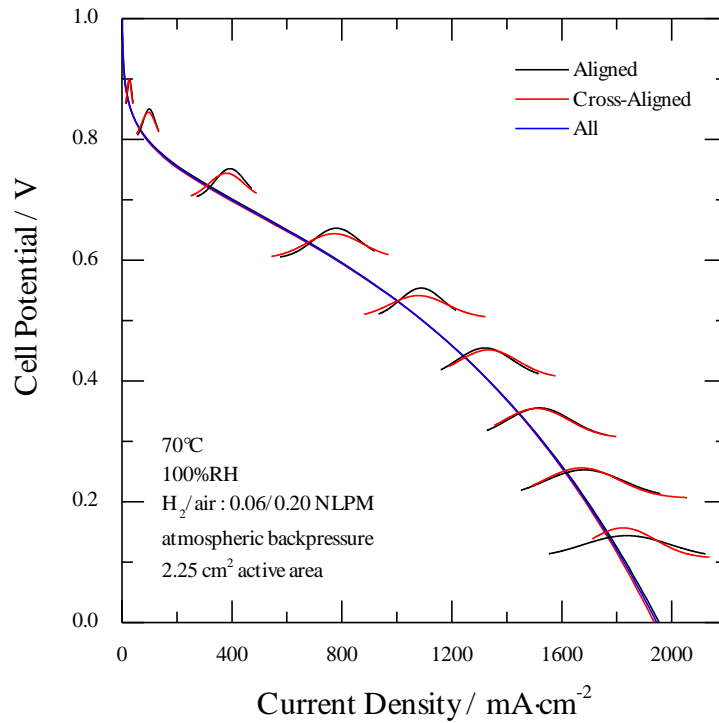


Figure 44: In-situ polarization results for baseline (commercial material) cells assembled with transport layer anisotropy either aligned or cross-aligned to flow-field geometry. Curves are fit following Equation 30, with superimposed distributions for different alignments at the potentiostatic measurement steps.

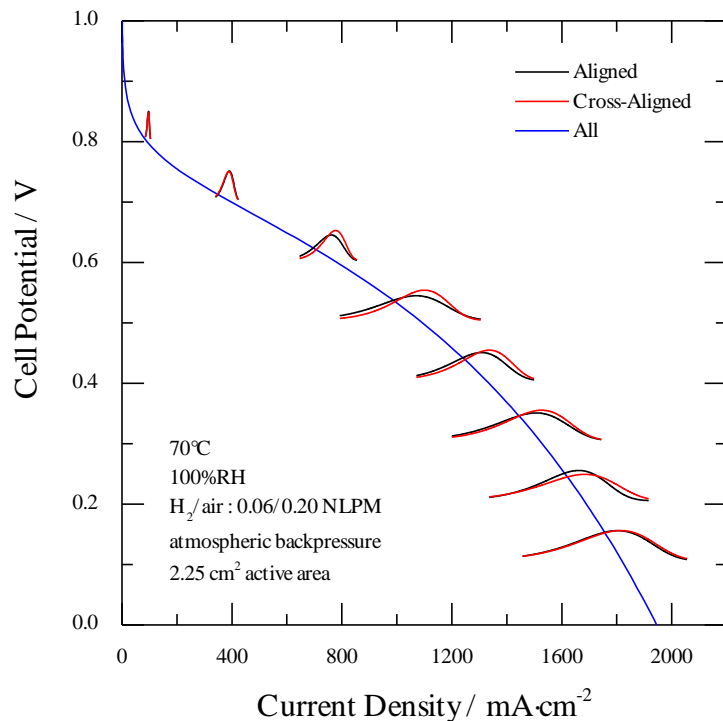


Figure 45: In-situ polarization results for baseline (commercial material) cells assembled with transport layer anisotropy either aligned or cross-aligned to flow-field geometry. The contiguous curve is the fit of Equation 30 to all steady-state data, whereas the superimposed distributions reflect the underlying time-series data acquired at 1 Hz for different alignments.

Inspection of results does not suggest a steady-state or transient performance difference based on transport layer orientation. Any difference either does not exist or is small compared to cell-to-cell performance variability; the Fisher statistic we calculated is less than one, suggesting at least the latter is plausible. We caution this result is strictly only applicable to our configuration of: MEA, cell hardware, and operating conditions; other configurations might reveal an orientation influence (as was reported in the literature). Consequently, we are developing our electrospun transport layers with manipulable anisotropy as an avenue for rational cell design, and as a diagnostics tool to probe the limits of in-plane transport layer anisotropy upon cell performance.

Polarization data for cells featuring electrospun transport layers of progressively greater in-plane anisotropy aligned and cross-aligned to flow-field geometry are presented in Figure 46.

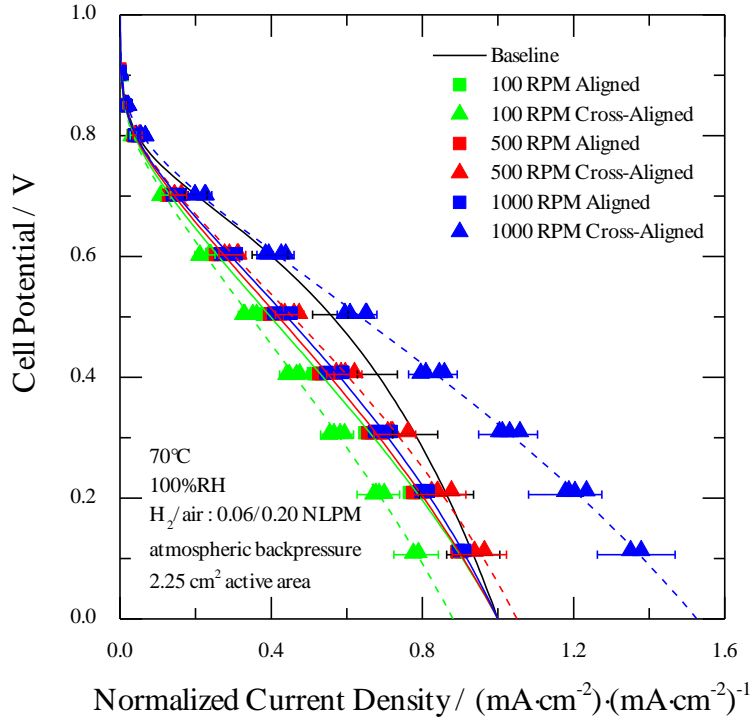


Figure 46: Normalized in-situ polarization results for cells featuring electrospun cathode transport layers of progressively greater in-plane anisotropy in different orientations versus flow-field geometry.

Continuous curves are fits of Equation 30 and measured data are plotted as markers. Current densities for a given electrospun material are normalized such that the value of the FAD configuration limiting current density is unity. This representation is chosen to detach the orientation effect from any substrate-specific average performance advantage. The baseline curve is developed from the commercial material tests, and is an average of the two curves of Figure 44. There are insufficient data to conduct a rigorous error analysis of the electrospun layer performance; we instead produce a preliminary estimate of variability based on the commercial material baseline tests. The standard deviations of the current densities from the baseline dataset are treated as a function of potential; these are converted to percent standard deviations based on the average current density at each potential. This percent standard deviation is assumed to apply consistently for our test platform. Using the current densities observed with the electrospun MEAs the percent standard deviation can be converted back to an absolute value (and then normalized by limiting current density for representation in Figure 46). The error bars represent plus or minus one standard deviation and are plotted only for the cross-aligned curves for clarity (they are similar in size for the aligned curves). The outcome is

a measure of measurement error, but excludes potential sample variability. We do not include an illustration equivalent to Figure 45, as no effect was discernable in the time-series data.

Inspecting Figure 46, the performance impact of transport layer orientation appears to increase with anisotropy magnitude. The lower anisotropy electrospun PTL suggests better performance with FAD aligned to flow-field geometry; however its anisotropy ratio is less than the baseline, therefore an orientation effect would not be expected. Its result is also falling into our uncertainty. The two electrospun PTLs of greater anisotropy ratio suggest better performance with FAD cross-aligned to flow-field geometry; this is consistent with the literature. Moreover, the electrospun transport layer with the greatest anisotropy ratio demonstrates the greatest sensitivity to orientation. Again, it is not possible with our available data what loss mechanisms (i.e. OCV, activation, Ohmic and mass-transport) are attributable to observed performance differences. A consistent CCM was used for all tests, therefore it is reasonable to assume that OCV and activation losses are also consistent. While a limit upon the bulk PTLs' contribution to ohmic losses might be estimated from ex-situ results; this does not readily translate to in-situ results. In-situ complications arising from contact resistances and humidification-dependent membrane conductivity are likely to overshadow. Finally in the mass-transport regime, a means to evaluate water saturation and distribution in-situ would be needed to supplement any ex-situ flow measurement (or model) such as permeability. Nevertheless, we demonstrate an effective framework for synthesis and characterization promising for continued investigation.

7.5 Summary

We have reported a novel method for the synthesis of fibre-based PEM fuel cell transport layers with progressive fibre alignment. These structures were realized through adaptation of electrospinning. Fibre alignment was visually and quantitatively confirmed. Transport layer fibre alignment, in commercial or electrospun materials, effects anisotropic transport properties within-plane. We surmised that the relative orientation of transport layer anisotropy versus the bipolar plate flow-field geometry may yield different performance. Accordingly, we applied our electrospun transport layers as a diagnostics tool. Our approach is distinguished from the literature by the unique application of structures with prescribed (progressive) anisotropy. A framework was detailed for assessing the in-situ performance implication of PTL anisotropy orientation. No effect was observed for the commercial material baseline (although an effect has been reported in literature), suggesting our result may be a product of our specific test configuration. Encouragingly, electrospun transport layers with greater anisotropy magnitude demonstrated greater sensitivity to layer orientation; where greater performance was

achieved with fibres cross-aligned to flow-field channels. However material and testing resources limited the present study to only a few samples. This work is the first application of PEM fuel cell transport layers with manipulable in-plane anisotropy, and consequently also the first to use said layers to investigate the implication of anisotropy orientation. It highlights the importance of anisotropy-aware experimentation and modelling. It also resonates with the goal of a structure-property-performance relationship, where creation of deterministic structures may clarify performance interpretation. Future work may comprise further tests to identify by which mechanisms does transport layer orientation affect cell operation.

8 Conclusion

The present thesis advances novel PEM fuel cell transport layer characterization, synthesis, and diagnostics research. The transport layers mediate energy and mass transport within the fuel cell. However, contemporary transport layer implementations have limited capacity for optimization. Moreover, contemporary characterization techniques lack critical consideration for anisotropic material behaviour. Herein, a novel transport layer synthesis paradigm is introduced. Furthermore, the state-of-the-art for characterizing transport layers in general is advanced. These outcomes agree with the needs of contemporary PEM fuel cell research and industrial development. Improved understanding of the structure-property-performance relationship, coupled with a synthesis method which affords heretofore unavailable structural manipulability, progresses the technology's rational design potential. Additionally, the improved tools offer a precedent from which industrial standards may derive.

Contributions include:

- Demonstrating novel electrospun transport layers for PEM fuel cells. This was the first reported application of electrospinning to create such layers with controlled morphology. Ex-situ and in-situ performance were comparable to conventional fuel cell PTLs.
- Controlling fibre diameters and fibre alignment within transport layers. Contemporary transport layer synthesis methods are comparatively inflexible; by adaptation of electrospinning, this is the first report of these parameters being controlled for PTLs in general.
- Reporting the principal components of in-plane electronic resistivity as a function of mechanical strain for PTLs of different thicknesses and PTFE contents. This necessitated development of novel apparatus and methods. It was determined for through-plane resistivity that only a micro-electrode configuration might rigorously exclude contact resistance effects.

- Introducing a novel framework for diagnosing the effect of transport layer anisotropy upon fuel cell performance. Model structures were synthesized over a spectrum of fibre alignments and had anisotropy uniquely quantified by electronic resistivity. Results suggested increased performance for fibre alignment perpendicular to the flow-field channels. The method enables a novel independent variable by which cell performance may be interpreted.

A novel method for acquiring three-dimensional electronic resistance information of PEM fuel cell PTLs was presented. A unique contribution was in-plane anisotropic resistivity acquisition via square 4PP arrangement as a function of mechanical strain. Resistivities in the range of 4.5×10^{-4} to $1.5 \times 10^{-4} \Omega \cdot \text{m}$ were observed over a range of strains from 0.0 to $-0.5 \text{ m} \cdot \text{m}^{-1}$. The rigorous attention given to the anisotropy of the fibre-based media contrasted the simplifications common in the literature. Furthermore, approaches from the literature for isolating contact resistance effects were critiqued; those assuming to neglect certain contact contributions and/or combining superficially similar media were deemed inappropriate. This work was subsequently extended to investigate the outcome of cyclically applied deformation. Plastic deformation of PTLs was quantified and related to the electronic response; the permanent set in both behaviours affirmed the fibre network's susceptibility to damage. Moreover, we presented feasibility of a sheet resistance measurement to estimate the peak strain experienced. This minimum-contact and non-destructive approach is particularly adaptable for on-line quality monitoring, though further study is required to harmonize the effects of other damage scenarios. No industry standards are yet established for the control of fuel cell transport layer electronic resistivity. As membrane conductivities improve with successive generations, the ohmic losses incurred by PTLs and other functional layers shall grow in significance. Moreover, as PEM technology progresses, a consistent language of materials specification is requisite for a sustainable supply network.

PEM fuel cell transport layers were produced by the novel application of electrospinning. Electrospinning offers simplified single-step generation of fibre structures, unlike contemporary PTL manufacturing methods. Adaptation of this technology allowed unique structures with controlled morphology to be realized; control over fibre diameters was demonstrated by varying synthesis parameters. A range of fibre diameters from approximately 0.2 to $1.6 \mu\text{m}$ was achieved. The electrospun transport layers were compared both ex-situ and in-situ versus a commercial baseline. Electrospun layers demonstrated sufficient mechanical strength and electronic conductance, whilst contact angle measurement suggested similar surface hydrophobicity ($140 \pm 5^\circ$). In cell tests, electrospun layers achieved performance approaching that of the commercial baseline (approximately 85% of the baseline peak current

density); cell design or operating condition optimization favouring the electrospun layers may close this gap. Additionally, the layers themselves may be refined. The promise of incorporating functional elements directly into layer synthesis, and of conceivably generating monolithic functional layers (or MEAs), are expressions of electrospinning's potential for streamlined, scalable and adaptable manufacturing.

Finally, electrospun transport layers themselves were developed as a diagnostics tool to probe the effect of within-plane transport layer anisotropy upon PEM fuel cell performance. It was surmised that the relative orientation of transport layer anisotropy versus the bipolar plate flow-field geometry may yield different performance. Some studies exist in the literature where commercial PTLs were utilized; however the state-of-the-art is limited by said limited scope of commercial PTLs. In the present thesis, electrospun layers with progressive fibre alignment, and thus anisotropy magnitude, were produced and evaluated. An equivalent study using commercially available materials is impossible due to lack of structurally similar substrates with different anisotropies. Electrospun PTL anisotropy was visualized via SEM microscopy, and quantified using the aforementioned electronic resistance methods. Based on a ratio of in-plane electronic resistivities, a range of anisotropy ratios from 1 to 6 was achieved. A framework was detailed for assessing the in-situ performance. Preliminary results suggest improved performance where the FAD is arranged perpendicular to the major flow-field direction (by approximately 50% in limiting current with the highest anisotropy configuration); which is accordance with the literature. This work is the first application of PEM fuel cell transport layers with manipulable anisotropy, and consequently also the first to use said layers to investigate the implication of anisotropy orientation; it consolidates and harmonizes the synthesis and characterization themes of the present thesis.

Future work should aim to resolve some of the challenges encountered in producing this thesis. These challenges relate to: the synthesis of electrospun PTLs; the characterization of PTLs; and the application of PTLs in-situ.

- The minimum of apparatus needed to create electrospun layers masks the complexity of the process. Although the present thesis used purpose-built commercial electrospinning systems, their use was tempestuous. A similar set of polymer-solution-spinning parameters could yield different results month-to-month. This was mitigated by conducting all synthesis for a given study in the shortest time window possible. Obviously there remains missing control over some parameters. Based on experience, the environment is most suspect (humidity and temperature affect solvent drying as fibres are drawn). Specifications for an improved system must include temperature and

humidity control of the spinning environment (with care given to side-effect air currents). Given a system producing repeatable structures, the second priority should be modelling synthesis parameters versus product structure; this would allow specification of a desired outcome rather than trial-and-error. A first step would be factorial experiment designs around porosity and tortuosity response variables.

- The characterization of PTLs can be enhanced with mass-transport information about the void phase. Such information would aid interpretation of in-situ performance. Neglecting liquid water saturation, knowledge of the (dry) transport properties could be used to put bounds on anticipated performance benefits of manipulating certain structural parameters. Effective diffusivity is the ideal measurement, although permeability may suffice. The challenge is establishing an anisotropy-aware method for acquiring this data.
- The in-situ study of electrospun transport layers would benefit from the above recommendations in addition to more extensive testing to determine the effects of PTL structure upon cell performance. Factorial design of experiments may determine empirically which structural parameters (and at which operating conditions) dominate performance (e.g. using peak power as the response variable). Electrospun PTLs are unique by offering new morphological parameters to vary as factors. This model would quantify the effects and interactions of factors; but not provide mechanistic detail. As described above, ex-situ mass-transport information would assist interpretation of cell performance. Further insight requires water management data; water balance methods are initial station enhancements which would help quantify water fluxes within the MEA.

The present thesis' contribution to the state-of-the-art resonates with the objective of a PEM fuel cell structure-property-performance relationship. The flexibility demonstrated in electrospun transport layer synthesis may realize deterministic structures. The advancements in ex-situ characterization contribute to a comprehensive description of properties. Finally these pathways enabling rational design may be exploited to elucidate and optimize performance.

References

- [1] Todd D, Schwager M, Merida W. Three-Dimensional Anisotropic Electrical Resistivity of PEM Fuel Cell Transport Layers as Functions of Compressive Strain. *J Electrochem Soc* 2015;162:F265–72. doi:10.1149/2.0611503jes.
- [2] Todd D, Mérida W. Morphologically controlled fuel cell transport layers enabled via electrospun carbon nonwovens. *J Power Sources* 2015;273:312–6. doi:10.1016/j.jpowsour.2014.09.095.
- [3] Grubb WTJ. Fuel Cell. USPTO 2,913,511, 1959.
- [4] Barreto L, Makihira a, Riahi K. The hydrogen economy in the 21st century: a sustainable development scenario. *Int J Hydrogen Energy* 2003;28:267–84. doi:10.1016/S0360-3199(02)00074-5.
- [5] Winter CJ, Nitsch J. Hydrogen as an energy carrier: technologies, systems, economy. New York, NY: Springer-Verlag New York Inc.; 1988.
- [6] Todd D, Schwager M, Mérida W. Thermodynamics of high-temperature, high-pressure water electrolysis. *J Power Sources* 2014;269:424–9. doi:10.1016/j.jpowsour.2014.06.144.
- [7] Tawfik H, Hung Y, Mahajan D. Metal bipolar plates for PEM fuel cell—A review. *J Power Sources* 2007;163:755–67. doi:10.1016/j.jpowsour.2006.09.088.
- [8] Hermann A, Chaudhuri T, Spagnol P. Bipolar plates for PEM fuel cells: A review. *Int J Hydrogen Energy* 2005;30:1297–302. doi:10.1016/j.ijhydene.2005.04.016.
- [9] Bard AJ, Faulkner LR. *Electrochemical Methods: Fundamentals and Applications*. 2nd ed. John Wiley & Sons; 2001.
- [10] Cooley JF. Apparatus for Electrically Dispersing Fluids. USPTO 692,631, 1902.

- [11] Morton WJ. Method of Dispersing Fluids. USPTO 705,691, 1902.
- [12] Formhals A. Process and Apparatus for Preparing Artificial Threads. USPTO 1,975,504, 1934.
- [13] Greiner A, Wendorff JH. Electrospinning: a fascinating method for the preparation of ultrathin fibers. *Angew Chem Int Ed Engl* 2007;46:5670–703. doi:10.1002/anie.200604646.
- [14] Agarwal S, Wendorff JH, Greiner A. Chemistry on electrospun polymeric nanofibers: merely routine chemistry or a real challenge? *Macromol Rapid Commun* 2010;31:1317–31. doi:10.1002/marc.201000021.
- [15] Andradý AL. Science and technology of polymer nanofibers. Hoboken, NJ: John Wiley & Sons; 2008.
- [16] Bhardwaj N, Kundu SC. Electrospinning: a fascinating fiber fabrication technique. *Biotechnol Adv* 2010;28:325–47. doi:10.1016/j.biotechadv.2010.01.004.
- [17] Dong Z, Kennedy SJ, Wu Y. Electrospinning materials for energy-related applications and devices. *J Power Sources* 2011;196:4886–904. doi:10.1016/j.jpowsour.2011.01.090.
- [18] Feng C, Khulbe KC, Matsuura T. Recent progress in the preparation, characterization, and applications of nanofibers and nanofiber membranes via electrospinning/interfacial polymerization. *J Appl Polym Sci* 2010;115:756–76. doi:10.1002/app.31059.
- [19] Hunley MT, Long TE. Electrospinning functional nanoscale fibers: a perspective for the future. *Polym Int* 2008;57:385–9. doi:10.1002/pi.2320.
- [20] Li D, Xia Y. Electrospinning of Nanofibers: Reinventing the Wheel? *Adv Mater* 2004;16:1151–70. doi:10.1002/adma.200400719.
- [21] Ramaseshan R, Sundarrajan S, Jose R, Ramakrishna S. Nanostructured ceramics by electrospinning. *J Appl Phys* 2007;102:111101. doi:10.1063/1.2815499.
- [22] Tan S, Huang X, Wu B. Some fascinating phenomena in electrospinning processes and applications of electrospun nanofibers. *Polym Int* 2007;56:1330–9. doi:10.1002/pi.2354.
- [23] Thavasi V, Singh G, Ramakrishna S. Electrospun nanofibers in energy and environmental applications. *Energy Environ Sci* 2008;1:205. doi:10.1039/b809074m.

- [24] Ko FK. Nanofiber Technology. In: Gogotsi Y, editor. *Nanotub. Nanofibers*, Boca Raton, FL: CRC Press; 2006.
- [25] Matsumoto H, Tanioka A. Functionality in Electrospun Nanofibrous Membranes Based on Fiber's Size, Surface Area, and Molecular Orientation. *Membranes (Basel)* 2011;1:249–64. doi:10.3390/membranes1030249.
- [26] Ramakrishna S, Fujihara K, Teo W, Yong T, Ma Z, Ramaseshan R. Electrospun nanofibers: solving global issues. *Mater Today* 2006;9:40–50. doi:10.1016/S1369-7021(06)71389-X.
- [27] Sill TJ, von Recum H a. Electrospinning: applications in drug delivery and tissue engineering. *Biomaterials* 2008;29:1989–2006. doi:10.1016/j.biomaterials.2008.01.011.
- [28] Subbiah T, Bhat GS, Tock RW, Parameswaran S, Ramkumar SS. Electrospinning of nanofibers. *J Appl Polym Sci* 2005;96:557–69. doi:10.1002/app.21481.
- [29] Teo WE, Ramakrishna S. A review on electrospinning design and nanofibre assemblies. *Nanotechnology* 2006;17:R89–106. doi:10.1088/0957-4484/17/14/R01.
- [30] Debe MK. Electrocatalyst approaches and challenges for automotive fuel cells. *Nature* 2012;486:43–51. doi:10.1038/nature11115.
- [31] Zhou F-L, Gong R-H, Porat I. Mass production of nanofibre assemblies by electrostatic spinning. *Polym Int* 2009;58:331–42. doi:10.1002/pi.2521.
- [32] Taylor G. Disintegration of Water Drops in an Electric Field. *Proc R Soc A Math Phys Eng Sci* 1964;280:383–97. doi:10.1098/rspa.1964.0151.
- [33] Target Tables from the U.S. DRIVE Fuel Cell Technical Team Technology Roadmap. 2011.
- [34] Mathias M, Roth J, Fleming J, Lehnert W. Chapter 46 Diffusion media materials and characterisation. In: Vielstich W, Lamm A, Gasteiger HA, editors. *Handb. Fuel Cells - Fundam. Technol. Appl.*, vol. 3, Chichester, England: John Wiley and Sons; 2003, p. 517–37.
- [35] Tomadakis MM, Robertson TJ. Viscous Permeability of Random Fiber Structures: Comparison of Electrical and Diffusional Estimates with Experimental and Analytical Results. *J Compos Mater* 2005;39:163–88. doi:10.1177/0021998305046438.

- [36] Tomadakis MM, Sotirchos S V. Effective diffusivities and conductivities of random dispersions of nonoverlapping and partially overlapping unidirectional fibers. *J Chem Phys* 1993;99:9820. doi:10.1063/1.465464.
- [37] Tomadakis MM, Sotirchos S V. Transport properties of random arrays of freely overlapping cylinders with various orientation distributions. *J Chem Phys* 1993;98:616. doi:10.1063/1.464604.
- [38] Tomadakis MM, Sotirchos S V. Transport through random arrays of conductive cylinders dispersed in a conductive matrix. *J Chem Phys* 1996;104:6893. doi:10.1063/1.471356.
- [39] Gostick JT, Fowler MW, Pritzker MD, Ioannidis M a., Behra LM. In-plane and through-plane gas permeability of carbon fiber electrode backing layers. *J Power Sources* 2006;162:228–38. doi:10.1016/j.jpowsour.2006.06.096.
- [40] Li X, editor. *Principles of Fuel Cells*. New York, NY: Taylor & Francis Group; 2006.
- [41] Li H, Tang Y, Wang Z, Shi Z, Wu S, Song D, et al. A review of water flooding issues in the proton exchange membrane fuel cell. *J Power Sources* 2008;178:103–17. doi:10.1016/j.jpowsour.2007.12.068.
- [42] Nam JH, Kaviany M. Effective diffusivity and water-saturation distribution in single- and two-layer PEMFC diffusion medium. *Int J Heat Mass Transf* 2003;46:4595–611. doi:10.1016/S0017-9310(03)00305-3.
- [43] Kitahara T, Konomi T, Nakajima H. Microporous layer coated gas diffusion layers for enhanced performance of polymer electrolyte fuel cells. *J Power Sources* 2010;195:2202–11. doi:10.1016/j.jpowsour.2009.10.089.
- [44] Gostick JT, Ioannidis M a., Fowler MW, Pritzker MD. On the role of the microporous layer in PEMFC operation. *Electrochem Commun* 2009;11:576–9. doi:10.1016/j.elecom.2008.12.053.
- [45] Kim T, Lee S, Park H. A study of water transport as a function of the micro-porous layer arrangement in PEMFCs. *Int J Hydrogen Energy* 2010;35:8631–43. doi:10.1016/j.ijhydene.2010.05.123.
- [46] Wang H, Yuan X-Z, Li H, editors. *PEM Fuel Cell Diagnostic Tools*. Boca Raton, FL: CRC Press; 2012.

- [47] Alink R, Gersteisen D. Scanning Electron Microscopy. In: Wang H, Yuan X-Z, editors. PEM Fuel Cell Diagnostic Tools. 1st ed., Boca Raton, FL: CRC Press; 2012, p. 315–32.
- [48] Harrington DA, van den Driessche P. Mechanism and equivalent circuits in electrochemical impedance spectroscopy. *Electrochim Acta* 2011;56:8005–13. doi:10.1016/j.electacta.2011.01.067.
- [49] Malevich D, Halliop E, Peppley B a., Pharoah JG, Karan K. Investigation of Charge-Transfer and Mass-Transport Resistances in PEMFCs with Microporous Layer Using Electrochemical Impedance Spectroscopy. *J Electrochem Soc* 2009;156:B216. doi:10.1149/1.3033408.
- [50] Anderson R. Characterization of gas-liquid two-phase flow in a proton exchange membrane fuel cell. PhD thesis, University of British Columbia, 2012.
- [51] Dhanushkodi SR, Schwager M, Todd D, Merida W. PEMFC Durability: Spatially Resolved Pt Dissolution in a Single Cell. *J Electrochem Soc* 2014;161:F1315–22. doi:10.1149/2.1031412jes.
- [52] Vie PJS, Kjelstrup S. Thermal conductivities from temperature profiles in the polymer electrolyte fuel cell. *Electrochim Acta* 2004;49:1069–77. doi:10.1016/j.electacta.2003.10.018.
- [53] Burheim OS, Pharoah JG, Lampert H, Vie PJS, Kjelstrup S. Through-Plane Thermal Conductivity of PEMFC Porous Transport Layers. *J Fuel Cell Sci Technol* 2011;8:021013. doi:10.1115/1.4002403.
- [54] Burheim O, Vie PJS, Pharoah JG, Kjelstrup S. Ex situ measurements of through-plane thermal conductivities in a polymer electrolyte fuel cell. *J Power Sources* 2010;195:249–56. doi:10.1016/j.jpowsour.2009.06.077.
- [55] Karimi G, Li X, Teertstra P. Measurement of through-plane effective thermal conductivity and contact resistance in PEM fuel cell diffusion media. *Electrochim Acta* 2010;55:1619–25. doi:10.1016/j.electacta.2009.10.035.
- [56] Khandelwal M, Mench MM. Direct measurement of through-plane thermal conductivity and contact resistance in fuel cell materials. *J Power Sources* 2006;161:1106–15. doi:10.1016/j.jpowsour.2006.06.092.

- [57] Nitta I, Himanen O, Mikkola M. Thermal Conductivity and Contact Resistance of Compressed Gas Diffusion Layer of PEM Fuel Cell. *Fuel Cells* 2008;8:111–9. doi:10.1002/fuce.200700054.
- [58] Sadeghi E, Djilali N, Bahrami M. Effective thermal conductivity and thermal contact resistance of gas diffusion layers in proton exchange membrane fuel cells. Part 1: Effect of compressive load. *J Power Sources* 2011;196:246–54. doi:10.1016/j.jpowsour.2010.06.039.
- [59] Sadeghi E, Djilali N, Bahrami M. Effective thermal conductivity and thermal contact resistance of gas diffusion layers in proton exchange membrane fuel cells. Part 2: Hysteresis effect under cyclic compressive load. *J Power Sources* 2010;195:8104–9. doi:10.1016/j.jpowsour.2010.07.051.
- [60] Ismail MS, Damjanovic T, Ingham DB, Pourkashanian M, Westwood A. Effect of polytetrafluoroethylene-treatment and microporous layer-coating on the electrical conductivity of gas diffusion layers used in proton exchange membrane fuel cells. *J Power Sources* 2010;195:2700–8. doi:10.1016/j.jpowsour.2009.11.069.
- [61] Escribano S, Blachot J-F, Ethève J, Morin A, Mosdale R. Characterization of PEMFCs gas diffusion layers properties. *J Power Sources* 2006;156:8–13. doi:10.1016/j.jpowsour.2005.08.013.
- [62] Chang WR, Hwang JJ, Weng FB, Chan SH. Effect of clamping pressure on the performance of a PEM fuel cell. *J Power Sources* 2007;166:149–54. doi:10.1016/j.jpowsour.2007.01.015.
- [63] Itonen J, Mikkola M, Lindbergh G. Flooding of Gas Diffusion Backing in PEFCs. *J Electrochem Soc* 2004;151:A1152. doi:10.1149/1.1763138.
- [64] Mishra V, Yang F, Pitchumani R. Measurement and Prediction of Electrical Contact Resistance Between Gas Diffusion Layers and Bipolar Plate for Applications to PEM Fuel Cells. *J Fuel Cell Sci Technol* 2004;1:2. doi:10.1115/1.1782917.
- [65] Nitta I, Himanen O, Mikkola M. Contact resistance between gas diffusion layer and catalyst layer of PEM fuel cell. *Electrochem Commun* 2008;10:47–51. doi:10.1016/j.elecom.2007.10.029.
- [66] Smits F. Measurement of sheet resistivities with the four-point probe. *Bell Syst Tech J* 1958.

- [67] Benziger J, Nehlsen J, Blackwell D, Brennan T, Itescu J. Water flow in the gas diffusion layer of PEM fuel cells. *J Memb Sci* 2005;261:98–106. doi:10.1016/j.memsci.2005.03.049.
- [68] Gurau V, Bluemle MJ, De Castro ES, Tsou Y-M, Zawodzinski T a., Mann JA. Characterization of transport properties in gas diffusion layers for proton exchange membrane fuel cells. *J Power Sources* 2007;165:793–802. doi:10.1016/j.jpowsour.2006.12.068.
- [69] Ismail MS, Damjanovic T, Hughes K, Ingham DB, Ma L, Pourkashanian M, et al. Through-Plane Permeability for Untreated and PTFE-Treated Gas Diffusion Layers in Proton Exchange Membrane Fuel Cells. *J Fuel Cell Sci Technol* 2010;7:051016. doi:10.1115/1.4000685.
- [70] Ismail MS, Damjanovic T, Ingham DB, Ma L, Pourkashanian M. Effect of polytetrafluoroethylene-treatment and microporous layer-coating on the in-plane permeability of gas diffusion layers used in proton exchange membrane fuel cells. *J Power Sources* 2010;195:6619–28. doi:10.1016/j.jpowsour.2010.04.036.
- [71] Koido T, Furusawa T, Moriyama K. An approach to modeling two-phase transport in the gas diffusion layer of a proton exchange membrane fuel cell. *J Power Sources* 2008;175:127–36. doi:10.1016/j.jpowsour.2007.09.029.
- [72] Ramos-Alvarado B, Sole JD, Hernandez-Guerrero A, Ellis MW. Experimental characterization of the water transport properties of PEM fuel cells diffusion media. *J Power Sources* 2012;218:221–32. doi:10.1016/j.jpowsour.2012.05.069.
- [73] Taira H, Liu H. In-situ measurements of GDL effective permeability and under-land cross-flow in a PEM fuel cell. *Int J Hydrogen Energy* 2012:1–6. doi:10.1016/j.ijhydene.2012.03.030.
- [74] Mérida W. Porous Transport Layer Degradation. In: Wang H, Li H, Yuan X-Z, editors. *PEM Fuel Cell Fail. Mode Anal.*, Boca Raton, FL: CRC Press; 2011.
- [75] Washburn EW. The dynamics of capillary flow. *Second Ser* 1921;17:273–83.
- [76] Udell KS. Heat transfer in porous media considering phase change and capillarity—the heat pipe effect. *Int J Heat Mass Transf* 1985;28:485–95. doi:10.1016/0017-9310(85)90082-1.

- [77] Pasaogullari U, Wang C-Y, editors. Modern aspects of electrochemistry, no. 49: modeling and diagnostics of polymer electrolyte fuel cells. Springer; n.d.
- [78] Lim C, Wang CY. Effects of hydrophobic polymer content in GDL on power performance of a PEM fuel cell. *Electrochim Acta* 2004;49:4149–56. doi:10.1016/j.electacta.2004.04.009.
- [79] Wood DL, Rulison C, Borup RL. Surface Properties of PEMFC Gas Diffusion Layers. *J Electrochem Soc* 2010;157:B195. doi:10.1149/1.3261850.
- [80] Gurau V, Bluemle MJ, De Castro ES, Tsou Y-M, Mann JA, Zawodzinski T a. Characterization of transport properties in gas diffusion layers for proton exchange membrane fuel cells. *J Power Sources* 2006;160:1156–62. doi:10.1016/j.jpowsour.2006.03.016.
- [81] Fairweather JD, Cheung P, St-Pierre J, Schwartz DT. A microfluidic approach for measuring capillary pressure in PEMFC gas diffusion layers. *Electrochem Commun* 2007;9:2340–5. doi:10.1016/j.elecom.2007.06.042.
- [82] Gallagher KG, Darling RM, Patterson TW, Perry ML. Capillary Pressure Saturation Relations for PEM Fuel Cell Gas Diffusion Layers. *J Electrochem Soc* 2008;155:B1225. doi:10.1149/1.2979145.
- [83] Gostick JT, Ioannidis M a., Fowler MW, Pritzker MD. Direct measurement of the capillary pressure characteristics of water–air–gas diffusion layer systems for PEM fuel cells. *Electrochem Commun* 2008;10:1520–3. doi:10.1016/j.elecom.2008.08.008.
- [84] Harkness IR, Hussain N, Smith L, Sharman JDB. The use of a novel water porosimeter to predict the water handling behaviour of gas diffusion media used in polymer electrolyte fuel cells. *J Power Sources* 2009;193:122–9. doi:10.1016/j.jpowsour.2008.11.055.
- [85] Nguyen T V., Lin G, Ohn H, Wang X. Measurement of Capillary Pressure Property of Gas Diffusion Media Used in Proton Exchange Membrane Fuel Cells. *Electrochem Solid-State Lett* 2008;11:B127. doi:10.1149/1.2929063.
- [86] Gostick JT, Ioannidis M a., Fowler MW, Pritzker MD. Wettability and capillary behavior of fibrous gas diffusion media for polymer electrolyte membrane fuel cells. *J Power Sources* 2009;194:433–44. doi:10.1016/j.jpowsour.2009.04.052.

- [87] Schwager M, Dhanushkodi SR, Merida W. An Approach to Measure the Water Breakthrough in Porous Carbon Materials. *ECS Electrochem Lett* 2015;4:F32–4. doi:10.1149/2.0071504eel.
- [88] Liu T-L, Pan C. Visualization and back pressure analysis of water transport through gas diffusion layers of proton exchange membrane fuel cell. *J Power Sources* 2012;207:60–9. doi:10.1016/j.jpowsour.2012.01.144.
- [89] Jiao K, Park J, Li X. Experimental investigations on liquid water removal from the gas diffusion layer by reactant flow in a PEM fuel cell. *Appl Energy* 2010;87:2770–7. doi:10.1016/j.apenergy.2009.04.041.
- [90] Lu Z, Daino MM, Rath C, Kandlikar SG. Water management studies in PEM fuel cells, part III: Dynamic breakthrough and intermittent drainage characteristics from GDLs with and without MPLs. *Int J Hydrogen Energy* 2010;35:4222–33. doi:10.1016/j.ijhydene.2010.01.012.
- [91] Litster S, Sinton D, Djilali N. Ex situ visualization of liquid water transport in PEM fuel cell gas diffusion layers. *J Power Sources* 2006;154:95–105. doi:10.1016/j.jpowsour.2005.03.199.
- [92] Nam JH, Lee K-J, Hwang G-S, Kim C-J, Kaviany M. Microporous layer for water morphology control in PEMFC. *Int J Heat Mass Transf* 2009;52:2779–91. doi:10.1016/j.ijheatmasstransfer.2009.01.002.
- [93] Alink R, Gerteisen D, Mérida W. Investigating the Water Transport in Porous Media for PEMFCs by Liquid Water Visualization in ESEM. *Fuel Cells* 2011;11:481–8. doi:10.1002/fuce.201000110.
- [94] Markötter H, Alink R, Haußmann J, Dittmann K, Arlt T, Wieder F, et al. Visualization of the water distribution in perforated gas diffusion layers by means of synchrotron X-ray radiography. *Int J Hydrogen Energy* 2012;37:7757–61. doi:10.1016/j.ijhydene.2012.01.141.
- [95] Pai Y-H, Ke J-H, Huang H-F, Lee C-M, Zen J-M, Shieu F-S. CF₄ plasma treatment for preparing gas diffusion layers in membrane electrode assemblies. *J Power Sources* 2006;161:275–81. doi:10.1016/j.jpowsour.2006.03.066.
- [96] Gerteisen D, Heilmann T, Ziegler C. Enhancing liquid water transport by laser perforation of a GDL in a PEM fuel cell. *J Power Sources* 2008;177:348–54. doi:10.1016/j.jpowsour.2007.11.080.

- [97] Kannan AM, Veedu VP, Munukutla L, Ghasemi-Nejhad MN. Nanostructured Gas Diffusion and Catalyst Layers for Proton Exchange Membrane Fuel Cells. *Electrochem Solid-State Lett* 2007;10:B47. doi:10.1149/1.2422751.
- [98] Kannan AM, Munukutla L. Carbon nano-chain and carbon nano-fibers based gas diffusion layers for proton exchange membrane fuel cells. *J Power Sources* 2007;167:330–5. doi:10.1016/j.jpowsour.2007.02.064.
- [99] Lin JF, Wertz J, Ahmad R, Thommes M, Kannan AM. Effect of carbon paper substrate of the gas diffusion layer on the performance of proton exchange membrane fuel cell. *Electrochim Acta* 2010;55:2746–51. doi:10.1016/j.electacta.2009.12.056.
- [100] Chun JH, Park KT, Jo DH, Lee JY, Kim SG, Lee ES, et al. Determination of the pore size distribution of micro porous layer in PEMFC using pore forming agents under various drying conditions. *Int J Hydrogen Energy* 2010;35:11148–53. doi:10.1016/j.ijhydene.2010.07.056.
- [101] Schweiss R, Steeb M, Wilde PM. Mitigation of Water Management in PEM Fuel Cell Cathodes by Hydrophilic Wicking Microporous Layers. *Fuel Cells* 2010;10:1176–80. doi:10.1002/face.201000003.
- [102] Hiramitsu Y, Sato H, Hori M. Prevention of the water flooding by micronizing the pore structure of gas diffusion layer for polymer electrolyte fuel cell. *J Power Sources* 2010;195:5543–9. doi:10.1016/j.jpowsour.2010.03.039.
- [103] Wilkinson DP, Stumper J, Campbell SA, Davis MT, Lamont G. Fuel cell fluid distribution layer having integral sealing capability. USPTO 6,974,647, 2005.
- [104] Mercuri RA. Fluid permeable flexible graphite fuel cell electrode. USPTO 6,413,663, 2002.
- [105] Blanco M. Study of selected water management strategies for proton exchange membrane fuel cells. PhD thesis, University of British Columbia, 2011.
- [106] Cindrella L, Kannan AM. Membrane electrode assembly with doped polyaniline interlayer for proton exchange membrane fuel cells under low relative humidity conditions. *J Power Sources* 2009;193:447–53. doi:10.1016/j.jpowsour.2009.04.002.
- [107] Buie CR, Posner JD, Fabian T, Cha S-W, Kim D, Prinz FB, et al. Water management in proton exchange membrane fuel cells using integrated electroosmotic pumping. *J Power Sources* 2006;161:191–202. doi:10.1016/j.jpowsour.2006.03.021.

- [108] Antolini E, Passos R, Ticianelli E. Effects of the cathode gas diffusion layer characteristics on the performance of polymer electrolyte fuel cells. *J Appl Electrochem* 2002;32:383–8. doi:10.1023/A:1016329820273.
- [109] Chun JH, Park KT, Jo DH, Lee JY, Kim SG, Park SH, et al. Development of a novel hydrophobic/hydrophilic double micro porous layer for use in a cathode gas diffusion layer in PEMFC. *Int J Hydrogen Energy* 2011;36:8422–8. doi:10.1016/j.ijhydene.2011.04.038.
- [110] Tang H, Wang S, Pan M, Yuan R. Porosity-graded micro-porous layers for polymer electrolyte membrane fuel cells. *J Power Sources* 2007;166:41–6. doi:10.1016/j.jpowsour.2007.01.021.
- [111] Kannan AM, Cindrella L, Munukutla L. Functionally graded nano-porous gas diffusion layer for proton exchange membrane fuel cells under low relative humidity conditions. *Electrochim Acta* 2008;53:2416–22. doi:10.1016/j.electacta.2007.10.013.
- [112] Weng F-B, Hsu C-Y, Su M-C. Experimental study of micro-porous layers for PEMFC with gradient hydrophobicity under various humidity conditions. *Int J Hydrogen Energy* 2011;36:13708–14. doi:10.1016/j.ijhydene.2011.07.141.
- [113] Tang Z, Poh CK, Tian Z, Lin J, Ng HY, Chua DHC. In situ grown carbon nanotubes on carbon paper as integrated gas diffusion and catalyst layer for proton exchange membrane fuel cells. *Electrochim Acta* 2011;56:4327–34. doi:10.1016/j.electacta.2011.01.035.
- [114] Du H-Y, Wang C-H, Hsu H-C, Chang S-T, Yen S-C, Chen L-C, et al. High performance of catalysts supported by directly grown PTFE-free micro-porous CNT layer in a proton exchange membrane fuel cell. *J Mater Chem* 2011;21:2512. doi:10.1039/c0jm03215h.
- [115] Chen-Yang YW, Hung TF, Huang J, Yang FL. Novel single-layer gas diffusion layer based on PTFE/carbon black composite for proton exchange membrane fuel cell. *J Power Sources* 2007;173:183–8. doi:10.1016/j.jpowsour.2007.04.080.
- [116] Hung TF, Huang J, Chuang HJ, Bai SH, Lai YJ, Chen-Yang YW. Highly efficient single-layer gas diffusion layers for the proton exchange membrane fuel cell. *J Power Sources* 2008;184:165–71. doi:10.1016/j.jpowsour.2008.05.086.
- [117] Gao Y, Sun GQ, Wang SL, Zhu S. Carbon nanotubes based gas diffusion layers in direct methanol fuel cells. *Energy* 2010;35:1455–9. doi:10.1016/j.energy.2009.11.031.

- [118] Blanco M, Wilkinson DP, Wang H. Perforated Metal Sheets as Gas Diffusion Layers for Proton Exchange Membrane Fuel Cells. *Electrochem Solid-State Lett* 2012;15:B20. doi:10.1149/2.017203esl.
- [119] Fushinobu K, Takahashi D, Okazaki K. Micromachined metallic thin films for the gas diffusion layer of PEFCs. *J Power Sources* 2006;158:1240–5. doi:10.1016/j.jpowsour.2005.10.080.
- [120] Oedegaard a, Hebling C, Schmitz A, Møller-Holst S, Tunold R. Influence of diffusion layer properties on low temperature DMFC. *J Power Sources* 2004;127:187–96. doi:10.1016/j.jpowsour.2003.09.015.
- [121] Shao Z-G, Zhu F, Lin W-F, Christensen P a., Zhang H, Yi B. Preparation and Characterization of New Anodes Based on Ti Mesh for Direct Methanol Fuel Cells. *J Electrochem Soc* 2006;153:A1575. doi:10.1149/1.2209563.
- [122] Chen R, Zhao TS. A novel electrode architecture for passive direct methanol fuel cells. *Electrochem Commun* 2007;9:718–24. doi:10.1016/j.elecom.2006.11.004.
- [123] Voß S, Kollmann H, Kollmann W. New innovative materials for advanced electrochemical applications in battery and fuel cell systems. *J Power Sources* 2004;127:93–7. doi:10.1016/j.jpowsour.2003.09.011.
- [124] Campbell SA, Stumper J, Wilkinson DP, Davis MT. Porous electrode substrate for an electrochemical fuel cell. USPTO 5,863,673, 1999.
- [125] Deyrail Y, Mighri F, Kaliaguine S. Development of Micro- to Macropores in Conductive Polymer-Based Gas Diffusion Layers for Proton Exchange Membrane Fuel Cells. *J Fuel Cell Sci Technol* 2009;6:021309. doi:10.1115/1.3080558.
- [126] Yakisir D, Mighri F, Bousmina M. Development of Porous Electrode Gas Diffusion Layers for Proton Exchange Membrane Fuel Cells. *J Fuel Cell Sci Technol* 2008;5:031008. doi:10.1115/1.2889053.
- [127] Wood DL, Mukundan R, Borup R. In-Plane Mass-Transport Studies of GDL Variation Using the Segmented Cell Approach. *ECS Trans.*, vol. 25, ECS; 2009, p. 1495–506. doi:10.1149/1.3210706.
- [128] Cavaliere S, Subianto S, Savych I, Jones DJ, Rozière J. Electrospinning: designed architectures for energy conversion and storage devices. *Energy Environ Sci* 2011;4:4761. doi:10.1039/c1ee02201f.

- [129] Duan Q, Wang B, Wang J, Wang H, Lu Y. Fabrication of a carbon nanofiber sheet as a micro-porous layer for proton exchange membrane fuel cells. *J Power Sources* 2010;195:8189–93. doi:10.1016/j.jpowsour.2010.07.032.
- [130] Hung C-J, Liu C-H, Ko T-H, Chen W-H, Cheng S-H, Chen W-S, et al. Effect of diffusion layers fabricated with different fiber diameters on the performance of low temperature proton exchange membrane fuel cells. *J Power Sources* 2013;221:134–40. doi:10.1016/j.jpowsour.2012.08.030.
- [131] Gerteisen D, Mérida W, Kurz T, Lupotto P, Schwager M, Hebling C. Spatially Resolved Voltage, Current and Electrochemical Impedance Spectroscopy Measurements. *Fuel Cells* 2011;11:339–49. doi:10.1002/fuce.201000181.
- [132] Morris DRP, Gostick JT. Determination of the in-plane components of the electrical conductivity tensor in PEM fuel cell gas diffusion layers. *Electrochim Acta* 2012;85:665–73. doi:10.1016/j.electacta.2012.08.083.
- [133] Mark RE, Habeger C, Borch J, Lyne MB. *Handbook of Physical Testing of Paper: Volume 1*. 2nd ed. New York, NY: CRC Press; 2001.
- [134] Morris DRP, Liu SP, Gonzalez DV, Gostick JT. Effect of Water Sorption on the Electronic Conductivity of Porous Polymer Electrolyte Membrane Fuel Cell Catalyst Layers. *ACS Appl Mater Interfaces* 2014;6:18609–18. doi:10.1021/am503509j.
- [135] Zhou T, Liu H. Effects of the electrical resistances of the GDL in a PEM fuel cell. *J Power Sources* 2006;161:444–53. doi:10.1016/j.jpowsour.2006.04.106.
- [136] Sun W, Peppley B a., Karan K. Modeling the Influence of GDL and flow-field plate parameters on the reaction distribution in the PEMFC cathode catalyst layer. *J Power Sources* 2005;144:42–53. doi:10.1016/j.jpowsour.2004.11.035.
- [137] He G, Yamazaki Y, Abudula A. A three-dimensional analysis of the effect of anisotropic gas diffusion layer(GDL) thermal conductivity on the heat transfer and two-phase behavior in a proton exchange membrane fuel cell(PEMFC). *J Power Sources* 2010;195:1551–60. doi:10.1016/j.jpowsour.2009.09.059.
- [138] Han K, Hong BK, Kim SH, Ahn BK, Lim TW. Influence of anisotropic bending stiffness of gas diffusion layers on the electrochemical performances of polymer electrolyte membrane fuel cells. *Int J Hydrogen Energy* 2010;35:12317–28. doi:10.1016/j.ijhydene.2010.08.061.

- [139] Naing KSS, Tabe Y, Chikahisa T. Performance and liquid water distribution in PEFCs with different anisotropic fiber directions of the GDL. *J Power Sources* 2011;196:2584–94. doi:10.1016/j.jpowsour.2010.10.080.
- [140] Kleemann J, Finsterwalder F, Tillmetz W. Characterisation of mechanical behaviour and coupled electrical properties of polymer electrolyte membrane fuel cell gas diffusion layers. *J Power Sources* 2009;190:92–102. doi:10.1016/j.jpowsour.2008.09.026.
- [141] Cohen SS. Contact resistance and methods for its determination. *Thin Solid Films* 1983;104:361–79. doi:10.1016/0040-6090(83)90577-1.
- [142] Sullivan M V., Eigler JH. Five Metal Hydrides as Alloying Agents on Silicon. *J Electrochem Soc* 1956;103:218. doi:10.1149/1.2430281.
- [143] Williams M V., Begg E, Bonville L, Kunz HR, Fenton JM. Characterization of Gas Diffusion Layers for PEMFC. *J Electrochem Soc* 2004;151:A1173. doi:10.1149/1.1764779.
- [144] Wasscher JD. Note of four-point resistivity measurements on anisotropic conductors. *Philips Res Reports* 1961;16:301–6.
- [145] Van der Pauw LJ. Determination of resistivity tensor and Hall tensor of anisotropic conductors. *Philips Res Reports* 1961;16:187.
- [146] Montgomery HC. Method for Measuring Electrical Resistivity of Anisotropic Materials. *J Appl Phys* 1971;42:2971. doi:10.1063/1.1660656.
- [147] Nitta I, Hottinen T, Himanen O, Mikkola M. Inhomogeneous compression of PEMFC gas diffusion layer. *J Power Sources* 2007;171:26–36. doi:10.1016/j.jpowsour.2006.11.018.
- [148] Caillard a., Brault P, Mathias J, Charles C, Boswell RW, Sauvage T. Deposition and diffusion of platinum nanoparticles in porous carbon assisted by plasma sputtering. *Surf Coatings Technol* 2005;200:391–4. doi:10.1016/j.surfcoat.2005.01.033.
- [149] Dos Santos C a. M, de Campos A, da Luz MS, White BD, Neumeier JJ, de Lima BS, et al. Procedure for measuring electrical resistivity of anisotropic materials: A revision of the Montgomery method. *J Appl Phys* 2011;110:083703. doi:10.1063/1.3652905.

- [150] Burheim OS, Pharoah JG, Lampert H, Vie PJS, Kjelstrup S. Through-Plane Thermal Conductivity of PEMFC Porous Transport Layers. *J Fuel Cell Sci Technol* 2011;8:021013. doi:10.1115/1.4002403.
- [151] Fishman Z, Hinebaugh J, Bazylak A. Microscale Tomography Investigations of Heterogeneous Porosity Distributions of PEMFC GDLs. *J Electrochem Soc* 2010;157:B1643. doi:10.1149/1.3481443.
- [152] Oloman C, Matte M, Lum C. Electronic Conductivity of Graphite Fiber Fixed-Bed Electrodes. *J Electrochem Soc* 1991;138:2330–4.
- [153] Sadeghi E, Djilali N, Bahrami M. Effective thermal conductivity and thermal contact resistance of gas diffusion layers in proton exchange membrane fuel cells. Part 2: Hysteresis effect under cyclic compressive load. *J Power Sources* 2010;195:8104–9. doi:10.1016/j.jpowsour.2010.07.051.
- [154] Kim S, Ahn BK, Mench MM. Physical degradation of membrane electrode assemblies undergoing freeze/thaw cycling: Diffusion media effects. *J Power Sources* 2008;179:140–6. doi:10.1016/j.jpowsour.2007.12.114.
- [155] Park J-H, Ju Y-W, Park S-H, Jung H-R, Yang K-S, Lee W-J. Effects of electrospun polyacrylonitrile-based carbon nanofibers as catalyst support in PEMFC. *J Appl Electrochem* 2009;39:1229–36. doi:10.1007/s10800-009-9787-4.
- [156] Singer SL. Low platinum loading electrospun electrodes for proton exchange membrane fuel cells. Massachusetts Institute of Technology, 2004.
- [157] Sighting JJ, McPherson E, Rigdon WA, Huang X. Application of Electrospinning Technique in the Fabrication of Catalyst Layer of Membrane Electrode Assemblies. *ECS Trans* 2013;50:1445–51. doi:10.1149/05002.1445ecst.
- [158] Zhang W, Brodt MW, Pintauro PN. Nanofiber Cathodes for Low and High Humidity Hydrogen Fuel Cell Operation. *ECS Trans.*, vol. 41, 2011, p. 891–9. doi:10.1149/1.3635623.
- [159] Kurpiewski JP. Electrospun Carbon Nanofiber Electrodes Decorated with Palladium Metal Nanoparticles: Fabrication and Characterization. Massachusetts Institute of Technology, 2005.
- [160] Ballengee JB, Pintauro PN. Morphological Control of Electrospun Nafion Nanofiber Mats. *J Electrochem Soc* 2011;158:B568. doi:10.1149/1.3561645.

- [161] Lee KM, Choi J, Wycisk R, Pintauro PN, Mather P. Nafion Nanofiber Membranes. *ECS Trans.*, vol. 25, ECS; 2009, p. 1451–8. doi:10.1149/1.3210701.
- [162] Tamura T, Kawakami H. Aligned electrospun nanofiber composite membranes for fuel cell electrolytes. *Nano Lett* 2010;10:1324–8. doi:10.1021/nl1007079.
- [163] Ra EJ, An KH, Kim KK, Jeong SY, Lee YH. Anisotropic electrical conductivity of MWCNT/PAN nanofiber paper. *Chem Phys Lett* 2005;413:188–93. doi:10.1016/j.cplett.2005.07.061.
- [164] Kim J, Lee S-M, Srinivasan S, Chamberlin CE. Modeling of Proton Exchange Membrane Fuel Cell Performance with an Empirical Equation. *J Electrochem Soc* 1995;142:2670. doi:10.1149/1.2050072.
- [165] Herrera OE, Wilkinson DP, Mérida W. Anode and cathode overpotentials and temperature profiles in a PEMFC. *J Power Sources* 2012;198:132–42. doi:10.1016/j.jpowsour.2011.09.042.
- [166] Kok MDR, Gostick JT. Transport properties of electrospun fibrous membranes with controlled anisotropy. *J Memb Sci* 2015;473:237–44. doi:10.1016/j.memsci.2014.09.017.
- [167] Götz M, Wendt H. Binary and ternary anode catalyst formulations including the elements W, Sn and Mo for PEMFCs operated on methanol or reformat gas. *Electrochim Acta* 1998;43:3637–44. doi:10.1016/S0013-4686(98)00121-2.
- [168] Wang B. Recent development of non-platinum catalysts for oxygen reduction reaction. *J Power Sources* 2005;152:1–15. doi:10.1016/j.jpowsour.2005.05.098.
- [169] Barazzouk S, Lefèvre M, Dodelet J-P. Oxygen Reduction in PEM Fuel Cells: Fe-Based Electrocatalysts Made with High Surface Area Activated Carbon Supports. *J Electrochem Soc* 2009;156:B1466. doi:10.1149/1.3242293.
- [170] Antolini E. Composite materials: An emerging class of fuel cell catalyst supports. *Appl Catal B Environ* 2010;100:413–26. doi:10.1016/j.apcatb.2010.08.025.
- [171] Antolini E, Gonzalez ER. Polymer supports for low-temperature fuel cell catalysts. *Appl Catal A Gen* 2009;365:1–19. doi:10.1016/j.apcata.2009.05.045.
- [172] Antolini E. Carbon supports for low-temperature fuel cell catalysts. *Appl Catal B Environ* 2009;88:1–24. doi:10.1016/j.apcatb.2008.09.030.

- [173] Debe MK, Schmoeckel AK, Vernstrom GD, Atanasoski R. High voltage stability of nanostructured thin film catalysts for PEM fuel cells. *J Power Sources* 2006;161:1002–11. doi:10.1016/j.jpowsour.2006.05.033.
- [174] De Bruijn F a., Dam V a. T, Janssen GJM. Review: Durability and Degradation Issues of PEM Fuel Cell Components. *Fuel Cells* 2008;8:3–22. doi:10.1002/fuce.200700053.
- [175] Kim JM, Joh H-I, Jo SM, Ahn DJ, Ha HY, Hong S-A, et al. Preparation and characterization of Pt nanowire by electrospinning method for methanol oxidation. *Electrochim Acta* 2010;55:4827–35. doi:10.1016/j.electacta.2010.03.036.
- [176] Kim HJ, Kim YS, Seo MH, Choi SM, Cho J, Huber GW, et al. Highly improved oxygen reduction performance over Pt/C-dispersed nanowire network catalysts. *Electrochem Commun* 2010;12:32–5. doi:10.1016/j.elecom.2009.10.029.
- [177] Kim YS, Kim HJ, Kim WB. Compositing hybrid electrocatalysts of Pt-based nanoparticles and nanowires for low temperature polymer electrolyte fuel cells. *Electrochem Commun* 2009;11:1026–9. doi:10.1016/j.elecom.2009.03.003.
- [178] Kim YS, Nam SH, Shim H-S, Ahn H-J, Anand M, Kim WB. Electrospun bimetallic nanowires of PtRh and PtRu with compositional variation for methanol electrooxidation. *Electrochem Commun* 2008;10:1016–9. doi:10.1016/j.elecom.2008.05.003.
- [179] Kim HJ, Kim YS, Seo MH, Choi SM, Kim WB. Pt and PtRh nanowire electrocatalysts for cyclohexane-fueled polymer electrolyte membrane fuel cell. *Electrochem Commun* 2009;11:446–9. doi:10.1016/j.elecom.2008.12.027.
- [180] Zhou X, Qiu Y, Yu J, Yin J, Gao S. Tungsten carbide nanofibers prepared by electrospinning with high electrocatalytic activity for oxygen reduction. *Int J Hydrogen Energy* 2011;36:7398–404. doi:10.1016/j.ijhydene.2011.03.081.
- [181] Shui J, Li JCM. Platinum nanowires produced by electrospinning. *Nano Lett* 2009;9:1307–14. doi:10.1021/nl802910h.
- [182] Formo E, Peng Z, Lee E, Lu X, Yang H, Xia Y. Direct Oxidation of Methanol on Pt Nanostructures Supported on Electrospun Nanofibers of Anatase. *J Phys Chem C* 2008;112:9970–5. doi:10.1021/jp803763q.

- [183] Guo B, Zhao S, Han G, Zhang L. Continuous thin gold films electroless deposited on fibrous mats of polyacrylonitrile and their electrocatalytic activity towards the oxidation of methanol. *Electrochim Acta* 2008;53:5174–9. doi:10.1016/j.electacta.2008.02.060.
- [184] Han GY, Guo B, Zhang LW, Yang BS. Conductive Gold Films Assembled on Electrospun Poly(methyl methacrylate) Fibrous Mats. *Adv Mater* 2006;18:1709–12. doi:10.1002/adma.200600098.
- [185] Hong S-H, Lee S-A, Nam J-D, Lee Y-K, Kim T-S, Won S. Platinum-catalyzed and ion-selective polystyrene fibrous membrane by electrospinning and in-situ metallization techniques. *Macromol Res* 2008;16:204–11. doi:10.1007/BF03218854.
- [186] Huang J, Hou H, You T. Highly efficient electrocatalytic oxidation of formic acid by electrospun carbon nanofiber-supported Pt_xAu_{100-x} bimetallic electrocatalyst. *Electrochem Commun* 2009;11:1281–4. doi:10.1016/j.elecom.2009.04.022.
- [187] Li M, Han G, Yang B. Fabrication of the catalytic electrodes for methanol oxidation on electrospinning-derived carbon fibrous mats. *Electrochem Commun* 2008;10:880–3. doi:10.1016/j.elecom.2008.04.002.
- [188] Li M, Zhao S, Han G, Yang B. Electrospinning-derived carbon fibrous mats improving the performance of commercial Pt/C for methanol oxidation. *J Power Sources* 2009;191:351–6. doi:10.1016/j.jpowsour.2009.01.089.
- [189] Lin Z, Ji L, Zhang X. Electrodeposition of platinum nanoparticles onto carbon nanofibers for electrocatalytic oxidation of methanol. *Mater Lett* 2009;63:2115–8. doi:10.1016/j.matlet.2009.07.005.
- [190] Lin Z, Ji L, Zhang X. Electrocatalytic properties of Pt/carbon composite nanofibers. *Electrochim Acta* 2009;54:7042–7. doi:10.1016/j.electacta.2009.07.022.
- [191] Lin Z, Ji L, Woodroof MD, Yao Y, Krause W, Zhang X. Synthesis and Electrocatalysis of Carbon Nanofiber-Supported Platinum by 1-AP Functionalization and Polyol Processing Technique. *J Phys Chem C* 2010;114:3791–7. doi:10.1021/jp9096138.
- [192] Liu X, Li M, Han G, Dong J. The catalysts supported on metallized electrospun polyacrylonitrile fibrous mats for methanol oxidation. *Electrochim Acta* 2010;55:2983–90. doi:10.1016/j.electacta.2010.01.014.

- [193] Schechner P, Kroll E, Bubis E, Chervinsky S, Zussman E. Silver-Plated Electrospun Fibrous Anode for Glucose Alkaline Fuel Cells. *J Electrochem Soc* 2007;154:B942. doi:10.1149/1.2752975.
- [194] Su L, Jia W, Schempf A, Ding Y, Lei Y. Free-Standing Palladium/Polyamide 6 Nanofibers for Electrooxidation of Alcohols in Alkaline Medium. *J Phys Chem C* 2009;113:16174–80. doi:10.1021/jp905606s.
- [195] Xuyen NT, Jeong HK, Kim G, So KP, An KH, Lee YH. Hydrolysis-induced immobilization of Pt(acac)₂ on polyimide-based carbon nanofiber mat and formation of Pt nanoparticles. *J Mater Chem* 2009;19:1283. doi:10.1039/b813486c.
- [196] Graeser M, Pippel E, Greiner A, Wendorff JH. Polymer Core–Shell Fibers with Metal Nanoparticles as Nanoreactor for Catalysis. *Macromolecules* 2007;40:6032–9. doi:10.1021/ma070898d.
- [197] Lin Z, Woodroof MD, Ji L, Liang Y, Krause W, Zhang X. Effect of platinum salt concentration on the electrospinning of polyacrylonitrile/platinum acetylacetonate solution. *J Appl Polym Sci* 2009;n/a – n/a. doi:10.1002/app.31616.
- [198] Lefèvre M, Proietti E, Jaouen F, Dodelet J-P. Iron-based catalysts with improved oxygen reduction activity in polymer electrolyte fuel cells. *Science* 2009;324:71–4. doi:10.1126/science.1170051.
- [199] Qiu Y, Yu J, Wu W, Yin J, Bai X. Fe–N/C nanofiber electrocatalysts with improved activity and stability for oxygen reduction in alkaline and acid solutions. *J Solid State Electrochem* 2012;14–7. doi:10.1007/s10008-012-1888-z.
- [200] Tekmen C, Tsunekawa Y, Nakanishi H. Electrospinning of carbon nanofiber supported Fe/Co/Ni ternary alloy nanoparticles. *J Mater Process Technol* 2010;210:451–5. doi:10.1016/j.jmatprotec.2009.10.006.
- [201] Zhang W, Pintauro PN. High-performance nanofiber fuel cell electrodes. *ChemSusChem* 2011;4:1753–7. doi:10.1002/cssc.201100245.

Appendix A

The author's conference and publication history follows.

A.1 Publications

1. **D. Todd**, M. Schwager, W. Mérida. (2015) “Three-dimensional anisotropic electrical resistivity of PEM fuel cell transport layers as functions of compressive strain”. *Journal of The Electrochemical Society*, 162, F265-F272. DOI: 10.1149/2.0611503jes
2. **D. Todd**, W. Mérida. (2015) “Morphologically controlled fuel cell transport layers enabled via electrospun carbon nonwovens”. *Journal of Power Sources*, 273, 312-316. DOI: 10.1016/j.jpowsour.2014.09.095
3. S. R. Dhanushkodi, M. Schwager, **D. Todd**, W. Mérida. (2014) “PEMFC durability: spatially resolved Pt dissolution in a single cell”. *Journal of The Electrochemical Society*, 161, F1315-F1322. DOI: 10.1149/2.1031412jes
4. **D. Todd**, M. Schwager, W. Mérida. (2014) “Thermodynamics of high-temperature, high-pressure water electrolysis”. *Journal of Power Sources*, 269, 42-429. DOI: 10.1016/j.jpowsour.2014.06.144

A.2 Publications in preparation

1. **D. Todd**, S. Bennett, W. Mérida. (2015) “Anisotropic electrical resistance of proton exchange membrane fuel cell transport layers as a function of cyclic mechanical compression”. *under review*.
2. **D. Todd**, W. Mérida. (2015) “Proton exchange membrane fuel cell transport layers with progressive fibre alignment for the study of anisotropy effects upon performance”. *under review*.

A.3 Conferences

1. **D. Todd***, W. Mérida. (2015) “Synthesis and performance of anisotropic porous transport layers”. Technical seminar presented at the International Conference on Electrochemical Energy Science and Technology, Vancouver, BC, August 19.
2. **D. Todd***, M. Schwager, L. Damron, S. R. Dhanushkodi, W. Mérida. (2015) “Sustainable transportation: current developments for the PEM fuel cell at UBC”. Poster presented at the 7th International Conference on Engineering Education for Sustainable Development, Vancouver, BC, June 12.
3. **D. Todd***, M. Schwager, S. R. Dhanushkodi, W. Mérida. (2015) “Porous transport layer characterization and efforts in engineered structures”. Poster presented at the Catalysis Research for Polymer Electrolyte Fuel Cells Network, Burnaby, BC, May 7.
4. **D. Todd***, S. R. Dhanushkodi, W. Mérida. (2015) “Progress in PEM fuel cell diagnostics and characterization”. Technical seminar presented at the Catalysis Research for Polymer Electrolyte Fuel Cells Network, Burnaby, BC, May 7.
5. **D. Todd***, M. Schwager, S. R. Dhanushkodi, W. Mérida. (2015) “Recent development for the PEM fuel cell at UBC”. Poster presented at the 1st UBC Sustainability Research Symposium, Vancouver, BC, March 4.
6. L. Damron*, M. Schwager, S. Flick, **D. Todd**, S. R. Dhanushkodi, W. Mérida. (2014) “The recent development of diagnostic tools for the PEM Fuel cell catalyst layer at UBC”. Poster presented at the International Symposium on Electrocatalysis, Whistler, BC, October 27.
7. **D. Todd***, S. Flick, W. Mérida. (2014) “UBC activities within the CARPE-GECKO collaboration”. Technical seminar presented at the Catalysis Research for Polymer Electrolyte Fuel Cells Network, Burnaby, BC, June 6.
8. M. Schwager*, **D. Todd**, S. R. Dhanushkodi, W. Mérida. (2014) “Spatially Resolved PEMFC Diagnostics via Segmented Cell Featuring Independent Power Electronics Applied to Water and Catalyst Management”. Technical seminar presented at the 97th Canadian Chemistry Conference and Exhibition, Vancouver, B. C., June 4.
9. S. R. Dhanushkodi*, M. Schwager, **D. Todd**, W. Mérida. (2014) “Use of Segmented Cells in Durability Testing: Experimental Studies to Measure the Spatial Distribution of Pt Surface Area and Performance Loss in PEM Fuel Cells”. Technical seminar presented at the 97th Canadian Chemistry Conference and Exhibition, Vancouver, B. C., June 4.
10. S. Bennett*, **D. Todd**, W. Mérida. (2014) “Analysis of the effect of plastic deformation on the through plane conductivity of porous transport layers in proton exchange membrane fuel cells”. Technical seminar presented at the UBC Multidisciplinary Undergraduate Research Conference, Vancouver, BC, March 22.

11. O.E. Herrera, **D. Todd***, S. Flick and W. Mérida. (2011) “Heat management in anode and cathode of a PEMFC”. Technical seminar presented at the Hydrogen + Fuel Cells 2011: International Conference and Exhibition, Vancouver, B.C., May 17.

Appendix B

B.1 Introduction

A comprehensive literature review compiled the applications of electrospinning technology towards PEM fuel cell CL development; interest stems from electrospinning's characteristics of high specific surface areas and versatility in materials. The review was not restricted to the H₂-O₂ type.

A CL must provide: catalytic sites, ionic connectivity to the electrolyte, electronic connectivity outwards, and physical access for reactive species (three-phase contact sites). Much of PEM fuel cell development has been defined by catalyst layer evolution. Early CLs were manufactured from platinum black and binder mixtures hot-pressed to membranes; these systems are reliable, but prohibitively expensive. Carbon supported platinum (Pt/C) offers superior mass-specific area, enabling lower catalyst loadings (reduced cost). State-of-the-art low catalyst loading (e.g. ~ 0.15 mg Pt·cm⁻²) CLs are based on Pt/C inks. These are applied to either the membrane or the PTLs as dispersions of: catalyst, ionomer, (PTFE), and solvent. Deposition methods include: brushing, spraying, blade deposition, rod coating, casting, and decal-transfer. Contemporary avenues of experimental development include:

- Pt alloys, such as Pt-Ru which improves poisoning resistance [167].
- Non-Pt catalysts, such as ammonium macrocycles [168] or iron-based catalysts [169].
- Alternative supports, such as non-conventional carbons, metallics, ceramics, polymers and hybrids thereof [170–172].
- Nanostructured layers, such as 3M nanostructured thin film CLs [173].

The motivation for such work is reduction (or elimination) of Pt and improving durability. Use of the precious metal is a major contributor to cost; whilst CL degradation (e.g. by Pt particle dissolution, migration and agglomeration; and carbon support corrosion [174]) currently prevents satisfaction of lifetime performance targets without exceeding cost targets [30].

B.2 Literature

The application of electrospinning to the manufacture of catalyst materials has received active interest from the research community [17,23]. For the synthesis of catalytic fibres, general progression is: spinning a carrier polymer and catalyst precursor solution, thermal treatment, dispersion into an ink, and application to the MEA. Korean researchers, of the Gwangju Institute of Science and Technology and Korea Institute of Technology, have published a method to electrospin catalyst nanowires for alcohol fuel cells. Pt-Ru-Rh alloys have been explored, as have combinations of catalyst wires decorated with Pt/C [175–179]. By similar means, Zhou et al. have prepared tungsten carbide fibres for ORR application [180]. Though not performing the post-treatments to obtain metallic catalyst particles, Shui et al. describe the impact of synthesis parameters upon electrospun Polyvinylpyrrolidone and Pt precursor fibre morphology [181].

More prevalent is electrospun material as supports for catalysts. A variety of (common) catalyst deposition methods are available: polyol method, NaBH_4 reduction, electrodeposition, electroless plating, and sputter deposition. Formo et al. produced Pt nanoparticles and nanofibres upon electrospun anatase (TiO_2) fibres for methanol fuel cells. Anatase was generated by calcination of electrospun precursor, while platinum was deposited by the polyol processes [182]. Guo et al. produced gold coated PAN fibres for methanol oxidation by electrospinning a PAN and Au salt solution, NaBH_4 reduction, and electroless plating [183]. Earlier, Han et al. of the same group, produced Au coated poly(methyl methacrylate) by similar means [184]. Hong et al. produced sulfonated polystyrene membranes catalysed with Pt [185]. Polystyrene mats were electrospun, sulfonated, and catalysed by sequential and repetitive immersion in Pt and reduction agent solutions. Huang et al. applied electrospun carbon supported Pt-Au catalyst for formic acid oxidation [186]. Dispersed electrospun carbon fibres were deposited onto an electrode and electroplated; they observed the alloy assisted in suppressing CO poisoning.

Li et al. produced catalysed mats of electrospun carbon for methanol oxidation. In one publication, they evaluated the performance of multi-cycle Pt electrodeposition [187]. In a second, electrospun layers were assessed for the support of Pt/C catalyst [188]; the smaller average pore size versus commercial substrates was suggested to improve activity and stability. Lin et al. demonstrated incorporation of Pt into electrospun PAN derived carbon fibres by two means for methanol applications. One was electrodeposition at fixed potential [189,190]; fixed potential yielded smaller particles with effective penetration into the substrate versus deposition with pulsed potential. The second made use of 1-aminopyrene pre-treated fibres to

enhance the polyol process [191]; pre-treatment produced smaller, more evenly distributed, Pt particles whilst maintaining carbon support integrity. Liu et al. applied Pt to Au metallized electrospun mats for methanol fuel cell electrodes [192]. PAN was electrospun and electroless plated with Au, Pt was subsequently cycle-electrodeposited; performance was compared against, the electrodeposited Pt possessed greater activity but inferior stability versus a Pt/C decorated metallized substrate. Park et al. produced electrospun carbon fibres decorated with Pt via a polyol process for hydrogen fuel cells [155]. The argument was fibre, versus carbon black, nano-pore morphology is more amenable to attaching three-phase accessible catalyst. Schechner et al. described Ag plated electrospun electrodes for glucose alkaline fuel cells [193]. Polycaprolactone was electrospun and subsequently electroless plated with silver. Singer published a thesis upon sputter coated electrospun layers for hydrogen PEM fuel cells [156]. PAN mats were electrospun, carbonized, sputtered with Pt, ionomer impregnated, and hot-pressed into MEAs; these CLs were distinct from the PTLs. Compared to commercial CLs, the electrospun layers performed poorly. Su et al. produced Pd-polyamide6 fibre electrodes for ethanol alkaline fuel cells [194]. Polyamide6 was electrospun to produce a free-standing template for the electroless deposition of palladium. Xuyen et al. bonded Pt onto carbon fibres by means of a hydrolysis reaction [195]. Electrospun poly(amic acid) was stabilized into polyamide, surface hydrolyzed, immersed in Pt solution, and thermally treated to generate carbon and metallic Pt.

Catalyst material may also be directly incorporated in the electrospinning dope; to be used as-is or with chemistry dependent post-treatments. Not intended for fuel cells, but rather catalysing hydrogenation reactions, Graeser et al. produced core-shell fibres featuring nanoparticles of Pd, Rh and Pt [196]. Polyethylene oxide and metal salts solution was electrospun, vapour coated with poly-p-xylylene, reduced under hydrogen, and stripped of the polyethylene oxide core; this work offers a precedent for how Pt might be incorporated into electrospun PEM fuel cell structures. Lin et al. described the rheology, electrospinning behaviour, and resultant fibre morphology for PAN and platinum(II)acetylacetonate solutions in DMF [197]; they did not post-process to synthesize metallic platinum. Increasing salt concentrations increased fibre diameters without altering the distribution. In contrast, decreasing salt concentrations decreased fibres diameters, with a critical threshold where the distribution broadened. Qui et al. applied the Fe-based catalyst developed by Dodelet's group [169,198] to an electrospun carbon fibre substrate [199]. PAN fibres were electrospun, impregnated with iron, and carbonized under ammonia. Tekmen et al. produced electrospun carbon fibres with ternary Fe-Co-Ni catalyst for alcohol PEM fuel cells [200]. Solutions of PAN and acetylacetonate salts were electrospun then thermally treated to carbonize the polymer and nucleate the catalyst; electrochemical tests were not performed. Zhang and Pintauro describe CLs of electrospun

poly(acrylic acid), Nafion and Pt/C [201]. All components were included in the dope, and as-spun mats were hot-pressed into MEAs.